Performance Comparison of Forced Draft and Induced Draft Air-Cooled Condensers under Adverse Crosswind Conditions

by

Daniel Louis Louw

Dissertation presented for the degree of Doctor of Philosophy (Mechanical Engineering) in the Faculty of Engineering at Stellenbosch University

Supervisor: Prof. C.J. Meyer
Co-supervisor: Prof. S.J. van der Spuy

December 2021

Declaration

By submitting this dissertation electronically, I declare that the entirety of the work contained therein is my own, original work, that I am the sole author thereof (save to the extent explicitly otherwise stated), that reproduction and publication thereof by Stellenbosch University will not infringe any third party rights and that I have not previously in its entirety or in part submitted it for obtaining any qualification.

Date: ....December 2021......

Abstract

Performance Comparison of Forced Draft and Induced Draft Air-Cooled Condensers under Adverse Crosswind Conditions

D.L. Louw

Department of Mechanical and Mechatronic Engineering,
University of Stellenbosch,
Private Bag X1, Matieland 7602, South Africa.

Dissertation: PhD (Mech. Eng.)

December 2021

In this study numerical models of two 8×8 fan-unit Air-Cooled Condensers (ACCs) were developed using Computational Fluid Dynamics (CFD). The two ACCs investigated were respectively a Forced Draft ACC with A-frame fan-units and an Induced Draft ACC with V-frame fan-units. The performance of the two ACCs was investigated under various adverse crosswind conditions. The numerical models were implemented using the open-source `OpenFOAM` CFD code and solved in parallel using a computer cluster.

The ACCs' axial flow fans were modeled using an Actuator Disk Model (ADM). The ACCs investigated in this study were configured using two different axial flow fans: an eight bladed fan identified as the L-fan, and a nine bladed fan identfied as the N-fan. Comparatively the L-fan has a steeper pressure characteristic and a higher power consumption than the N-fan and was used exclusively at the front and back periphery of the ACCs. The ADM was specifically implemented for the two fans and succesfully validated against experimental results obtained from a BS 848 Type A Facility.

A direct comparison of the two ACCs shows that under normal operating conditions the Induced Draft ACC outperforms the Forced Draft ACC both with regards to its volumetric effectiveness and heat transfer effectiveness. The two ACC were then subjected to crosswinds of 3, 6 and 9 m/s from two different directions: primary crosswinds where the L-fan is used at the leading edge, and secondary crosswinds where the N-fan is used at the leading edge.

The Forced Draft ACC showed a greater reduction in axial flow fan performance under crosswind conditions than the Induced Draft ACC. Under primary crosswinds the L-fan equipped leading edge fan-units were able to mitigate the reduced fan performance better than the N-fan equiped leading edge fan-units under secondary crosswinds.

The Induced Draft ACC showed higher heat exchanger inlet air temperatures under crosswind conditions than the Forced Draft ACC. The Induced Draft ACC's perpendicular orientation of its V-frame fan-units to secondary crosswinds allowed for greater increases in the inlet air temperatures at its downwind fan-units' heat exchangers.

The Induced Draft ACC's heat transfer rate to fan power consumption ratio under primary crosswind conditions was higher than that of the Forced Draft ACC under either primary or secondary crosswinds. In contrast the Induced Draft ACC's heat-to-power ratio under secondary crosswind conditions was worse than that of the Forced Draft ACC under either primary or secondary crosswinds.

The mean heat-to-power ratio of the Induced Draft ACC under normal operating conditions was higher than that of the Forced Draft ACC with a ratio of 120.6 W/W compared to 99.4 W/W. However, the mean heat-to-power ratio of the Induced Draft ACC decreased more by 23.3% and 35.6% under 9 m/s primary and secondary crosswinds, while the heat-to-power ratios of the Forced Draft ACC decreased less by 10.8% and 15.4% under the same crosswinds.

Uittreksel

Vergelyking van die Werksverrigting van Geforseerde Vloei en Geïnduseerde Vloei Lugverkoelde Kondensors onder Kruiswind Toestande

("Performance Comparison of Forced Draft and Induced Draft Air-Cooled Condensers under Adverse Crosswind Conditions")

D.L. Louw

Departement Meganiese en Megatroniese Ingenieurswese,
Universiteit van Stellenbosch,
Privaatsak X1, Matieland 7602, Suid Afrika.

Proefskrif: PhD (Meg. Ing.)

Desember 2021

In hierdie studie is numeriese modelle van twee 8×8 waaiereenheid lugverkoelde kondensors (LVKs) met behulp van numeriese vloei meganika ontwikkel. Die twee LVKs was onderskeidelik 'n Geforseerde Vloei LVK met A-raam waaiereenhede en 'n Geïnduseerde Vloei LVK met V-raam waaiereenhede. Die werksverrigting van die twee LVKs onder verskeie wind toestande is in hierdie studie ondersoek en vergelyk. Die numeriese modelle was ontwikkel met behulp van die `OpenFOAM` vloeimeganika kode en geïmplementeer vir parallel oplossing op 'n trosrekenaar.

Die LVKs se aksiaalvloei waaiers is met 'n aksieskyfmodel gemodelleer. Die twee LVKs is met twee verskillende aksiaalvloei waaiers opgestel: 'n agt-lem waaier en 'n nege lem waaier wat onderskeidelik die L-waaier en die N-waaier genoem is. Die L-waaier het vergelykbaar 'n steiler druk karakteristiek en hoër kragverbruik as die N-waaier en is uitsluitlik by die voorkant en agterkant van die LVKs gebruik. Die aksieskyfmodel was spesifiek vir die studie geïmplenteer en is suksesvol gevalideer teenoor eksperimentele resultate van 'n BS 848 Tipe A Fasiliteit.

'n Direkte vergelyking van die twee LVKs wys dat sonder enige wind die Geïnduseerde Vloei LVK meer doeltreffend is as die Geforseerde Vloei LVK met betrekking tot beide die volumetriese effektiwiteit en die hitte oordrag effektiwiteit. Die twee LVK se werksverrigting is daarna onder kruiswinde van 3, 6 en 9 m/s vanaf twee verskillende windsrigtings getoets: waar die

primêre windsrigting die L-waaier by die voorkant van die LVK plaas, en waar sekondêre winde die N-waaier by die voorkant van die LVK plaas.

Die Geforseerde Vloei LVK wys 'n laer vermindering in die waaier effektiwiteit onder kruiswinde as die Geïnduseerde Vloei LVK. Onder primêre kruiswinde wys die L-waaier waaiereenhede aan die voorkant van die LVK 'n laer vermindering in waaier effectiwiteit as die N-waaier waaiereenhede aan die sykant van die LVK onder sekondêre kruiswinde.

Die Geïnduseerde Vloei LVK wys a groter verhoging in die hitte-uitruilers se lug inlaat temperatuur onder kruiswinde as die Geforseerde Vloei LVK. Die Geïnduseerde Vloei LVK se loodregte opstelling van sy V-raam hitte-uitruilers teenoor die sekondêre kruiswind het groter verhogings in die lug inlaat temperature van stroomaf waaiereenhede se hitte-uitruilers veroorsaak.

Die Geïnduseerde Vloei LVK se hitte oordragstempo teenoor die waaiers se kragverbruik onder primêre kruiswinde was hoër as die van die Geforseerde Vloei LVK onder beide primêre en sekondêre kruiswinde. In kontras was die Geïnduseerde Vloei LVK se hitte-to-kragverbruiks verhouding onder sekondêre kruiswinde laer as die van die Geforseerde Vloei LVK onder beide primêre en sekondêre kruiswinde.

Die gemiddelde hitteoordrag-tot-kragverbruik verhouding van die Geïnduseerde Vloei LVK onder normale toestande was hoër as dit van die Geforseerde Vloei LVK met 'n verhouding van 120.6 W/W teenoor 99.4 W/W. Die gemiddelde hitteoordrag-tot-kragverbruik verhouding van die Geïnduseerde Vloei LVK het met 23.3% en 35.6% verminder onder 9 m/s primêre en sekondêre kruiswinde, terwyl die Geforseerde Vloei LVK slegs met 10.8% en 15.4% verminder het onder dieselfde kruiswind toestande.

Acknowledgements

I would like to express my sincere gratitude to the following people and organisations:

- My supervisors, Prof. S.J. van der Spuy and Prof. C.J. Meyer, without whom this thesis would not have been possible.
- My parents, P.L. Louw and Dr. A.L. Scheepers, whose support throughout this endeavour has never faltered.
- My predecessor, R.A. Engelbrecht, who gave me a running start.
- T.M. Schommarz and C. du Plessis, fellow students and dear friends.
- ESKOM and the Eskom Power Plant Engineering Institute (EPPEI) for funding this project.
- The Centre for High Performance Computing (CHPC), South Africa, for providing computational resources to this project.

Contents

List of Figures

List of Tables

Nomenclature

Constants

g	Gravitional Accelaration, 9.81 m/s^2
$\overline{R}$	Ideal Gas Constant, 8.314 J/K mol

Variables

x	Coordinate	[m]
t	Time	[s]
$\mathbf{u}$	Velocity Vector	[m/s]
ρ	Density	[kg/m^3]
p	Pressure	[N/m^2]
μ	Viscosity	[N · s/m^2]
T	Temperature	[K]
i	Internal Energy	[J/kg]
κ	Thermal Conductivity	[W/m]
k	Turbulence Kinetic Energy	[m^2/s^2]
ϵ	Dissipation Rate of Turbulence Energy	[m^2/s^3]
$\bar{\mu}$	Bulk Viscosity	[N · s/m^2]
U	Velocity Magnitude	[m/s]
V	Volume	[m^3]
$\dot{m}$	Mass Flow Rate	[kg/s]
ε	Effectiveness	[ ]
$\dot{Q}$	Heat Transfer Rate	[W]
$\dot{W}$	Fan Power Consumption	[W]
η	Efficiency	[%]
F	Force	[N]
f	Force per Unit Volume	[N/m^3]
C	Coefficient	[ ]
γ	Blade Angle	[°]
β	Average Relative Blade Angle	[°]

α	Angle of Attack	[°]
σ	Fan Solidity	[m/m]
n_b	Number of Fan Blades	[ ]
c	Chord Length	[m]
r	Radial Coordinate	[m]
ζ	Blade Stagger Angle	[m]
h	Heat Transfer Coefficient	[W/m$^2 \cdot$ K]
A	Area	[m^2]
β	Thermal Expansion Coefficient	[1/K]
K	Loss Coefficient	[°]
r	Radius	[m]
D	Diameter	[m]
L	Length	[m]
W	Width	[m]
Nu	Nusselt Number	[ ]
Re	Reynolds Number	[ ]

Subscripts

0	reference
f	fan
R	relative
L	lift
D	drag
i	inlet *OR* i-th index
o	outlet
a	air *OR* axial-component
t	tangential-component
r	radial-component
p	pressure
v	vapor
x	cross-section
c	condensate
NTU	Number of Transfer Units
HTP	Heat-to-Power
he	heat exchanger
iso	isothermal
$niso$	non-isothermal

$\perp$	perpendicular component
$\parallel$	parallel component

Chapter 1

Introduction

1.1 Background and Motivation

Thermal power generation cycles require heat to be discharged (Kröger, 1998). The heat rejection is required to complete the thermodynamic cycle, keeping the power generation cycle in compliance with the second law of thermodynamics (Çengel and Boles, 2008).

The Rankine cycle generates power from steam using a steam turbine. It is used to harness power from thermal energy sources – i.e coal, nuclear, natural gas and solar-thermal energy. An example of the Rankine cycle is shown in Fig. 1.1.

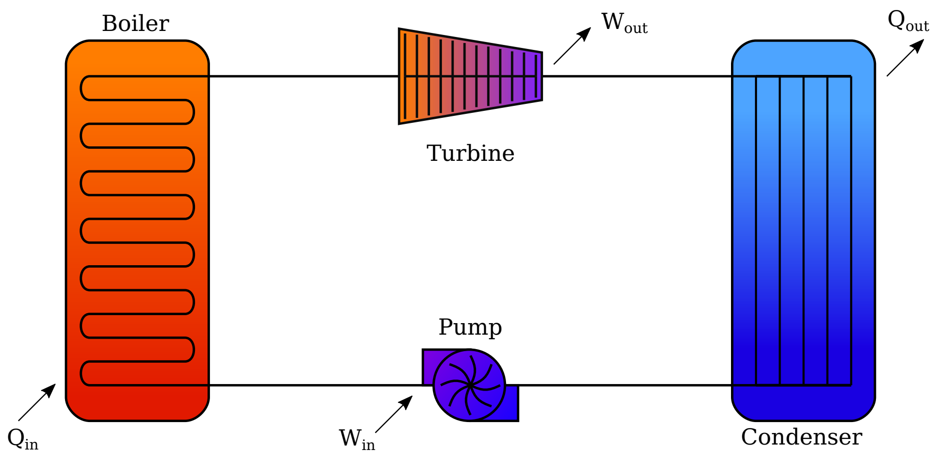

Figure 1.1: Ideal Rankine Cycle

The cooling systems used in the power generation cycles are categorised by the mechanisms used to facilitate the heat transfer and the airflow through the system (Kröger, 1998). Wet cooled systems utilise surface condensers and the evaporation of cooling water in a cooling tower to facilitate heat transfer. Dry cooled systems utilise convective heat transfer to the atmosphere via an air-cooled condenser (ACC). Hybrid wet/dry and dry/wet systems utilise a combination of the two methods.

The heat transfer performance of dry cooled systems is limited by the higher drybulb temperature of air, as opposed to that of wet cooled systems that is limited by the from lower ambient wetbulb temperatures (Kröger, 1998). The result is that dry cooled systems are neither as effective nor as seasonally consistent as wet cooled systems. However, wet cooled systems, as the name suggests, require a consistent water supply to replenish losses due to evaporation. Water scarcity may override both economic and performance considerations when choosing between the two technologies.

Natural draft systems exploit the buoyancy of heated air, isolated from ambient conditions via a cooling tower, to facilitate airflow through the system. Mechanical draft systems utilise axial flow fans to directly force airflow through the system. Mechanical draft systems may or may not make use of cooling towers to exploit the buoyancy effect of heated air.

Mechanical draft ACCs are further subcategorised according to the arrangement of the heat exchangers and the axial flow fans. Forced draft ACCs locate the axial flow fans upstream of the heat exchanger bundles, while induced draft ACCs reverse the fan and heat exchanger arrangment. Examples of forced and induced draft systems are shown in Fig. 1.2.

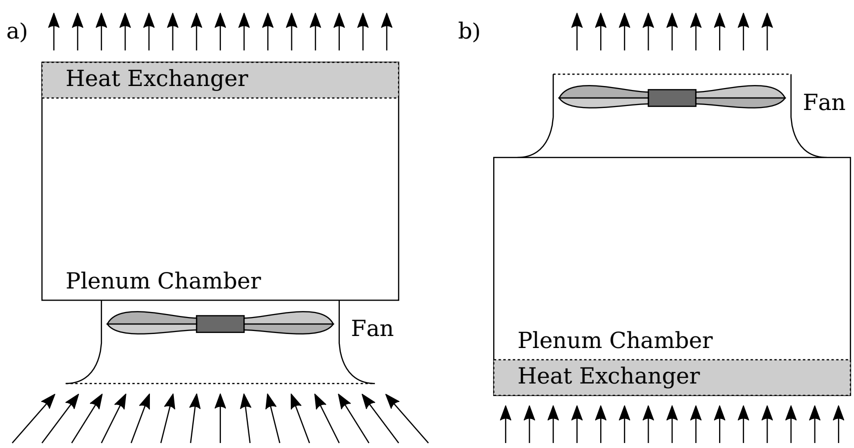

Figure 1.2: Fan-Units: a) Forced Draft, b) Induced Draft

For the purpose of this study, a large ACC is defined as having at least 60 fan-units. The distinction between small and large ACCs is twofold, based on physical and numerical considerations. Certain unique flow field phenomena such as hot plume recirculation are only present in multiple fan ACCs. Additionally, non-trivial computational resources are required to solve numerical models of large ACCs.

ESKOM, South Africa's electricity utility, currently operates the world's largest dry-cooled coal-fired power stations. Matimba, currently the largest, houses 6×665 MW turbines where the steam is condensed using a 288 fan-unit forced draft ACC. Two new power stations, Medupi and Kusile, housing 6×794 MW turbines are currently under construction, both of which utilise forced draft ACCs similar to the one at Matimba.

As previously mentioned, dry cooled systems are neither as effective nor as consistent as wet cooled systems. Reduced ACC performance, and thus decreased heat rejection in the thermodynamic cycle, can severely limit the steam turbine's ability to generate power, due to increased turbine backpressure (Goldschagg, 1993).

A need exists to ensure that ACCs are implemented effectively, which in turn requires investigation of the factors that limit ACC performance. Full scale experiments are impractical due to the physical size of the air-cooled condenser and the axial flow fans in question (van der Spuy, 2011). Computational Fluid Dynamics (CFD) offers an alternative method to model the performance of the air-cooled condenser under various conditions.

Previous studies investigating ACC performance using CFD have faced multiple limitations. Explicit 3-dimensional fan modeling is computationally expensive, forcing the use of simplified models. Even with the use of simplified models such as the pressure jump model, full scale models of large ACCs remain computationally expensive. A need exists to reduce the cost associated with solving the numerical ACC models.

Thiart and von Backström (1993) developed the actuator disk model (ADM) to investigate distorted inflow conditions for axial flow fans. The ADM is a highly capable simplified fan model based on blade element theory, with significant advantages over simplified fan models such as the pressure jump model (PJM). Among the advantages of the ADM is its ability to accurately predict the fan power consumption and the flow field downstream of the fan rotor.

Previous studies have investigated the effects of crosswinds on ACC performance (van Rooyen, 2007; Joubert, 2010; Owen, 2010; Louw, 2011; Engelbrecht, 2018). These studies identified crosswinds as a primary cause of distorted inflow conditions for fans located at the upstream periphery of the ACC. Secondary flow field phenomena such as hot plume recirculation were also identified.

The numerical ACC models developed thus far have been limited to small ACC units and/or use of the pressure jump model. Notably the largest ACC modeled to date is the 384-fan ACC model created by Louw (2011) which utilized the PJM and an interpolation scheme to model all 384 fans. The largest ACCs modeled using only the ADM are two 30-fan ACC models created by Engelbrecht (2018).

Engelbrecht (2018) investigated the two distinct 30-fan ACCs using multiple fan configurations aimed at mitigating reduced fan performance due to distorted inlet flow conditions. The fans investigated included a commercially available axial flow fan and a research fan developed by Bruneau (1994). Increases in ACC performance where noted in configurations where higher-powered axial flow fans where located at the periphery of the ACC.

Engelbrecht (2018) implemented the ADM using OpenFOAM, Open Source Field Operations And Manipulation, which is an C++ toolbox for the development of solvers and utilities for finite volume CFD. The use of OpenFOAM provided scalability to the ADM that was unmatched by previous implementations.

1.2 Research Objectives

The objective of this study is to develop, solve and evaluate numerical models of two large 64-fan ACCs using a rotating fan model, one of which is a Forced Draft A-frame design and the other an Induced Draft V-frame design. This study will investigate and compare the performance of the two ACCs when subjected to adverse crosswind conditions. This study builds upon the work of Thiart and von Backström (1993), Louw (2011) and Engelbrecht (2018).

The specific objectives of this study are:

1. Implementing and solving the numerical models of a 64-fan Forced Draft ACC and a 64-fan Induced Draft ACC:
    a) Modeling the axial flow fans using the actuator disk model to provide an accurate alternative to explicit 3-dimensional fan modeling, and matching the fans' experimental performance characteristics.
    b) Modeling the heat exchangers and matching the heat exchangers' experimental characteristics.
    c) Modeling a single fan-unit ACC unit and matching the results to an analytical draft equation.

d) Developing the models for parallel computing on a High Performance Cluster (HPC) using OpenFOAM to solve the size and scalability constraints faced in previous studies.

2. Investigate and compare the performance of the two ACCs regarding:

    a) Different fan configurations, specifically the placement of high volumetric flow rate fans at the periphery of the ACCs.

    b) Different wind speeds and directions, as well as the macro scale phenomena associated with such crosswinds, i.e. hot plume recirculation.

Chapter 2

Literature Review

2.1 Air-Cooled Condensers

Monroe (1979) described methods to improve the efficiency of an axial flow fan used in both wet and dry cooled systems. Monroe (1979) highlighted differences between the 'ideal' efficiencies of axial flow fans and the 'real life' efficiencies of fan systems measured in full scale set-ups. Three categories of potential losses in system efficiency were identified: losses attibuted to the fan itself, losses attributed to the system, and losses attributed to emerging macro scale phenomena. Poor fan blade design and operating point selection result in losses attributed to the fan that are effectively 'built-in' to the system, making detection and correction difficult. Losses attibuted to the system include fan tip clearance losses, poor fan inlet conditions and random leaks in the plenum chamber. Lastly, an example of emerging macro scale phenomena given by Monroe (1979) is hot plume recirculation, whereby hot air exiting the heat exchangers is drawn back into the system.

Kröger (1998) describes an analytical draft equation for mechanical draft air-cooled condensers. The draft equation describes a single fan-unit ACC as a system of consecutive flow resistances which are matched against the axial flow fan's performance characteristics. A compact version of the draft equation is given below:

$$\Delta p_{fan} = \sum_{i}^{n} K_i \frac{m_{ai}/A_i}{2\rho_{ai}} \tag{2.1}$$

where K is the loss coefficient, m_a the air mass flow rate, A the cross-sectional area and ρ_a the air density. Various loss coefficients for features commonly found in ACC set-ups are provided by Kröger (1998). More details on the analytical draft equation can be found in Appendix B.

2.2 Axial Fan Models

Explicit fan modeling involves creating a full 3-dimensional (3D) model of the fan. Each individual blade of the axial flow fan is rotated around a common reference frame (i.e. the fan's axis of rotation). The flow is then explicitly modeled over each fan blade. Implementation of a full 3D fan model is computationally expensive. At least 3.5×10^6 cells per fan blade are required for an accurate representation of a single eight bladed fan rotor (van der Spuy *et al.*, 2009).

Simplified fan models have been developed to model fans at a fraction of the computational cost. There are two well documented simplified fan models that have been used to model the performance of axial flow fans for ACCs, namely the pressure jump model (PJM), which utilizes the fan's characteristic curve, and the actuator disk model (ADM), which utilizes blade element theory.

The pressure jump model (PJM) introduces an axial source term into the momentum equation of the axial flow fan that corresponds to the expected static-to-static pressure rise over the fan. The magnitude of the source term is determined by using the fan's characteristic curve which maps the fan's volumetric flow rate to its total-to-static pressure rise. The pressure jump model has been effectively implemented in the modeling of power station cooling systems by Owen (2010), Joubert (2010), Louw (2011), Yang *et al.* (2011) and Chen *et al.* (2018).

The actuator disk model (ADM) was initially developed by Thiart and von Backström (1993). The ADM utilizes blade element theory to determine the forces exerted on the flow field by the axial flow fan, which are then added as body forces in the Navier-Stokes equations. The body forces exerted on the flow field are defined as the corresponding reaction forces to the lift and drag forces exerted on the fan blades by the flow field. The lift and drag forces themselves are calculated using the lift and drag coefficients of the fan blade profile and the corresponding angle of attack between the relative velocity vector and the fan blade chord. The ADM is able to directly calculate the fan's power consumption during operation, a feature unavailable to the PJM. The ADM has been successfully implemented for small power station cooling systems by Bredell (2005), van Rooyen (2007) and Engelbrecht (2018).

A study by van der Spuy *et al.* (2009) compared the predicted flow for both the pressure jump model and actuator disk model against experimental data also collected during the study. Both models were capable of accurately predicting the fan performance while attempting to replicate the fan's characteristic curves within its normal operating range. The study noted that the required number of cells to accurately model the flow is considerably less than that required for an explicit full 3D model. The ADM was capable of delivering a more accurate representation of the downstream flow field due to it considering the local blade flow field properties. The PJM is noted as being purely a reflection of the fan performance curve, and should therefore perform well for uniformly distributed flow entering the fan (as is present in the BS 848 setup used to test the fan).

The actuator disk model under-predicts the fan total-to-static pressure rise at low volumetric flow rates. The under-predicted fan performance is due to the 2-dimensional derivation of the ADM not accounting for the 3-dimensional radial flow that is present at low volumetric flow rates. This shortcoming has led to the development of the extended actuator disk model (EADM) by van der Spuy (2011) and the reverse engineered empirical actuator disk model (REEADM) by Louw (2015). Both extended models exhibit improved accuracy in their predictions, but both models still under-predict the static pressure rise at low volumetric flow rates.

2.3 Heat Exchanger Models

Explicit heat exchanger modeling involves creating a full 3-dimensional model of the heat exchanger. Explicit models may or may not require modeling of both the hot and cold side of the heat exchanger. Similar to explicit fan modeling, explicit heat exchanger modeling can become computationally expensive and therefore simplified models are used to reduce the computational cost. The simplified models must accurately model both the heat transfer and the pressure drop characteristics of the heat exchanger.

The ϵ-NTU (Effectiveness Number of Transfer Units) method can be used to calculate the air-side heat transfer of heat exchangers when limited information regarding the steam temperatures is available (Kröger, 1998). The ϵ-NTU method was successfully utilized to model heat transfer at the heat exchanger by Joubert (2010), Owen (2010), Louw (2011) and Engelbrecht (2018).

Porous media have been used to model the pressure drop characteristic of heat exchangers in ACCs. The Darcy-Forchheimer porosity model was used to model the heat exchanger pressure by Joubert (2010), Owen (2010), Louw (2011) and Engelbrecht (2018).

2.4 Air-Cooled Condenser Models

Previous studies have attempted to numerically model air-cooled condensers. Computational constraints have limited both the size of the ACCs modeled and the numerical fan and heat exchanger models used.

Du Toit and Kröger (1993) investigated the recirculation of flow in mechanical draft ACC systems. A simplified 2-dimensional numerical model was employed and compared to both analytical and experimental results. The study found large recirculating regions in the flow field located at the sides of the ACC. Additionally, little to no mixing was found between hot plume and ambient air as evident in the calculated temperature distribution. Both the numerical flow field results and temperature distribution showed agreement with the analytical and experimental results.

Thiart and von Backström (1993) investigated the effects of non-uniform inlet flow conditions on the performance of ACC fan-units. The newly developed actuator disk model was used to provide numerical results which were validated against experimental results. Neighbouring fans, buildings and crosswinds were identified as potential causes of distorted flow conditions at the fan inlets. The study concluded that more power is required to achieve similar volumetric flow rates under crosswind conditions than those attained under idealised inlet conditions.

Salta and Kröger (1995) experimentally investigated the effect of platform height on the fan performance of an ACC. An empirical correlation was derived showing an exponential decrease in fan performance as the fan platform height is reduced. Decreased fan performance was observed at the periphery fans when compared to the inner fans, with the performance decrease especially pronounced at low fan platform heights. The study also identified increases in periphery fan performance associated with increases in the ACC's walkway width.

Duvenage *et al.* (1996) numerically investigated the effect of platform height and shroud design on the fan performance of an ACC. The results showed that the empirical correlation derived by Salta and Kröger (1995) could be extended for multiple fan inlet shrouds. Furthermore, the fan inlet shroud is emphasized as an important feature of an ACC that should be evaluated carefully during the design process.

Bredell (2005) modeled a single row of forced draft ACC fan-units using the ADM. The largest of the numerical models developed used a total of 810×10^3 cells to investigate the effect of crosswinds on the ACC. Parallel slip planes and a symmetry plane were utilized to reduce the entire ACC to a single row of ACC fan-units, thereby reducing the computational resource required for the study. The plenum chamber of the ACC was also simplified as a box plenum. The study evaluated the inlet flow conditions of the ACC. The results showed flow separation and distorted flow inlet conditions at the fan inlet caused by cross-flow beneath the fan platform. These flow conditions have an adverse effect on the volumetric effectiveness of the fans at the periphery of the ACC.

Van Rooyen (2007) modeled a 30-fan forced draft ACC by making use of the ADM. Due to the limited computational resources available, only certain fan units were simulated and the results interpolated to determine the overall performance of the ACC. The numerical investigation used computational meshes sized between 800×10^3 and 1.5×10^6 cells. The results of the study showed strong correlation to those obtained by Bredell (2005). The study attributed the greatest loss in performance to reduced fan performance due to distorted flow conditions and separation at the fan inlet. Additionally, the study found hot plume recirculation to have an adverse, yet marginal, affect on the ACCs overall performance. The presence of obstructions in the flow path, such as walkways around the periphery of the ACC and porous windscreens below the ACC, was found in certain configurations to have a positive effect on the fan performance of the ACC.

Owen (2010) modeled a 30-fan forced draft ACC by making use of a two stage modeling process and the PJM. The numerical model used for the investigation consisted of 2.669×10^6 cells. The study looked at the effect of wind on the performance of an existing power station in Nevada, USA. The plenum chamber of the ACC was also simplified by using a box plenum chamber instead of the actual A-frame. The effects of obstructions such as walkways and windscreens in the flow path were investigated. The presence of walkways was found beneficial to the performance of the ACC, confirming the results obtained by van Rooyen (2007). The use of correctly configured windscreens was also found to be beneficial to the fan performance of the ACC. It was found that increasing the fan power by scaling the fan characteristic curves used in the PJM could increase ACC performance. However the performance gains were limited by diminishing returns after a 20 % increase in fan power.

Joubert (2010) modeled the same 30-fan forced draft ACC that was investigated by van Rooyen (2007). The numerical model of the ACC used in the investigation consisted of approximately 6.7×10^6 cells. The use of a PJM allowed the full model to be simulated due to the reduction in intensive computational requirements imposed by the model. Furthermore, it allowed for a comparative analysis between the two simplified fan models, with good correlation between the studies shown. The effect of obstructions, walkways and windscreens was again investigated, along with an investigation into alternative flow inlets and fan configurations. The results correlate well with previous studies and show that the presence of walkways around the periphery of the ACC, as well as porous windscreens located below it, can improve the performance of an ACC.

Louw (2011) was able to model a large 384-fan forced draft ACC using an implementation of the PJM and an interpolation scheme. The numerical model used in the study used a total of 8.25×10^6 cells to investigate the effect of wind on the ACC's performance. The size of the ACC modeled allowed for a comparison of both longitudinal and orthogonal crosswinds (relative to the longest edge of the ACC). The results of the wind direction analysis showed that the wind direction can both increase and reduce the ACC's performance, with increased performance for longitudinal winds and reduced performance for orthogonal crosswinds. The size of the ACC investigated by Louw allowed for a more in-depth analysis regarding the effect of crosswinds on hot plume recirculation. The vortices formed along the parallel edges of the ACC are exaggerated at higher crosswinds, resulting in increased recirculation at these edges.

Louw's (2011) results showed good correlation with those from previous studies, linking flow separation at the upstream edge of the ACC to reduced performance. Furthermore the effect of the power station building itself on ACC performance was also included in the investigation of flow obstructions, walkways and porous windscreens. The use of walkways around the periphery of the ACC was found to increase performance by 2 to 9 %, dependent on the width of the walkway. The placement of a windscreen below the ACC was found to increase the overall performance of the ACC by 8 to 30 %, dependent on both the location and size of the windscreen.

Yang *et al.* (2011) investigated the performance of a generic 7×16 ACC subject to crosswind conditions. The numerical investigation used a 2.126×10^6 grid mesh for the simulations with no crosswinds, and a 2.090×10^6 grid mesh for the simulations with crosswinds. The axial flow fans were modeled using a PJM augmented with and additional empirically derived source term that introduces a tangential component to account for the rotational flow through the fan. The overall performance of the ACC was found to decrease as the crosswind magnitude increased, with the greatest decreases found at the upwind fan-units.

Engelbrecht (2018) modeled two different 30-fan forced draft ACCs under adverse crosswind conditions using the ADM for all fans. The two 30-fan ACCs investigated were a 6×5 ACC and a 3×10 ACC, which were configured using two different axial flow fans. The 6×5 ACC was numerically modeled using a 8.671×10^6 cell mesh. Under crosswind conditions, the overall ACC performance for each configuration investigated was shown to decrease as the crosswind velocity increased. The decreases in overall performance were primarily attributed to decreased fan performance at the upstream fan-units, with the downstream and centre-located fan-units largely unaffected by the crosswinds.

Engelbrecht (2018) found that similar performance trends for individual fans were shown for both the 6×5 and the 3×10 ACC layouts. However, the volumetric, thermal and overall performance showed increased sensitivity to crosswind for the 3×10 ACC due to its asymmetrical layout. The total fan power consumption was also found to be significantly higher for the 3×10 ACC for each fan configuration investigated. Hot plume recirculation under crosswind conditions was identified at the fan-units located at the downstream peripheries parallel to the crosswinds direction. Engelbrecht also identified reverse flow through the upstream fan-units as a second phenomena responsible for decreased thermal performance of the ACC. Reverse flow through upstream fan-units was found to be more prominent for crosswinds orthogonal to the long axis of the 3×10 ACC due to the greater number of fans at the upstream periphery.

The two axial flow fans investigated by Engelbrecht (2018) included a commercially available axial flow fan and the high efficiency, high volumetric flow rate B2a-fan designed by Bruneau (1994). Engelbrecht was able to identify significant improvements in the heat-to-power ratio of individual fan-units where the ACC's fan configuration utilized the B2a-fan. The highest volumetric and thermal performance was found for ACCs utilizing a combined commercial-fan and B2a-fan configuration, with the B2a-fan located at the periphery of the ACC. The highest overall performance, determined using the heat-to-power ratio, was found for ACCs utilizing only the B2a-fan.

Chen *et al.* (2018) investigated two 7×16 ACCs, one configured with forced draft A-frame fan-units and one with induced draft V-frame fan-units. The maximum grid sizes for their numerical investigation was 3.411×10^6 and 3.730×10^6 for the A-frame and V-frame investigations respectively. Similar to Yang *et al.* (2011) a PJM using an additional tangential source term was used to model the axial flow fans. The study found that the A-frame ACC performed poorly at the upwind fan-units under crosswind conditions, while the V-frame ACC performed better due to the axial flow fan's location behind the heat exchangers reducing off-axis flow into the fan. For the V-frame ACC under crosswind conditions the overall performance of the fan-units immediately downwind of the leading edge was shown to be worse than that of the leading edge fan-units. No significant asymmetry was shown to exist for either of the two ACC's volumetric or heat exchanger performance.

Huang *et al.* (2019) numerically modeled a 5×12 forced draft A-frame ACC equipped with two types of deflectors located below the periphery of the ACC and investigated the performance of the ACC under various crosswind conditions. The largest computational mesh used in the investigations had a grid size of 4.854×10^6 nodes, and the axial flow fans were modeled using a PJM. The deflectors at the periphery was found to increase the leading edge axial flow fans' performance, however the deflectors also increased the effect of hot plume recirculation at the periphery. The overall benefit of the deflectors below the periphery was found to be dependent on the crosswind direction. The arc-style deflectors outperformed the plane-style deflectors for all cases. An experimental validation of heat exchanger's inlet air temperatures was conducted in the study with good correlation between the numerical and experimental results achieved.

2.5 Literature

This study aims to answer the following open questions in the current literature:

1. The differences in performance between Forced Draft A-frame and Induced Draft V-frame ACCs under crosswind conditions, where the axial flow fans used in the ACC are represented using an actuator disk model (ADM), allowing the investigation of:
    a) The local flow field phenomena,
    b) The fan power consumption, and thus also
    c) The ACC's heat-to-power ratio.
2. The effect of crosswinds on the performance of large ACCs, i.e. >30 fan-units, where the axial flwo fans are modeled using an ADM where the following phenomena can be analysed in greater detail:
    a) Flow separation at the leading edge of the ACC,
    b) Hot plume recirculation at the periphery of the ACC, and
    c) The influence fo using different fan configurations at the periphery of the ACC on the ACC performance.

Chapter 3

Numerical Modeling Strategy

3.1 Computational Fluid Dynamics

3.1.1 Governing Equations

A fluid's motion in 3-dimensions is governed by three principles (Versteeg and Malalasekera, 2015; Schobeiri, 2010). These are the conservation of mass, the conservation of momentum and the conservation of energy, which are respectively given by the following three relations:

$$\frac{\partial \rho}{\partial t} + \nabla \cdot (\rho \mathbf{u}) = 0 \tag{3.1}$$

$$\frac{\partial (\rho \mathbf{u})}{\partial t} + \nabla \cdot (\rho \mathbf{u}\mathbf{u}) = -\nabla p + \nabla \cdot (\mu \nabla \mathbf{u}) + \mathbf{S}_M \tag{3.2}$$

$$\frac{\partial (\rho i)}{\partial t} + \nabla \cdot (\rho i \mathbf{u}) = -p \ \nabla \cdot \mathbf{u} \ + \nabla \cdot (\kappa \nabla T) + \Phi + S_i \tag{3.3}$$

where the dissipation function Φ is defined as

$$\Phi = 2\mu \ \nabla \mathbf{u} : \nabla \mathbf{u} + (\bar{\mu} - 2/3 \ \mu) \ (\nabla \cdot \mathbf{u})^2 \tag{3.4}$$

where $\bar{\mu}$ is the bulk viscosity which for most engineering application can be approximated as $\bar{\mu} = 0$ (Schobeiri, 2010).

The governing equations are often simplified for incompressible flows by assuming a uniform and constant density field.

`OpenFOAM` uses the finite volume method to discretize and numerically solve the aforementioned partial differential equations.

3.1.2 Buoyancy Effect

The bouyancy effect is present in flow fields with non-uniform density and a gravitional field. The buoyancy effect can be approximated or explicitly modeled.

Boussinesq Approximation

Solving the fully compressible derivations of the governing equations for flows with a variable density field is computationally expensive.

The Boussinesq approximation introduces a non-uniform effective density field, ρ_k, that is used to calculate a buoyancy source term. The buouyancy source term is added to the incompressible form of the governing equations.

The Boussinesq approximation's buoyancy source term is defined as:

$$\mathbf{S}_M = \frac{\rho_{ref} - \rho_k}{\rho_k}\mathbf{g} \tag{3.5}$$

where ρ_{ref} is the reference density of the incompressible flow.

The Boussinesq approximation's equation of state for the effective density is given by the following relation:

$$\rho_k = \rho_{ref}(1 - \beta(T - T_{ref})) \tag{3.6}$$

where β is the thermal expansion coefficient, T is the actual temperature and T_{ref} is the reference temperature.

The Boussinesq approximation is valid when:

$$\frac{\beta(T - T_{ref})}{\rho_{ref}} << 1 \tag{3.7}$$

Ideal Gas

Solving the fully compressible form of the governing equations with a gravitional source term is sufficient when the buoyancy effect needs to be modeled without approximations.

The gravitational source term added to the governing equations is defined as:

$$\mathbf{S}_M = \rho\mathbf{g} \tag{3.8}$$

The density field can be calculated using the equation of state for an ideal gas which is given by the following relation:

$$\rho = \frac{1}{RT}p \tag{3.9}$$

where R is the specific gas constant, T is the temperature and p is the pressure.

The ideal gas relation can be simplified by assuming a constant reference pressure p_{ref}. This simplification holds for fluid flows where the density is primarily dependent on the temperature.

3.1.3 Turbulence Models

Fluid flow is subject to both inertial and viscous forces. The Reynolds number, Re, of a fluid flow is the dimensionless ratio of the inertial forces and the viscous forces that are present in the flow field:

$$Re = \frac{\rho U L}{\mu} \tag{3.10}$$

where L is a characteristic length.

Turbulent flow occurs when the inertial forces in the flow field are dominant, i.e. the flow has a high characteristic Reynolds numbers, and are subject to fluctuations in both the velocity and pressure fields. For most engineering applications the flow regimes are turbulent and thus require representation in the flow analysis (Versteeg and Malalasekera, 2015). However, resolving the turbulent fluctuations using direct numerical simulation (DNS) is computationally expensive and therefore turbulence models have been developed to solve the Reynolds-averaged Navier-Stokes (RANS) equations which describe the mean flow of the fluid.

The *standard* k-ϵ turbulence model (Launder and Spalding, 1974) adds two additional transport equations that need to be solved in conjunction with the governing equations.

$$\frac{\partial(\rho k)}{\partial t} + \nabla \cdot (\rho k \mathbf{u}) = \nabla \cdot \left(\frac{\mu_t}{\sigma_k}\nabla k\right) + 2\mu_t S_{ij} S_{ij} - \rho\epsilon \tag{3.11}$$

$$\frac{\partial(\rho \epsilon)}{\partial t} + \nabla \cdot (\rho \epsilon \mathbf{u}) = \nabla \cdot \left(\frac{\mu_t}{\sigma_e}\nabla \epsilon\right) + C_{1\epsilon}\frac{\epsilon}{k} 2\mu_t S_{ij} S_{ij} - C_{2\epsilon}\rho\frac{\epsilon^2}{k} \tag{3.12}$$

where S_{ij} is the mean component of the rate of deformation tensor s_{ij}, and μ_t is the eddy viscosity which is defined as:

$$\mu_t = \rho C_\mu \frac{k^2}{\epsilon} \tag{3.13}$$

The *standard* k-ϵ turbulence model uses five adjustable constants, determined using comprehensive data fitting over a wide range of turbulent flows. The canonical values of the abovementioned constants are tabulated in Table 3.1.

Table 3.1: *Standard* k-ϵ Turbulence Model Parameters

C_μ	σ_k	σ_ϵ	$C_{1\epsilon}$	$C_{2\epsilon}$
0.09	1.00	1.30	1.44	1.92

3.2 Actuator Disk Model

3.2.1 Actuator Disk Model Implementation

The actuator disk model used in this study is based on the model initially developed by Thiart and von Backström (1993). The model is implemented by using the `OpenFOAM` `C++` toolbox to extend existing `OpenFOAM` solvers. The model uses blade element theory to calculate a source term that is added to the momentum equations in the CFD solver.

The ADM uses three axially aligned disks to represent the fan being modelled. The upstream and downstream disks are used to obtain the inlet and outlet flow velocities of the fan. The average of the velocities in the two disks is used to calculate the relative velocity, U_R, and angle of attack of the flow relative to the fan's chord line, α, at a given location in the third and eponymous actuator disk. The upstream and downstream disks are located half a chord length upstream and downstream of the actuator disk.

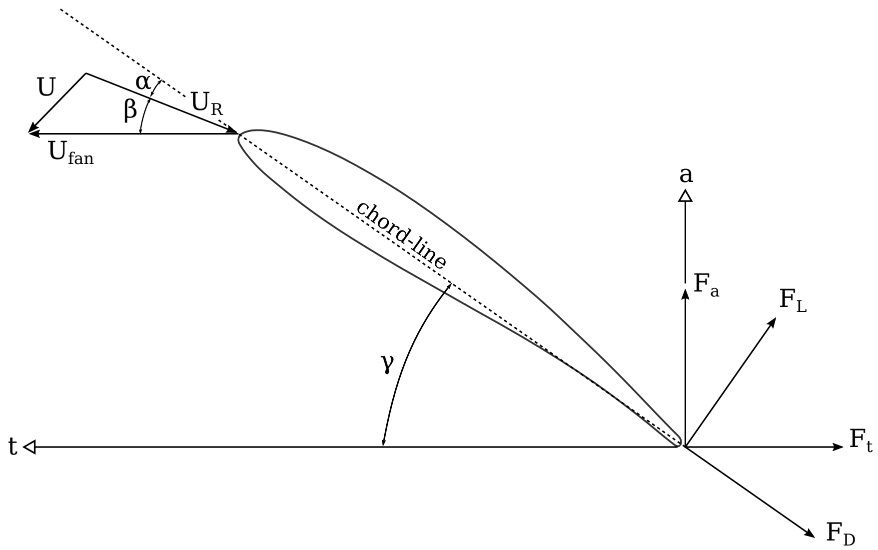

Figure 3.1: Blade Element Theory

Using blade element theory the magnitude and direction of the forces being exerted on the blade profiles, as shown in Fig. 3.1, can be calculated. The fan blades exert a corresponding reaction force on the fluid, where the reaction force is equal in magnitude but in the opposite direction. The lift and drag forces per blade segment, δF_L and δF_D respectively, are calculated using the following relations:

$$\delta F_L = \frac{1}{2}\rho |U_R|^2 C_L c \delta r \tag{3.14}$$

$$\delta F_D = \frac{1}{2}\rho |U_R|^2 C_D c \delta r \tag{3.15}$$

where C_L and C_D are the lift and drag coefficients respectfully, c is the chord length of the fan blade profile, and δr is the radial blade segment dimension.

The angle of attack of the flow relative to the blade, α, is used to determine the lift coefficient drag coefficients of the blade profile. The ADM therefore requires that the lift and drag coefficients of the fan blade profile are known for $-180° < \alpha < 180°$.

The chord line of the fan blade profile is not in plane with the actuator disk, but offset by the blade setting angle, γ. Therefore the forces determined in Eqns. (3.14) and (3.15) are converted into a cylindrical frame of reference with its corresponding tangential, axial and radial directions.

$$\delta F_t = \delta F_L \sin\beta + \delta F_D \cos\beta \tag{3.16}$$

$$\delta F_a = \delta F_L \cos\beta - \delta F_D \sin\beta \tag{3.17}$$

$$\delta F_r = 0 \tag{3.18}$$

where the average relative angle $\beta = \gamma - \alpha$.

The source term must account for the solidity, σ, of the blade at any given radius. The solidity is representative of the fraction of the circumference that is blocked by a fan blade at a given radius:

$$\sigma = \frac{n_b c}{2\pi r} \tag{3.19}$$

where n_b is the number of fan blades, and r is the radius.

The source terms in the momentum equations are added as force per unit volume which is distributed uniformly around the circumference of actuator disk according to the fan's solidity:

$$f = \frac{\delta F}{\delta V} = \frac{\sigma}{c}\frac{\delta F}{\delta r \delta t} \tag{3.20}$$

where δF is force calculated for the cell, δt is thickness of the actuator disk cells.

In summary, the axial, tangential and radial source terms added to the momentum equations in a cylindrical reference frame are defined as:

$$f_a = \frac{1}{2}\rho|U_R|^2\frac{\sigma}{\delta t}(C_L\cos\beta - C_D\sin\beta) \tag{3.21}$$

$$f_t = \frac{1}{2}\rho|U_R|^2\frac{\sigma}{\delta t}(C_L\sin\beta + C_D\cos\beta) \tag{3.22}$$

$$f_r = 0 \tag{3.23}$$

The actuator disk model is able to directly calculate the fan power consumption by integrating the tangential component of the model's source term over the actuator disk's volume:

$$\dot{W} = \omega\int_V f_t\ r\ dV \tag{3.24}$$

where ω is the fan's rotational speed, and f_t is the tangential component of the ADM's source term.

3.2.2 Ammendments to the Actuator Disk Model

Fan Lift Interference Factor

High solidity ratios are problematic when the actuator disk model is being used due to the model being derived from blade element theory for an isolated airfoil. This assumption that the fan blades operate as isolated airfoils is not valid for fans with a high solidity ratio due to the interference in the flow caused by the neighbouring fan blades.

Wallis (1983) proposes the use of an empirically obtained lift interference factor to compensate for the high solidity of the fan near the hub. The proposed lift interference factor, C_L/C_{Li}, is a function the blade's solidity over chord length, c/s, and the blade's stagger angle, ζ, and is shown in Fig. 3.2.

Connection at the Fan Hub

Many industrial axial flow fans have fan blade profiles that do not span the entire the hub-to-tip distance. The fan blade profile of these fans will often taper down to a cylindrical shaft which is fastened to the hub. The tapered fan-hub connection of one of the axial flow fans modeled later in this study is shown as an example in Fig. 3.3.

The ADM applies a linear interpolation between lift and drag coefficients of the fan's airfoil profile and that of a cylinder over the length of the tapered connection.

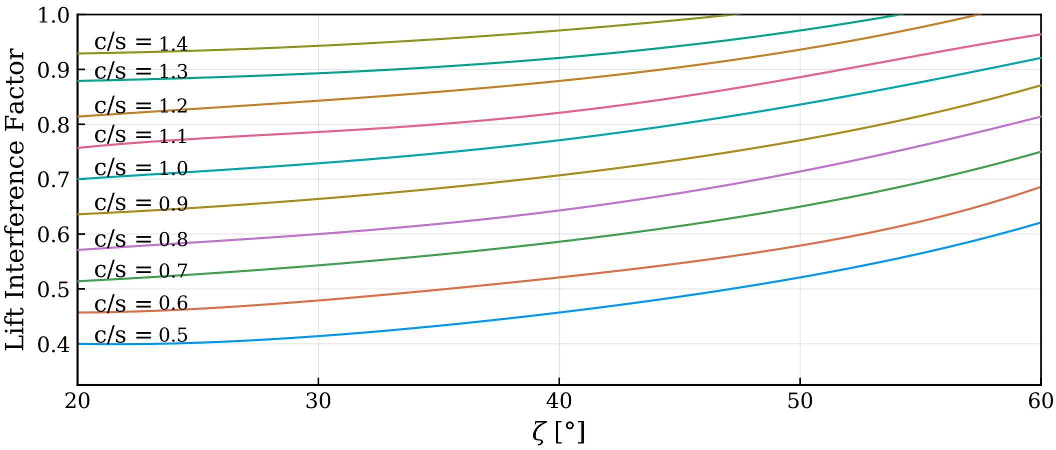

Figure 3.2: Lift Interference Factor vs ζ (Reproduced from Wallis, 1983)

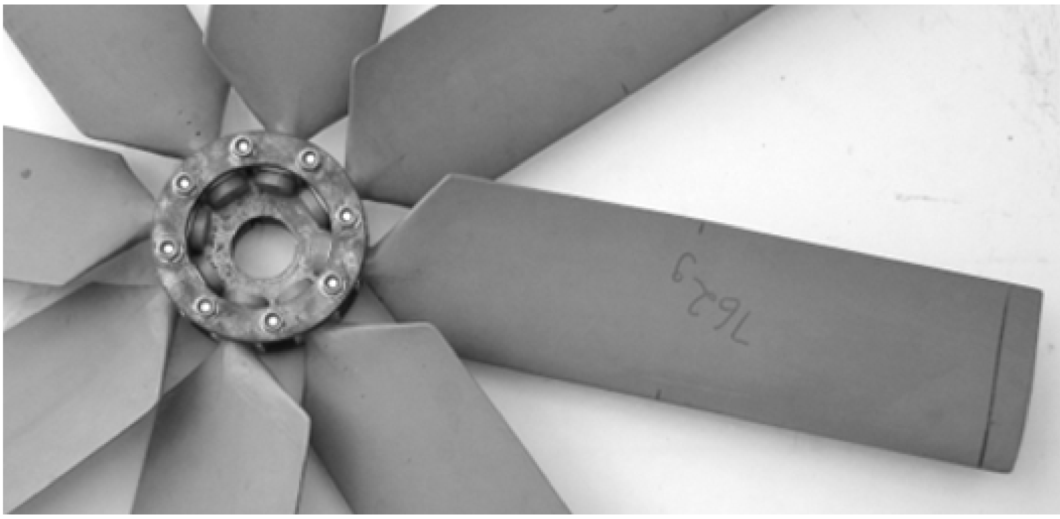

Figure 3.3: Tapered Fan-Hub Connection (L-fan)

3.3 Heat Exchanger Model

3.3.1 Heat Transfer

The Effectiveness Number of Transfer Units (ε-NTU) method is used to calculate the heat transfer from the steam to the air in the heat exchanger (Kröger, 1998). The ε-NTU method allows the heat transfer to be calculated using the difference between the vapor temperature and the air inlet temperature. The heat transfer to the air can be calculated as follows:

$$\dot{Q} = \dot{m}_a c_{pa}(T_v - T_{ai})\varepsilon_{NTU} \tag{3.25}$$

where $\dot{Q}$ is the heat transfer rate to the air, $\dot{m}_a$ is the air mass flow rate through the heat exchanger, c_{pa} is the specific heat of the air, T_v is the vapor temperature, T_{ai} is the air temperature at the inlet of the heat exchanger, and ε_{NTU} is the heat exchanger's effectiveness.

Heat exchangers, such as those found in ACCs, often contain multiple rows of finned tubes which facilitate the heat transfer. The heat transfer is calculated for each individual row, using the air outlet temperature of the previous row as the inlet temperate for the next tube row. The heat transfer for all the rows are added up and distributed across the individual cells in the heat exchanger.

Assuming a constant vapor temperature during the condensation process the heat transfer effectiveness is given by the following relation (Kröger, 1998):

$$\varepsilon = 1 - \exp\left(\frac{\left((h_a A_x)^{-1} + (h_c A_c)^{-1}\right)^{-1}}{\dot{m}_a c_{pa}}\right) \tag{3.26}$$

where h_a is the air-side heat transfer coefficient, A_x is the heat exchanger's cross sectional area, h_c is the condensation heat transfer coefficient, A_c is the condensate heat transfer area, $\dot{m}_a$ is the air mass flow rate, and c_{pa} is the specific heat capacity of the air (isobaric).

3.3.2 Heat Exchanger Pressure Drop

The pressure drop over the heat exchanger is calculated using the Darcy-Forchheimer porosity model. The Darcy-Forchheimer porosity model adds a resistance source term to the momentum equations. The one-dimensional pressure drop per unit length is calculated using the following equation:

$$\frac{\partial p}{\partial x} = \mu k_d U + \rho k_f \frac{U^2}{2} \tag{3.27}$$

where μ is the dynamic viscosity of the fluid, ρ is the fluid density, U is the fluid velocity, and k_d and k_f are the Darcy-Forchheimer coefficients.

The pressure drop characteristic curves of the heat exchangers being modelled are available from previous experimental tests. From dimensional analysis the Darcy-Forchheimer coefficients are calculated by fitting a second order polynomial through the experimental data and performing a conversion.

$$\Delta p = A \cdot U + B \cdot U^2 \tag{3.28}$$

$$k_d = \frac{A}{\mu \Delta x} \tag{3.29}$$

$$k_f = \frac{2B}{\rho \Delta x} \tag{3.30}$$

For three-dimensional fluid flows the Darcy-Forchheimer coefficients can be set uniquely for each direction, creating an anisotropic porous medium. The flow in the heat exchanger occurs along the primary axis of the heat exchanger, i.e. from inlet to outlet. The Darcy-Forchheimer coefficients for the primary axis are set according to the experimental data. The coefficients for both secondary axes are set to arbitrarily large values (multiple orders of magnitude larger) so as to coerce the flow direction along the primary axis of the heat exchanger.

3.4 Crosswinds

The crosswinds in this study are simulated by applying an Atmospheric Boundary Layer (ABL) (Hargreaves and Wright, 2007) at the inlet boundary of the atmospheric domain. The velocity profile for a given reference velocity, U_{ref}, at a given reference height, z_{ref}, is specified as:

$$U = \frac{U_{ref}}{ln\left(\frac{Z_{ref}+z_0}{z_0}\right)}\, ln\left(\frac{z+z_0}{z_0}\right) \tag{3.31}$$

where z is the vertical coordinate, z_0 is the surface roughness (default of 0.1 m) and z_g is the z-coordinate at ground level.

The crosswind profiles for reference velocities of 3, 6 and 9 m/s at a reference height of 60 m (which is the reference height used in the simulations in this study) are shown in Fig. 3.4.

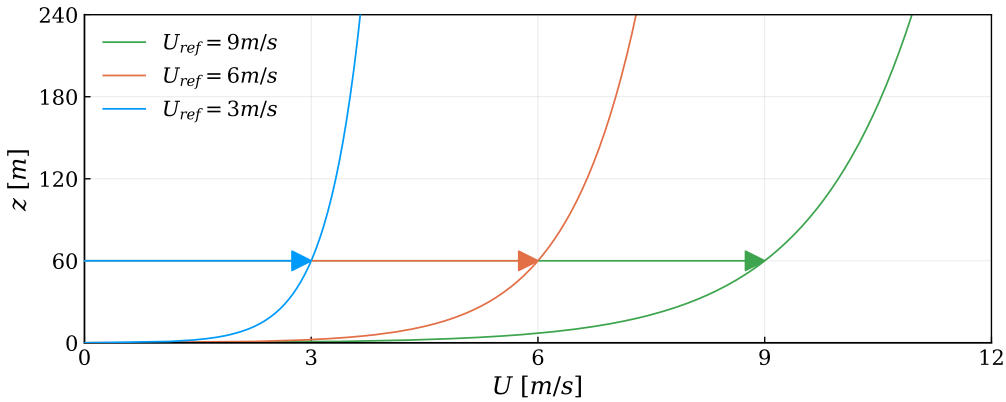

Figure 3.4: Crosswind Profiles

Chapter 4

Forced Draft ACC Model Development

4.1 Fan Profile Lift & Drag Coefficients

Two commercially available axial flow fans are investigated in this study: an 8-bladed axial flow fan identified as the L-fan and a 9-bladed axial flow fan identified as the N-fan. The actuator disk model requires the lift and drag coefficient of the fans' airfoil profiles in order to calculate the source terms to be added to the momentum equations.

4.1.1 Fan Profiles

The L-fan and N-fan have different airfoil profiles and chord lengths, but share a similar diameter and hub-to-tip ratio. The airfoil profiles of the L-fan and N-fan at different radii are shown in Figs. 4.1 and 4.2 respectively. Note that the chord length of both fan's airfoils remains constant throughout the length of the fan blade. Similarly, the airfoil profiles is constant for the L-fan throughout the length of the fan blade, and is constant for the N-fan from 3 m radially outwards.

The fan blade twist along the radial axis of the L-fan and the N-fan is shown in Fig. 4.3. The twist is shown from the hub radius to the tip radius, with the blade setting angle set to zero.

4.1.2 Numerical Analysis

The lift and drag coefficients are dependent on the fan blade's airfoil profile and the angle of attack, α, with regard to the flow field. The lift and drag

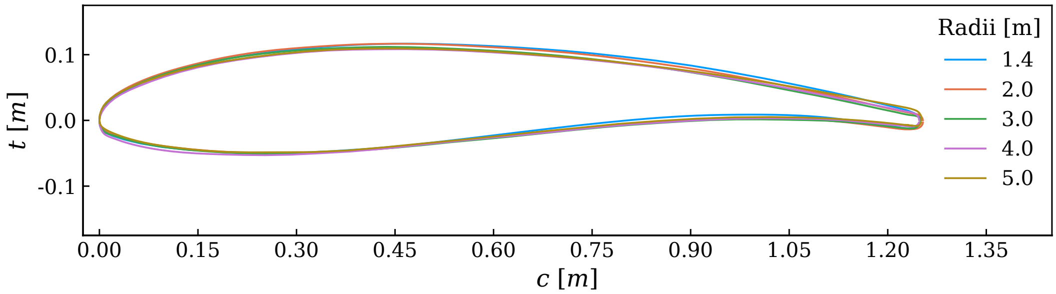

Figure 4.1: L-Fan Airfoil Profiles at Different Radii

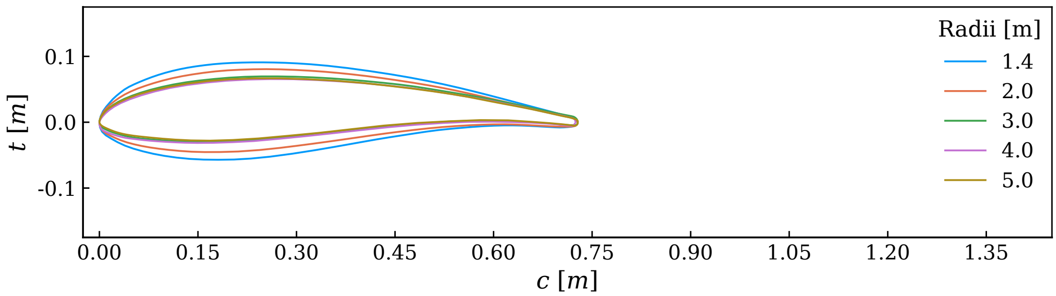

Figure 4.2: N-Fan Airfoil Profiles at Different Radii

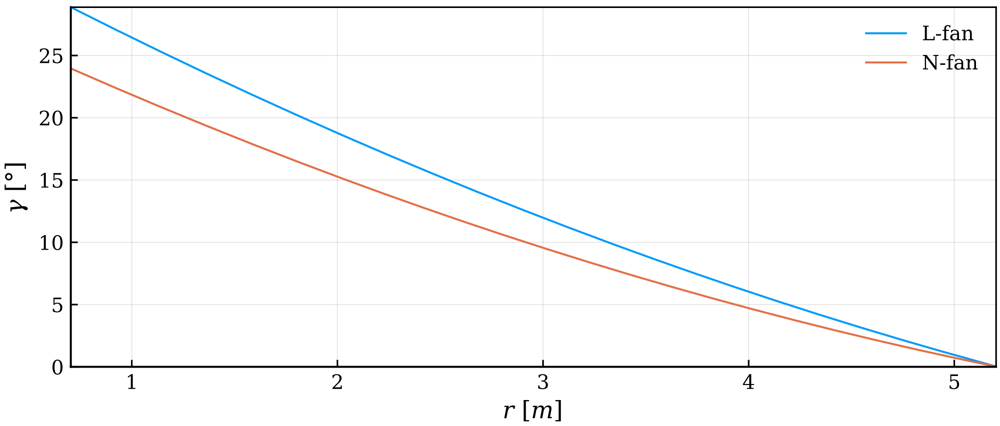

Figure 4.3: Fan Blade Twist (γ) vs Radius (r)

coefficients are respectively defined as:

$$C_L = \frac{F_L}{\frac{1}{2}\rho U^2 A} \tag{4.1}$$

$$C_D = \frac{F_D}{\frac{1}{2}\rho U^2 A} \tag{4.2}$$

Following the methodology used by van der Spuy (2011) and Wilkinson (2017), the lift and drag coefficients for the fan blade profiles were calculated using the `XFoil` software program. `XFoil` uses a combination of panel methods and viscous/inviscid interaction methods to solve the boundary layer around the airfoil (Drela, 1989). Consequently, the computational time required for these simulations is significant orders of magnitude less than when using CFD simulations (van der Spuy, 2011).

`XFoil` is used to calculate the lift and drag coefficients for angles of attack between the upper and lower stall points of the airfoil. Hoerner (1965) recommends using flat plate theory to extend the lift and drag coefficient curves beyond its stall points. The `XFoil` curves are superimposed over the flat plate curves. A gradual interpolation is used beyond the stall limits of the `XFoil` curves to ensure a smooth transition to the flat plate theory. It should be noted that when the fan is at normal operating conditions the majority of the flow's angles of attack with the fan blades are well within the range delimited by the airfoil's stall points.

The lift and drag coefficients of the L-fan and the N-fan at various Reynolds numbers are shown in Figs. 4.4 and 4.5. The lift and drag coefficients are shown over a range of angles of attack extending beyond the stall limits of the airfoils.

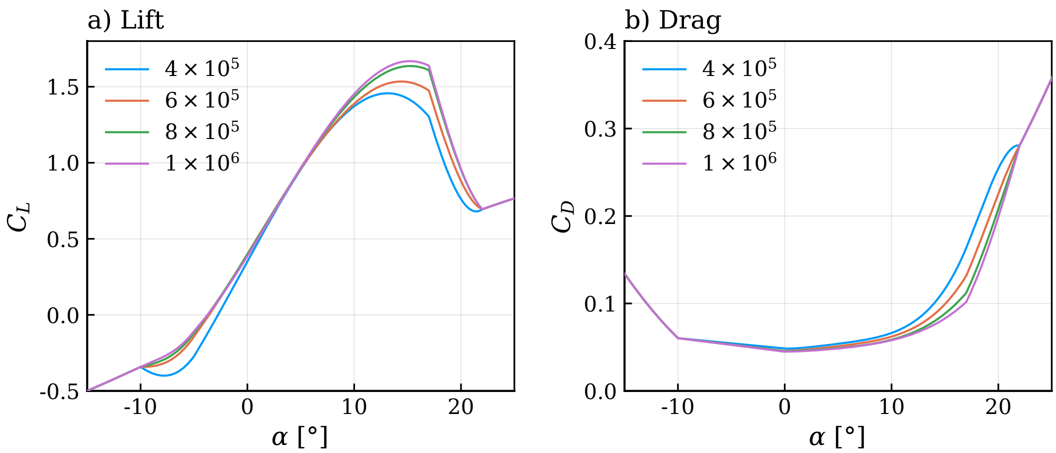

Figure 4.4: L-Fan Lift & Drag Coefficients at Various *Re* Numbers

The initial CFD simulations under-predicted the power consumption for the two fans. The under-predicted power was traced to under-predicted drag coefficients for both fans obtained from `XFoil` at small angles of attack. A constant offset was added to the `XFoil` drag coefficient polynomials to increase the drag. The increased drag coefficient primarily influences the tangential forces

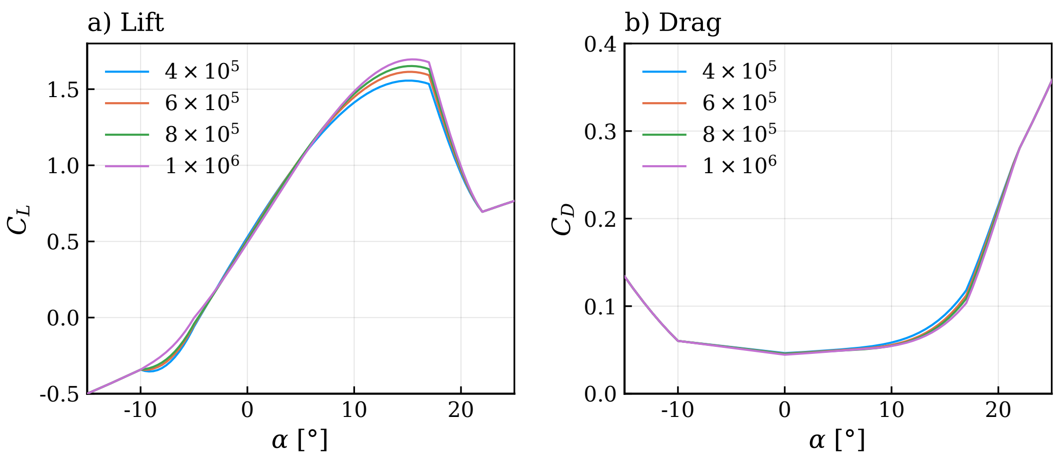

Figure 4.5: N-Fan Lift & Drag Coefficients at Various *Re* Numbers

imparted on the airfoil (see Eqn. (3.23)), which is then used to calculate the fan shaft power.

4.2 Incompressible Axial Flow Fan Model

4.2.1 Computational Domain

The actuator disk model implementations of the N-fan and L-fan are validated against experimental data obtained from a at the Department of Mechanical and Mechatronic Engineering at Stellenbosch University (Augustyn, 2013).

A schematic representation of the BS 848 facility, as shown in Fig. 4.6, is modeled using a 3-dimensional computational domain based on that of Bredell (2005). The representation of the computational domain is shown in Fig. 4.7.

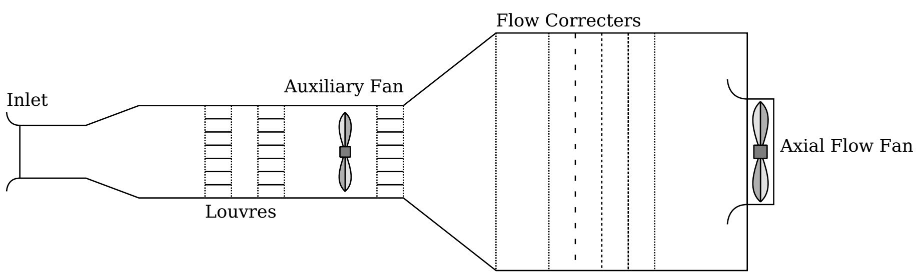

Figure 4.6: Schematic Drawing of the BS 848 Facility

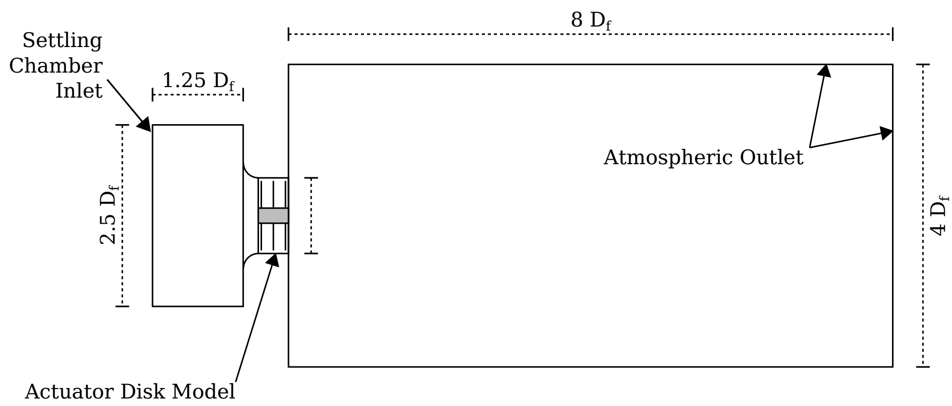

Figure 4.7: BS 848 Computational Domain Schematic

4.2.2 Computational Mesh

The computational domain is discretized into a computational mesh so that the flow can be solved numerically. The domain is split into two separate regions, the actuator disk region and the rest of the facility, which are meshed separately.

A cross-sectional slice through the computational mesh is shown in Fig. 4.8. The actuator disk region is meshed using a fully structured hexahedral mesh, and the remainder is meshed using an unstructured tetrahedral mesh.

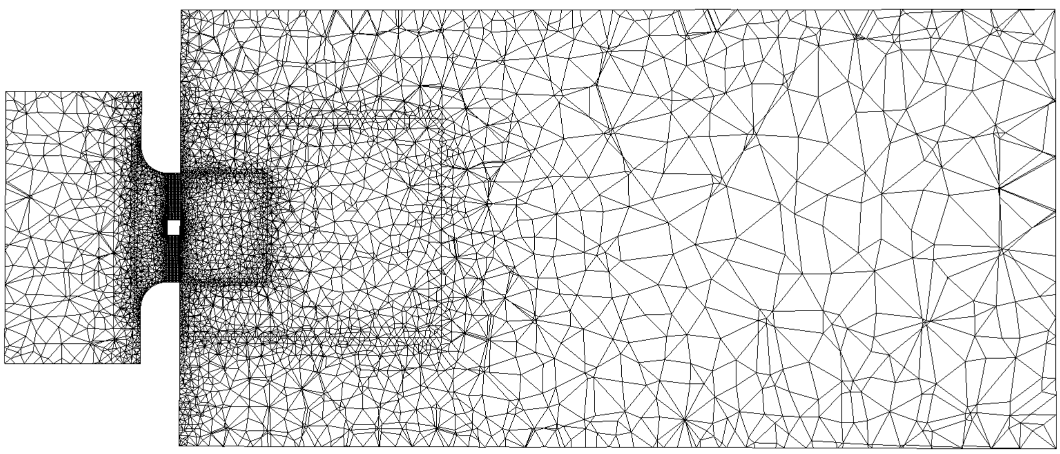

Figure 4.8: BS 848 Mesh Cross-Sectional Slice (Incompressible)

The computational domains for both the N-fan and L-fan simulations were meshed using 5.94×10^5 cells. The cell density of the mesh increases near the actuator disk region of the domain where greater accuracy in calculating the flow field is required.

4.2.3 Boundary Conditions

The boundary conditions used for the incompressible flow BS 848 simulations are tabulated in Table 4.1.

Table 4.1: BS 848 Boundary Conditions (Incompressible)

Field	Boundary	Type	Value
p	Inlet	`zeroGradient`	$\nabla p_\perp = 0$
	Outlet	`totalPressure`	p_{ref}
	Walls	`zeroGradient`	$\nabla p_\perp = 0$
U	Inlet	`fixedValue`	U_{ref}
	Outlet	`zeroGradient`	$\nabla U_\perp = 0$
	Walls	`noSlip`	$U = 0$

A total pressure boundary condition is used to constrain the pressure at the outlet of the domain with the reference pressure, p_{ref}, set to 101325 Pa. A zero-gradient boundary condition is used to constrain the pressure at the inlet of the domain.

A fixed value boundary condition is used to set a uniform velocity field at the inlet of the domain, with multiple reference velocities, U_{ref}, used to test the fan model at various volumetric flow rates. A zero-gradient boundary condition is used to set the velocity at the outlet of the domain.

Standard wall-functions are used for the *standard* k-ϵ turbulence model. Zero-gradient boundaries were used for the k and ϵ fields.

4.2.4 Results

The fan static pressure results for the L-fan and N-fan are shown in Figs. 4.9 and 4.10 respectively. The predicted operating regions of the two fans are also shown. The results shown for volumetric flow rates near the predicted operating regions of the two fans correlate well with the experimental results obtained by Augustyn (2013). The numerical results start to deviate from the experimental results at low volumetric flow rates.

The fan shaft power consumption for the L-fan and N-fan are shown in Figs. 4.11 and 4.12 respectively. The results are compared to the experimental results which show good correlations within the fan's operating regions.

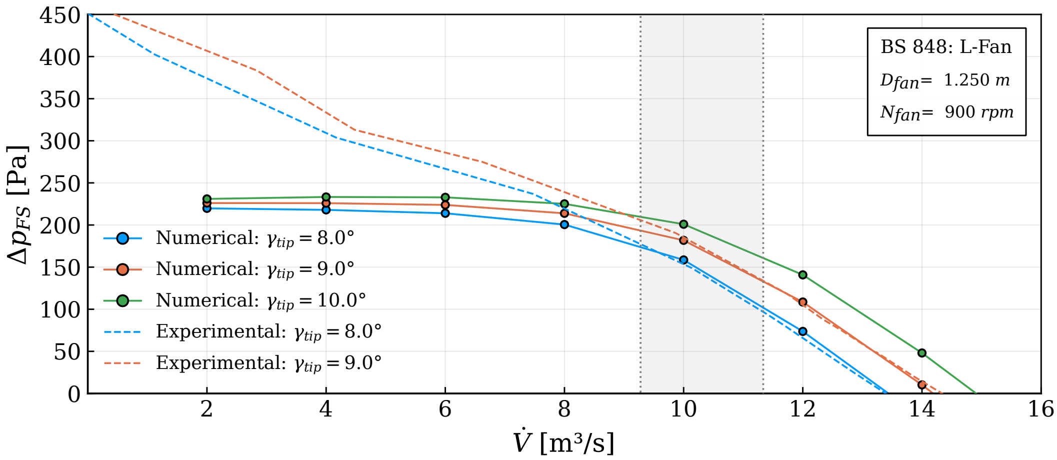

Figure 4.9: L-Fan Fan Static Pressure (Incompressible) vs. Volumetric Flow Rate

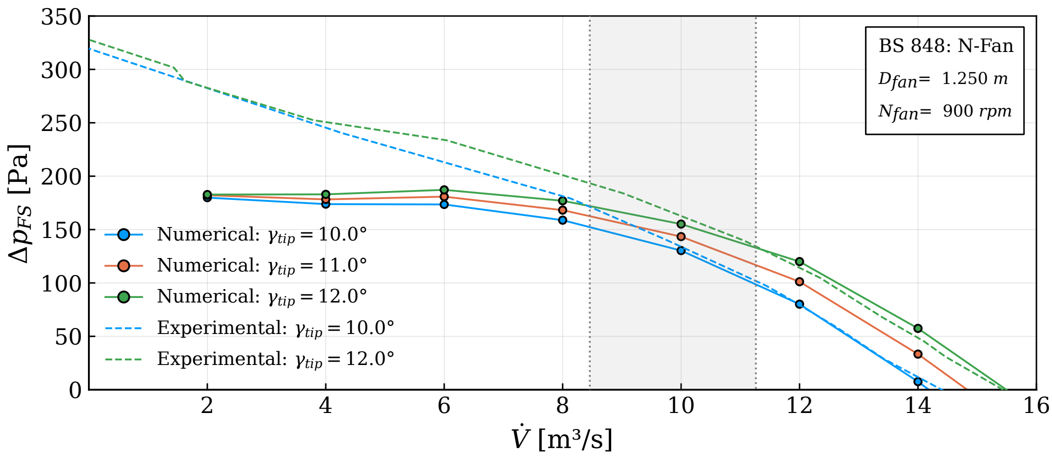

Figure 4.10: N-Fan Fan Static Pressure (Incompressible) vs. Volumetric Flow Rate

The fan efficiency characteristic curves for the L-fan and N-fan are shown in Figs. 4.13 and 4.14 respectively. The fan efficiency is derived from the fan static pressure and fan power consumption and therefore the results exhibit the same correlation with experimental results within the operating region of the two fans.

4.2.5 Conclusions

The results from the fan simulations correlate well with the experimental results obtained by Augustyn (2013) validating the incompressible implementation of the actuator disk model.

The under-predicted fan static pressure at the lower flow rates is expected

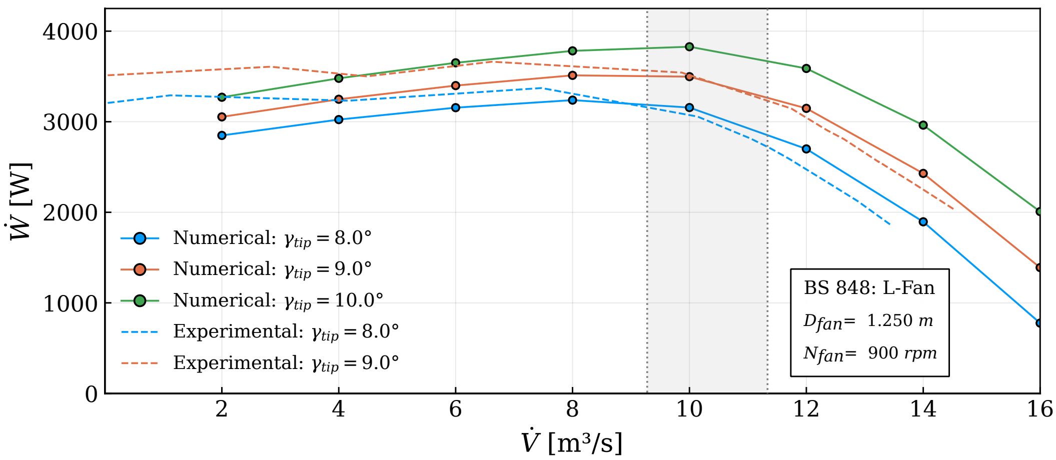

Figure 4.11: L-Fan Shaft Power (Incompressible) vs. Volumetric Flow Rate

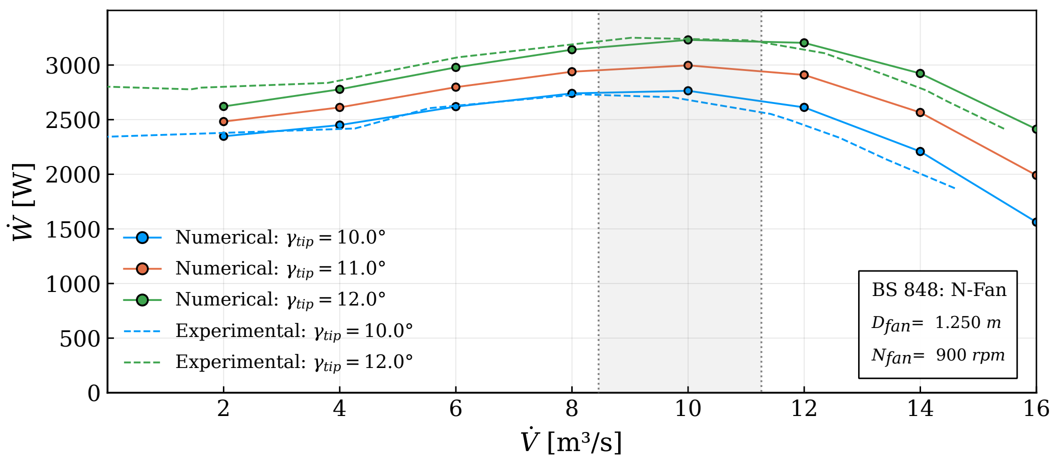

Figure 4.12: N-Fan Shaft Power (Incompressible) vs. Volumetric Flow Rate

when using the actuator disk model (see § 2.2). The lower flow rates are well below the predicted operating points of the two fans when installed within an ACC unit. The deviations should not affect the investigation of the ACC's fan configuration as similar deviations are expected for both of the axial flow fans.

4.3 Incompressible Heat Exchanger Model

The heat exchanger modeled is based on an elliptical finned tube heat exchanger tested by Zietsman and Kröger (2010).

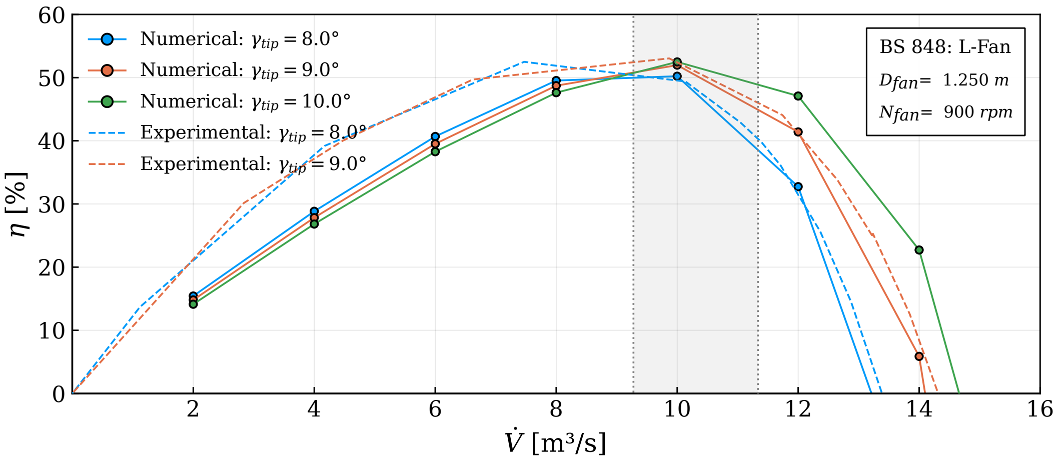

Figure 4.13: L-Fan Static Efficiency (Incompressible) vs. Volumetric Flow Rate

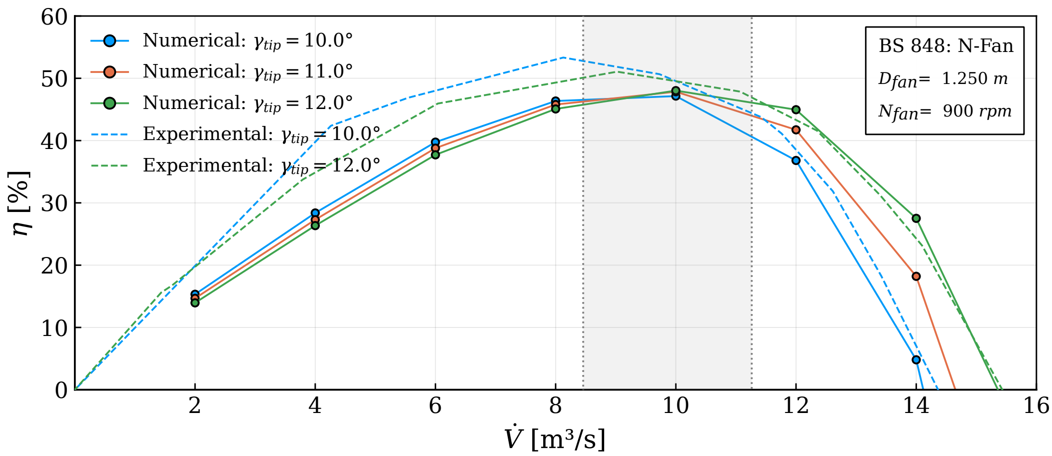

Figure 4.14: N-Fan Static Efficiency (Incompressible) vs. Volumetric Flow Rate

4.3.1 Experimental Characteristics

The heat exchanger characteristics were obtained in an experimental wind tunnel at the Department of Mechanical and Mechatronic Engineering at Stellenbosch University (Zietsman and Kröger, 2010). A schematic representation of the test wind tunnel is given in Fig. 4.15.

The heat exchanger characteristics were obtained at various mass flow rates. The dimensionless Reynolds number, Re, and Nusselt number, Nu, were scaled using the characteristic dimensions of the experimental heat exchanger (Kröger, 1998). The *characteristic* Reynolds number, Ry, and *characteristic*

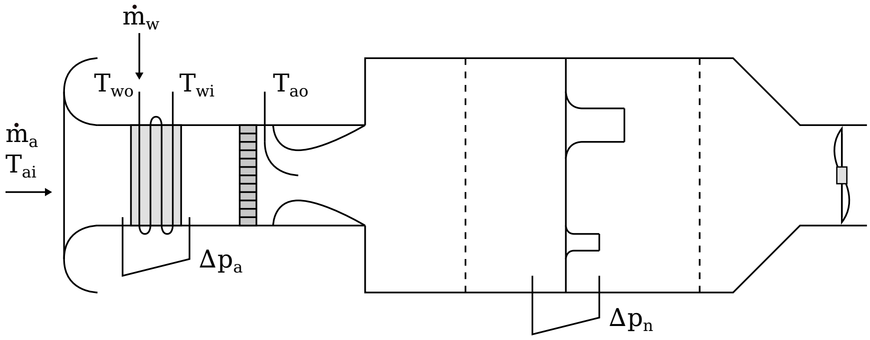

Figure 4.15: Heat Exchanger Experimental Windtunnel (Kröger, 1998)

Nusselt number, Ny, are defined as:

$$Ry = \frac{\dot{m}}{\mu A_{fr}} \tag{4.3}$$

$$Ny = \frac{h\ A_s}{k\ A_{fr}\ Pr^{0.333}} \tag{4.4}$$

where Pr is the Prandtl number of the flow.

The experimental heat transfer characteristic for the heat exchanger is modelled as:

$$Ny = aRy^b \tag{4.5}$$

The experimental pressure drop characteristics across the heat exchanger are defined for non-isothermal and isothermal flows as:

$$K_{he-nonisothermal} = c_1 Ry^{d_1} \tag{4.6}$$

$$K_{he-isothermal} = c_2 Ry^{d_2} \tag{4.7}$$

where K_{he} is the pressure drop coefficient which defines the heat exchanger's pressure drop as:

$$\Delta p_{he} = K_{he}\frac{(\dot{m}/A)^2}{2\rho} \tag{4.8}$$

4.3.2 Computational Domain

The computational domain used in the heat exchanger simulations is shown in Fig. 4.16, and the domain's dimensions are tabulated in Table 4.2.

4.3.3 Computational Mesh

The discretized computational domain is shown in Fig. 4.17. The computational mesh consists completely of hexahedral cells, using a total of 13824 cells to discretize the domain.

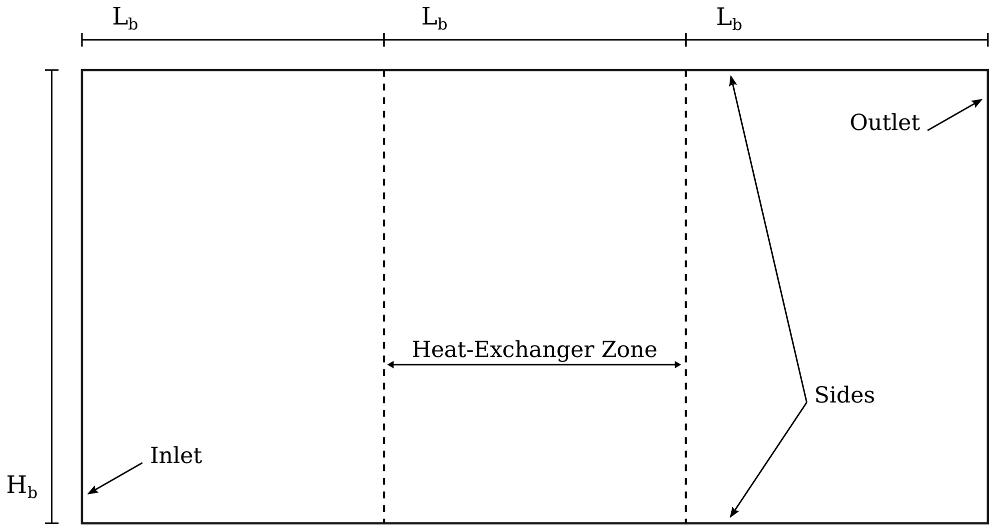

Figure 4.16: Heat Exchanger Domain Schematic (Incompressible)

Table 4.2: Heat Exchanger Domain Dimensions (Incompressible)

Dimension	Value	
H_b	0.47	m
L_b	0.30	m

4.3.4 Boundary Conditions

The boundary conditions used for the incompressible flow heat exchanger simulations are tabulated in Table 4.3.

Table 4.3: Heat Exchanger Boundary Conditions (Incompressible)

Field	Boundary	Type	Value
p	Inlet	`totalPressure`	p_{ref}
	Outlet	`zeroGradient`	$\nabla p_{\perp} = 0$
	Sides	`zeroGradient`	$\nabla p_{\perp} = 0$
U	Inlet/Outlet/Sides	`fixedValue`	U_{ref}
T	Inlet	`fixedValue`	T_{ref}
	Outlet	`zeroGradient`	$\nabla T_{\perp} = 0$
	Sides	`zeroGradient`	$\nabla T_{\perp} = 0$

A total pressure boundary condition is used to constrain the pressure at the inlet of the domain with the reference pressure, p_{ref}, set to 100236 Pa. A zero-gradient boundary condition is used to constrain the pressure at the outlet and sides of the domain.

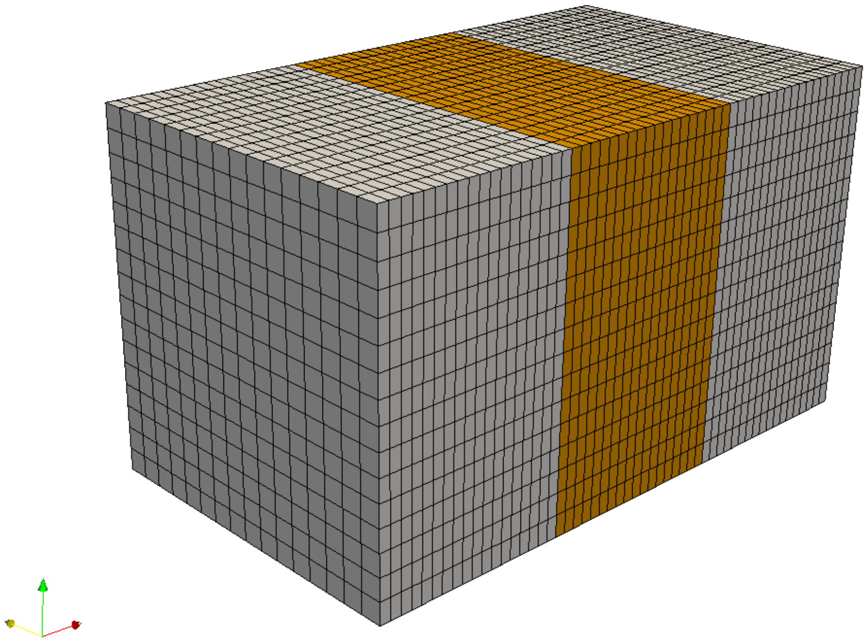

Figure 4.17: Heat Exchanger Domain Mesh (Incompressible)

A fixed value boundary condition is used to set a uniform velocity field at all the boundaries of the domain. Multiple reference velocities, U_{ref}, were used to test the heat exchanger model at various volumetric flow rates.

A fixed value boundary condition is used to set a uniform temperature field at the inlet of the domain, with the reference temperature, T_{ref}, is set to match that measured for each experimental flow rate. A zero gradient boundary condition is used to set the temperature at the outlet and sides of the domain.

Standard wall-functions are used for the *standard* k-ϵ turbulence model. Zero-gradient boundaries were used for the k and ϵ fields.

4.3.5 Results

The numerical results from the Heat Exchanger simulations correlate well with the experimental results (Zietsman and Kröger, 2010). The Darcy-Forchheimmer porosity model provides a near perfect static pressure drop over the heat exchanger as shown in Fig. 4.18. The heat transfer rate to the airflow correlates reasonably well with the experimental results. The correlation between the numerical and experimental heat transfer rates deviates at the lower flow rates, where it is under-predicted, and at the higher flow rates, where it is over-predicted, Fig. 4.19.

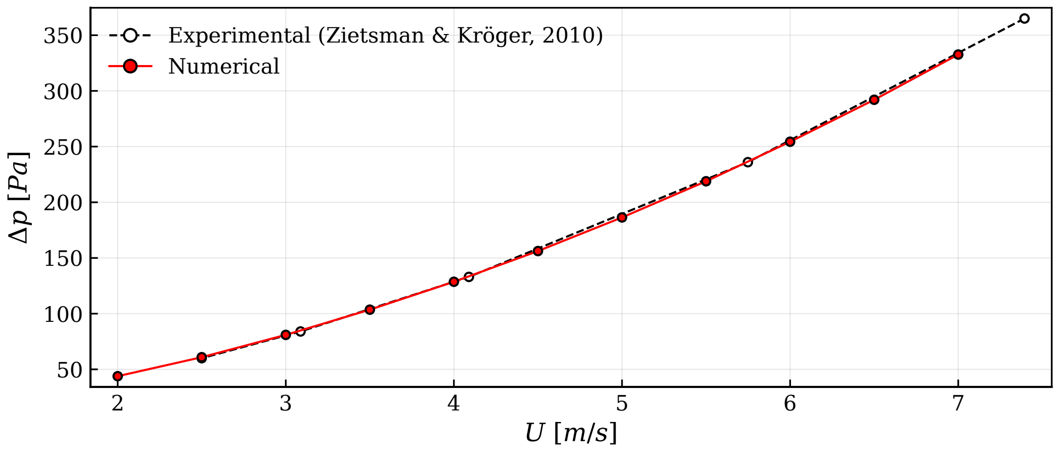

Figure 4.18: Heat Exchanger Isothermal Pressure Drop (Incompressible)

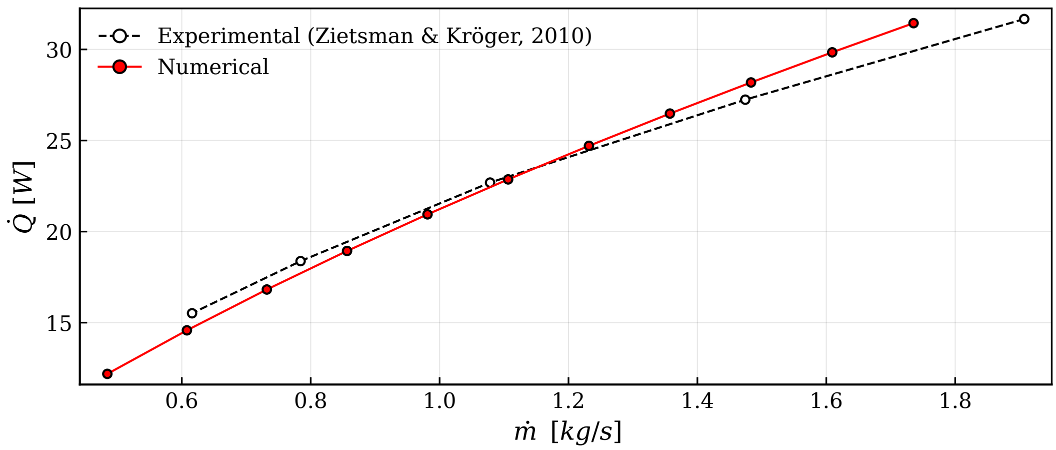

Figure 4.19: Heat Exchanger Heat Transfer Rate (Incompressible)

The differences between the heat transfer rates are attributed to the use of an incompressible solver (see § 3.1.2). The volumetric expansion of the fluid as it is heated does not occur due to use of a constant fluid density in the solver. Due to the methodology used to implement the heat transfer model, this phenomena of increased volumetric flow rate increases the calculated heat transfer to the fluid.

4.3.6 Conclusions

The heat exchanger model is capable of accurately simulating the pressure drop across the heat exchanger. The numerical heat transfer correlates reasonably well with experimental data at moderate flow rates.

It should be noted that the model does accurately predict the heat transfer to the airflow at certain flow rates, specifically those closer to the expected operating point of the heat exchanger (when installed in the ACC).

4.4 Single Fan Forced Draft ACC Model

4.4.1 Analytical Model

A draft equation as defined by Kröger (1998) is used to derive a one-dimensional analytical model for preliminary analysis of the Single Fan Forced Draft ACC. The results of the draft equation are used as a reference point to compare the CFD results against.

The draft equation is defined as:

$$\Delta p_{total} = \sum_{i}^{n} K_i \frac{(\dot{m}_{ai}/A_i)^2}{2\rho_{ai}} - \Delta p_{fan} + \Delta p_{height} \tag{4.9}$$

where Δp_{total} is the total pressure change over the entire fan-unit, K_i are losses associated with obstruction in the flow path, Δp_{fan} is the fan static pressure rise and Δp_{height} is the pressure rise due to changes in height. The various losses are available in Appendix B.

The draft equation is solved uniquely for both the full scale L-fan and the N-fan, with the results tabulated in Table 4.4. The full scale L-fan and N-fan characteristics used in the draft equation are obtained by scaling the experimental model scale characteristics using the fan affinity laws (Eqns. (B.3) to (B.5) found in Appendix B).

Table 4.4: Single Fan Forced Draft ACC Analytical Solution

Perfomance Characteristic		**L-Fan**	**N-Fan**	
Fan Blade Angle	γ_{tip}	9	10	°
Volumetric Flow Rate	$\dot{V}$	725.90	661.85	m^3/s
Fan Pressure Rise	Δp	123.80	105.50	Pa
Fan Shaft Power	$\dot{W}$	177.62	138.59	kW
Heat Transfer	$\dot{Q}$	18.36	17.10	MW

4.4.2 Computational Domain

The computational domain for the Single Fan Forced Draft ACC Model is created with a single ACC fan-unit embedded inside a larger atmospheric domain. The ACC unit has additional windwalls added to its sides, similar to full sized Multiple Fan ACC units. The computational domain is shown in Fig. 4.20, and the domain dimensions are tabulated in Table 4.5.

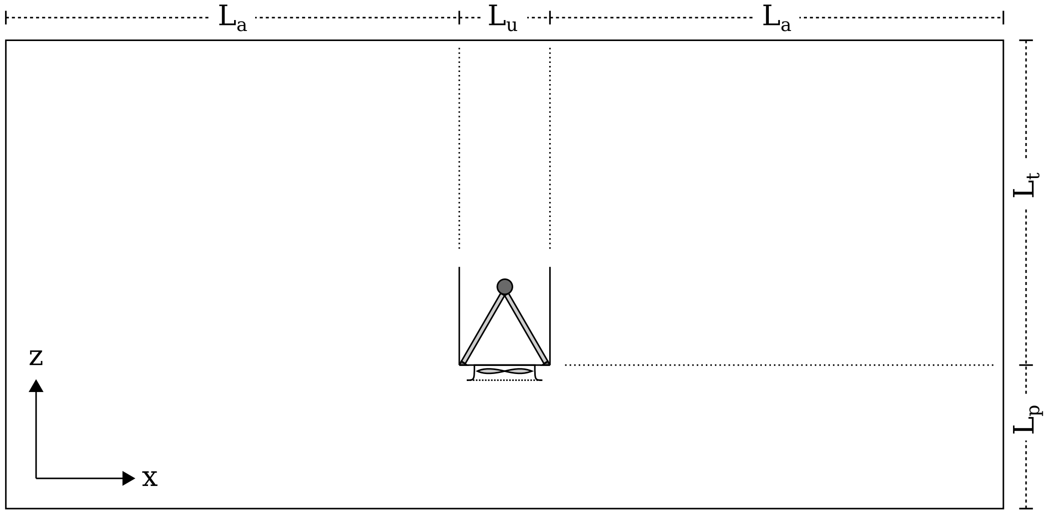

Figure 4.20: Single Fan Forced Draft ACC Domain

Table 4.5: Single Fan Forced Draft Dimensions

Dimension	**Symbol**	**Value**	
Unit Width	L_u	12.5	m
Platform Height	L_p	60.0	m
Distance to Atmospheric Sides	L_a	150.0	m
Distance to Atmospheric Top	L_t	240.0	m

4.4.3 Computational Mesh

The domain and mesh for the Single Fan Forced Draft ACC are created in a modular fashion allowing for each individual component to be meshed according to specific requirements. The modular design also allows reuse of the individual components in the construction of the Multiple Fan Forced Draft ACC model's mesh later in the study. The submesh components created to form the entire computational domain are listed in Table 4.6.

The computational domain is discretized using a total of 2.66×10^6 cells which have a mean 5.7 faces per cell and a mean non-orthogonality of 5.9°. The mesh

Table 4.6: Single Fan Forced Draft ACC Submesh Components

Submesh Region	Mesh Type	
Actuator Disk	Hexahedral	Structured
Heat Exchanger	Hexahedral	Structured
Fan-Unit Lower	Tetrahedral	Unstructured
Fan-Unit Plenum	Tetrahedral	Unstructured
Fan-Unit Upper	Tetrahedral	Unstructured
Atmosphere	Hexahedral	Structured

consists of 2.24×10^6 hexahedral cells which are primarily used to discretize the atmospheric region of the domain. The remainder of the domain is meshed using 388×10^3 tetrahedral cells which are used to discretize the complex geometry of the fan-unit. A small number of polyhedral cells (26×10^3) remain as artifacts of mesh refinement.

An isolated section of the initial mesh around the ACC region is shown in Fig. 4.21. The isolated section shows the refinement of the structured hexahedral atmospheric submesh component in the vicinity of the ACC region. The refinement is applied to the atmospheric domain's structured hexahedral mesh around the fan-unit region. The refinement is achieved using successive applications of cell-splitting using consecutively smaller refinement regions. The fan-unit region's unstructured tetrahedral mesh itself is initially created with the desired mesh resolution and is not refined.

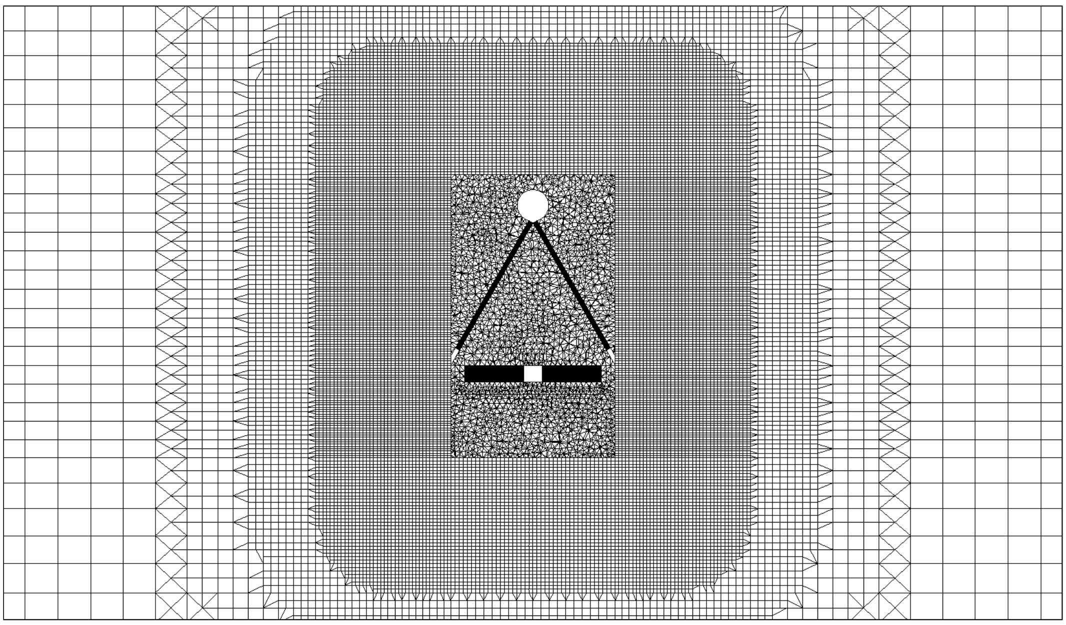

Figure 4.21: Single Fan Forced Draft ACC Mesh

4.4.4 Boundary Conditions

The Single Fan Forced Draft ACC Model's boundary conditions are set to match atmospheric conditions. The boundary conditions used are tabulated in Table 4.7. The ambient conditions for the simulation are calculated using a reference pressure, p_{ref}, of 101325 Pa and a reference temperature, T_{ref}, of 300 K.

Table 4.7: Single Fan Forced Draft ACC Boundary Conditions

Field	Boundary	Type	Value
p'	Sides/Top	`totalPressure`	p_{ref}
	Walls	`zeroGradient`	$\nabla p'_{\perp} = 0$
U	Sides	`pressureInletOutletVelocity`	$\nabla U_{\perp} = 0$
	Walls	`noSlip`	$U = 0$
T	Sides	`inletOutlet`	T_{ref}, $\nabla T_{\perp} = 0$
	Walls	`zeroGradient`	$\nabla T_{\perp} = 0$

The `OpenFOAM` incompressible flow solver with Boussinesq bouyancy solves for an alternative pressure field, p', which is obtained by subtracting the hydrostatic component from the actual pressure:

$$p' = p - \rho g h \tag{4.10}$$

The actual pressure, p, is obtained when necessary by back substitution.

A total pressure boundary condition is used at the atmospheric boundaries with the reference pressure, p_{ref}. Zero-gradient boundary conditions are used for the pressure field at the walls of the ACC.

The `OpenFOAM` specific `pressureInletOutletVelocity` velocity boundary condition is used to for atmospheric boundaries. For inflow conditions the internal flow field is used to determine the inlet flux, while for outflow conditions a zero-gradient boundary condition is used.

The `OpenFOAM` specific `inletOutlet` boundary condition is used to set the temperature at the atmospheric boundaries of the domain. Under inflow conditions the boundary is specified using a reference temperature, T_{ref}, set to 300 K, while under outflow conditions a zero-gradient boundary condition is used.

Standard wall-functions are used for the *standard* k-ϵ turbulence model. Zero-gradient boundaries were used for the k and ϵ fields.

4.4.5 Results

Operating Points At Multiple Fan Angles

The flow field for the Single Fan ACC is solved for a range of different fan blade angles, γ_{tip}. The results of the simulations are used to determine how sensitive the Single Fan ACC model is to changes in the fan blade angles. The fan blade angles used are tabulated in Table 4.8.

Table 4.8: Single Fan Forced Draft ACC Blade Angles

Fan	**Blade Angles**
L-Fan	$\gamma_{tip} \in \{8.0°, 8.5°, 9.0°, 9.5°, 10.0°, 10.5°\}$
N-Fan	$\gamma_{tip} \in \{10.0°, 10.5°, 11.0°, 11.5°, 12.0°, 12.5°\}$

The results of the simulations are tabulated in Table 4.9. The results show a consistent increase in the volumetric flow rate, $\dot{V}$, fan power consumption, $\dot{W}$, and heat transfer, $\dot{Q}$, for each 0.5° increase in fan blade angle.

Table 4.9: Single Fan Forced Draft ACC Results

L-Fan	8.0°	8.5°	9.0°	9.5°	10.0°	10.5°	
$\dot{V}$	699.25	712.89	726.64	740.05	753.53	766.72	$m^3/2$
$\dot{W}$	159.55	167.18	174.97	183.14	191.63	200.37	kW
$\dot{Q}$	16.18	16.43	16.68	16.91	17.16	17.39	MW

N-Fan	10.0°	10.5°	11.0°	11.5°	12.0°	12.5°	
$\dot{V}$	663.29	674.17	684.71	695.39	705.94	716.32	$m^3/2$
$\dot{W}$	139.60	145.89	152.29	158.90	165.57	172.29	kW
$\dot{Q}$	15.55	15.75	15.94	16.14	16.33	16.51	MW

The L-fan results show that the volumetric flow rate increases at a rate of 27 $m^3/s/°$, the fan power consumption increases at a rate of 16 kW/° and the total heat transfer increases at a rate of 0.5 MW/°. The N-fan results show that the volumetric flow rate increases at a rate of 21 $m^3/s/°$, the fan power consumption increases at a rate of 13 kW/° and the total heat transfer increases at a rate of 0.4 MW/°.

Comparison to Analytical Draft Equation

The numerical results of the Single Fan Forced Draft ACC model are compared against the operating points obtained by solving the analytical draft equation Eqn. (4.9). A comparison of the numerical results and the analytical draft equation results are tabulated in Table 4.10.

Table 4.10: Single Fan Forced Draft ACC Draft Equation Validation

L-Fan ($\gamma_{tip} = 9°$)		**Analytic**	**Numerical**	
Volumetric Flow Rate	$\dot{V}$	725.90	726.64	m^3/s
Fan Power	$\dot{W}$	177.62	174.97	kW
Heat Transfer	$\dot{Q}$	18.36	16.68	MW

N-Fan ($\gamma_{tip} = 10°$)		**Analytic**	**Numerical**	
Volumetric Flow Rate	$\dot{V}$	661.85	663.29	m^3/s
Fan Power	$\dot{W}$	138.59	139.60	kW
Heat Transfer	$\dot{Q}$	17.10	15.55	MW

The numerical L-fan and N-fan flow field results correlate well with the analytical draft equation results. The numerical volumetric flow rate is 0.1% greater than the analytical value for the L-fan, and 0.22% greater for the N-Fan. The numerical fan power is 1.49% less than the analytical value for the L-fan, and 0.73% greater for the N-fan.

The numerical heat transfer deviates significantly from the analytical where it underpredicts the analytical draft equation results. The numerical L-fan and N-fan heat transfer is respectively 9.15% (1.68 MW) and 9.06% (1.55 MW) less than the analytical results. The deviation of the numerical results from the analytical is attributed primarily to non-uniform flow inside the plenum chamber of the fan-unit.

The heat transfer calculated in the analytical draft equation does not account for the non-uniform flow distribution through the heat exchanger. The non-uniform flow distribution is a combined result of both the overlap and offset between the fan outlet and the heat exchanger inlet. Additionally the actuator disk model provides a tangential source term component that leads to swirling flow inside the plenum chamber, causing a further increase in the non-uniformity of the flow through the heat exchanger. Similar overall trends were observed in previous studies, specifically Engelbrecht (2018) who also utilized an actuator disk model and A-frame plenum chamber.

It should be noted that previous studies by Owen (2010), Joubert (2010) and Louw (2011) all utilised simplified ACC fan-units with box-shaped plenum chambers and horizontally orientated heat exchangers. The simplified fan-units used in the abovementioned studies limited the accuracy of the numerically calculated flow fields inside the plenum chambers.

4.4.6 Conclusions

The numerical model of the Single Fan Forced Draft ACC succesfully combined the incompressible flow implementations of the actuator disk model used for the axial flow fan and the Darcy-Forchheimer porosity model and ε-NTU heat transfer model used for the heat exchangers. The numerical results obtained from the Single Fan Forced Draft ACC model are sufficiently close enough to the analytical draft equation results to validate the combined numerical model. The only significant difference was found in the heat transfer rates, which is attributed to the one-dimensional uniform flow approximation made in the analtyical draft equation.

Chapter 5

Forced Draft ACC Analysis

5.1 Forced Draft ACC Model Setup

5.1.1 Computational Domain

The Forced Draft ACC is compromised of an 8×8 array of A-frame forced draft fan-units which are located in an extended atmospheric domain. The computational domain is shown in Figs. 5.1 and 5.2, and the dimensions tabulated in Table 5.1.

The 64 fan-units are identified using an (i, j)-indexing scheme corresponding to the x- and y-coordinates of the fan-units, with the layout schematic shown in Fig. 5.1 The i-index identifies the street that the fan-unit is located in, while the j-index identifies the row that the fan-unit is located in. Fan-units in the same street (i.e. same i-index) share a steam duct, but the fan-units have separated plenum chambers.

Both the L-fan and the N-fan are used in the Forced Draft ACC's fan configuration:

1. The L-fan is located at front ($j = 1$) and back ($j = 8$) sides of the ACC and is configured using using a blade setting angle $\gamma_{tip} = 9.3°$
2. The N-fan is used for the remainder of the fan-units ($2 \leq j \leq 7$) and is configured using using a blade setting angle $\gamma_{tip} = 11.6°$.

5.1.2 Computational Mesh

The computational domain and mesh for the 64-fan Forced Draft ACC Model reuses the modular domain and mesh components created for the Single Fan Forced Draft ACC Model. Only the atmospheric submesh is new due to the

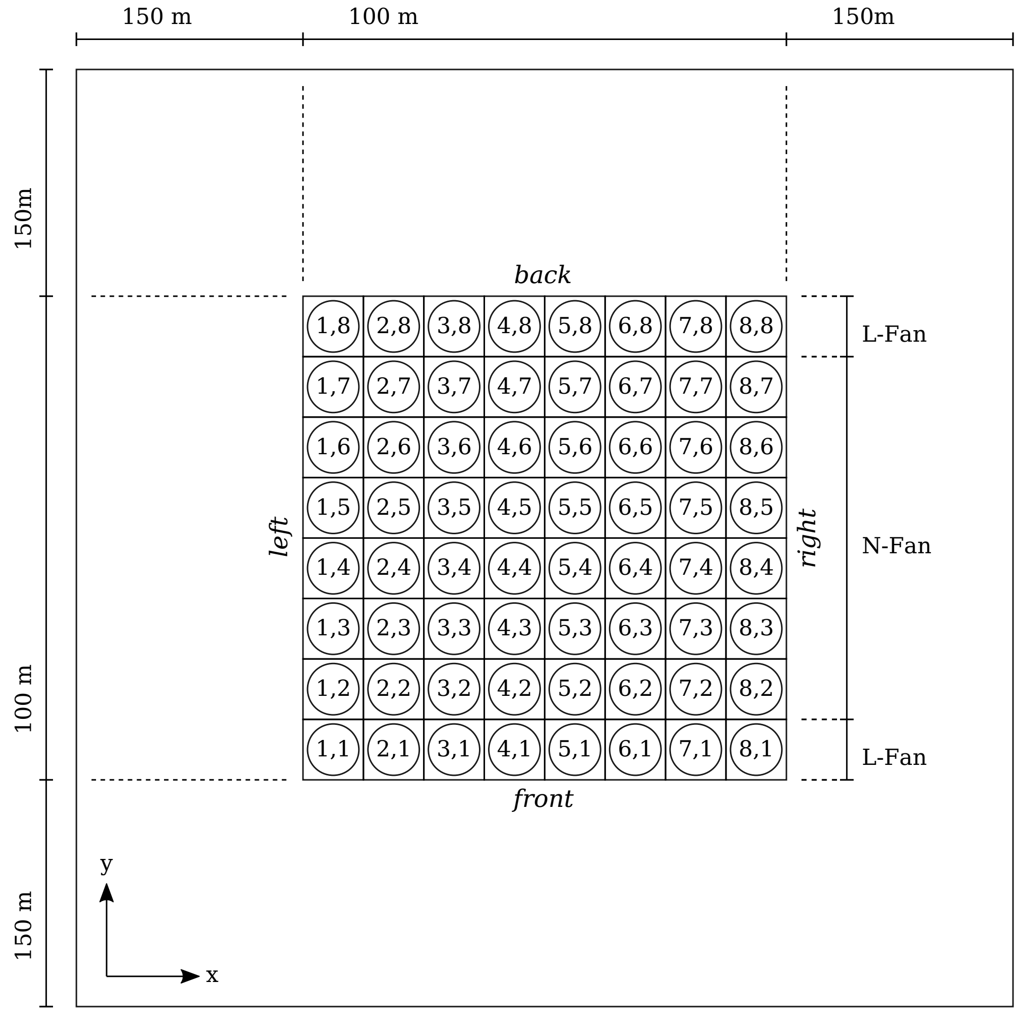

Figure 5.1: Forced Draft ACC Schematic: Top View

.

difference in size between the single fan ACC's atmospheric domain and that of the current 64-fan ACC. The submesh components created to form the entire computational domain were previously listed in Table 4.6.

Similar to the Single Fan Forced Draft ACC Model the atmospheric mesh used is constructed using an initial hexahedral mesh which is then subjected to successive refinements in the vicinity of the ACC subdomain. The mesh refinement is achieved using a cell-splitting technique on the structured hexahedral mesh. The use of multiple layers of refinement allows the relatively coarse atmospheric mesh to be refined such that the cells near the relatively fine ACC subdomain mesh are of similar size. A cross-sectional slice of the atmospheric submesh showing the refinement regions is displayed in Fig. 5.3.

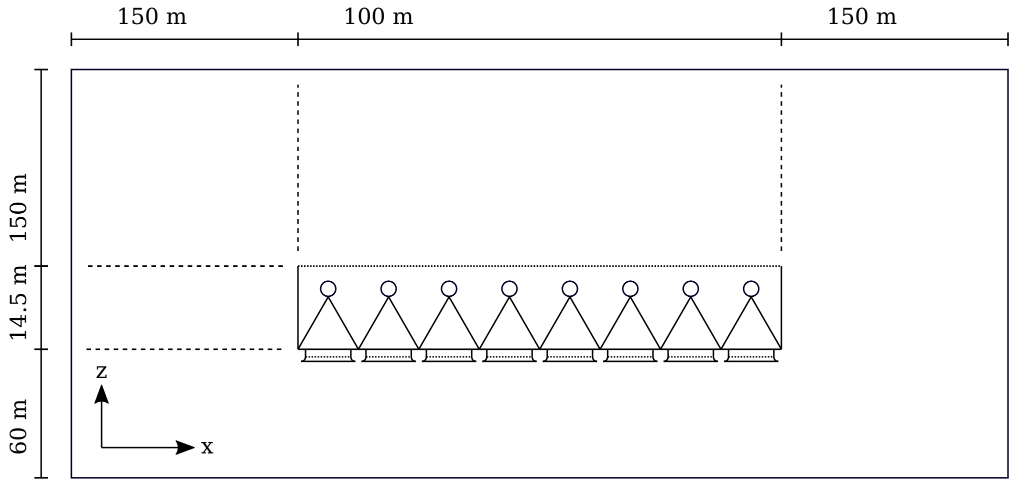

Figure 5.2: Forced Draft ACC Schematic: Front View

Table 5.1: Forced Draft Domain Dimensions

Dimension	Symbol	Value	
Unit Width	L_u	12.5	m
Platform Height	L_p	60.0	m
Distance to Atmospheric Sides	L_a	150.0	m
Distance to Atmospheric Top	L_t	210.0	m

The final mesh for the 64-fan Forced Draft ACC Model consists of a total of 45.97×10^6 cells, of which 20.98×10^6 are hexahedral cells and 24.81×10^6 are tetrahedral cells.

5.1.3 Boundary Conditions

The Forced Draft ACC Model's boundary conditions are set to match atmospheric conditions, similar to the Single Fan Forced Draft ACC Model's boundary conditions. The boundary conditions used are tabulated in Table 5.2.

The same `OpenFOAM` incompressible flow solver used in the Single Fan Forced Draft ACC Model is used for the full Forced Draft ACC Model. The alternative pressure field, p', given previously in Eqn. (4.10) is solved numerically and the actual pressure, p, is obtained when necessary by back substitution.

A total pressure boundary condition is used at the atmospheric boundaries with the reference pressure, p_{ref}, set to 101325 Pa. A zero-gradient boundary condition is used for the pressure field at the walls of the ACC.

The `OpenFOAM` specific `pressureInletOutletVelocity` velocity boundary con-

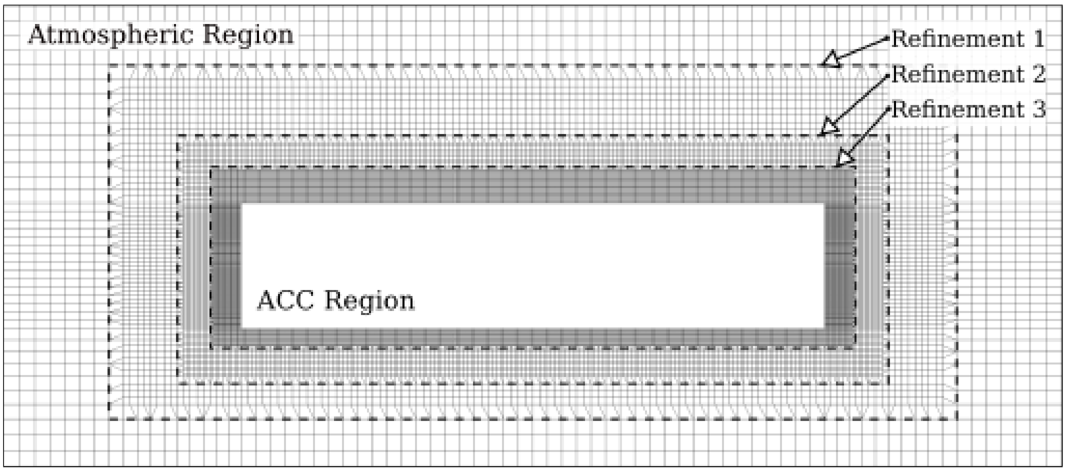

Figure 5.3: Forced Draft Atmospheric Submesh Refinement

Table 5.2: Forced Draft ACC Boundary Conditions

Field	Boundary	Type	Value
p'	Sides/Top	`totalPressure`	p_{ref}
	Walls	`zeroGradient`	$\nabla p'_{\perp} = 0$
U	Inlet	`atmBoundaryLayerInletVelocity`	Eqn. (3.31)
	Sides	`pressureInletOutletVelocity`	$\nabla U_{\perp} = 0$
	Walls	`noSlip`	$U = 0$
T	Sides	`inletOutlet`	T_{ref}, $\nabla T_{\perp} = 0$
	Walls	`zeroGradient`	$\nabla T_{\perp} = 0$

dition is used to for atmospheric boundaries. For inflow conditions the internal flow field is used to determine the inlet flux, while for outflow conditions a zero-gradient boundary condition is used.

The `OpenFOAM` specific `atmBoundaryLayerInletVelocity` is used to apply the crosswind's velocity profile at the appropriate atmospheric inlet boundaries of the domain. The velocity profile is calculated using Eqn. (3.31).

The `OpenFOAM` specific `inletOutlet` boundary condition is used to set the temperature at the atmospheric boundaries of the domain. Under inflow conditions the boundary is specified using a reference temperature, T_{ref}, set to 300 K, while under outflow conditions a zero-gradient boundary condition is used.

Standard wall-functions are used for the *standard* k-ϵ turbulence model.

5.2 Performance Criteria

5.2.1 Volumetric Effectiveness

The volumetric effectiveness, $\varepsilon_{\dot{V}}$, is defined as the normalised volumetric flow rate through the fan-unit:

$$\varepsilon_{\dot{V}} = \frac{\dot{V}}{\dot{V}_{ideal}} \tag{5.1}$$

where $\dot{V}_{ideal}$ is the ideal volumetric flow rate which is approximated using the results from a Single Fan ACC.

Normalising the volumetric flow rate through the ACC using an idealised flow rate is useful in determining which fan-units underperform when the ACC is subjected to adverse operating conditions. The method is particularly useful when different fan configurations are present in the ACC, as demonstrated by Engelbrecht (2018).

5.2.2 Heat Transfer Effectiveness

Similar to the volumetric effectiveness, the heat transfer effectiveness, $\varepsilon_{\dot{Q}}$, is defined as the normalised heat transfer rate:

$$\varepsilon_{\dot{Q}} = \frac{\dot{Q}}{\dot{Q}_{ideal}} \tag{5.2}$$

where $\dot{Q}_{ideal}$ is the ideal heat transfer rate which is approximated using the results from a Single Fan ACC.

5.2.3 Heat-to-Power Ratio

The heat-to-power ratio, η_{HTP}, is defined as the ratio between the heat exchanger's heat transfer rate and the fan power consumption (Engelbrecht, 2018):

$$\eta_{HTP} = \frac{\dot{Q}}{\dot{W}} \tag{5.3}$$

The heat-to-power ratio combines the fan and heat exchanger performance into a singular metric that is particularly useful when different fan and heat exchangers configurations are present in an ACC.

5.2.4 Simulations

The Forced Draft ACC Model was solved for a total of seven different crosswind conditions. The first solution serves as the reference case for normal operation of the Forced Draft ACC with no crosswind applied, i.e. $U_{ref} = 0$ m/s. The numerical model was then solved for three different crosswind magnitudes in both the primary and secondary crosswind directions. The three reference crosswinds magnitudes (U_{ref}) used were 3 m/s, 6 m/s and 9 m/s.

The primary crosswind direction is defined as aligned with the steam ducts, and thus parallel to the heat exchanger bundles, which puts the L-fan configured front row fan-units ($j = 1$) at the leading edge of the ACC. The secondary crosswind direction is defined as perpendicular to the steam ducts and the heat exchanger bundles, which puts the N-fan configured left column fan-units ($i = 1$) at the leading edge of the ACC.

Parallel computing capability is required to solve the flow fields due to the size of the 64-fan model. The High Performance Cluster (HPC) at the University of Stellenbosch was initially used, however the size of the simulations exceeded the HPC's capacity. The simulations were moved to the Centre for High Performance Computing (CHPC) in Cape Town. The model required the use of seven 24-core `Intel Xeon`®(2.6 GHz) compute nodes on the CHPC, with a total runtime of five days per simulation.

5.3 Forced Draft ACC Performance Analysis

5.3.1 Normal Operating Conditions

The results obtained for the Forced Draft ACC under normal operating conditions are presented in this section. Normal operating conditions are defined by the lack of crosswinds, i.e. the reference crosswind velocity is zero: $U_{ref} = 0$ m/s.

Fan Performance

The fan volumetric flow rate and fan power consumption of the Forced Draft ACC under normal operating conditions are shown in Fig. 5.4.

The front ($j = 1$) and back ($j = 8$) fan-units show volumetric flow rates that are on average 13.3 m^3/s greater than that of the neighbouring inner fan-units, while the fan power is on average 25.1 kW greater. This is consistent with the difference in performance between the L-fan and N-fan observed in for a Single Fan Forced Draft ACC (see § 4.4).

The left ($i = 1$) and right ($i = 8$) fan-units show volumetric flow rates that are on average 26.7 m^3/s less when compared to that of the neighbouring inner fan-units. The difference is attributed to flow separation at the above-mentioned sides of the ACC. The steeper fan pressure characteristic curve of the L-fan,

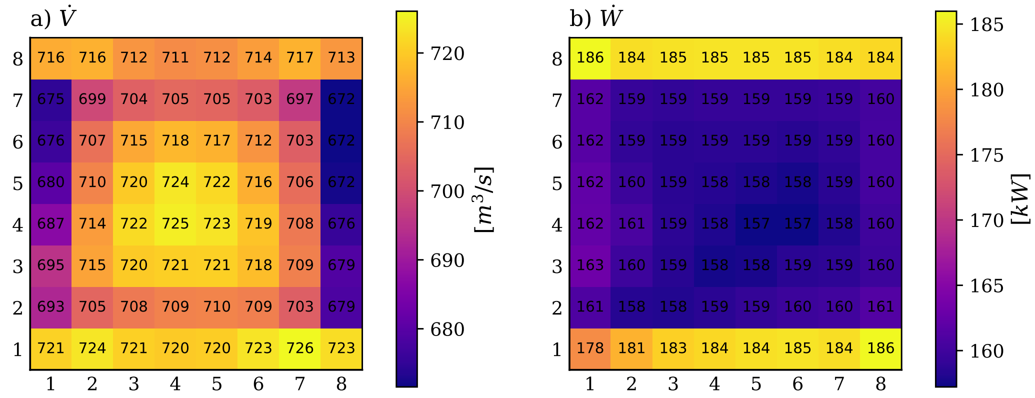

Figure 5.4: Forced Draft Fan Performance ($U_{ref} = 0$ m/s)

compared to the N-fan, allows the fan-units located at the front and back sides of the ACC to mitigate the effect of flow separation.

Flow Separation

Flow separation at the sides of the Forced Draft ACC under normal operating conditions is shown in Fig. 5.5. The flow separation is shown using velocity magnitude plots on the yz-plane through the centres of fan-units $(1, 4)$ and $(4, 1)$

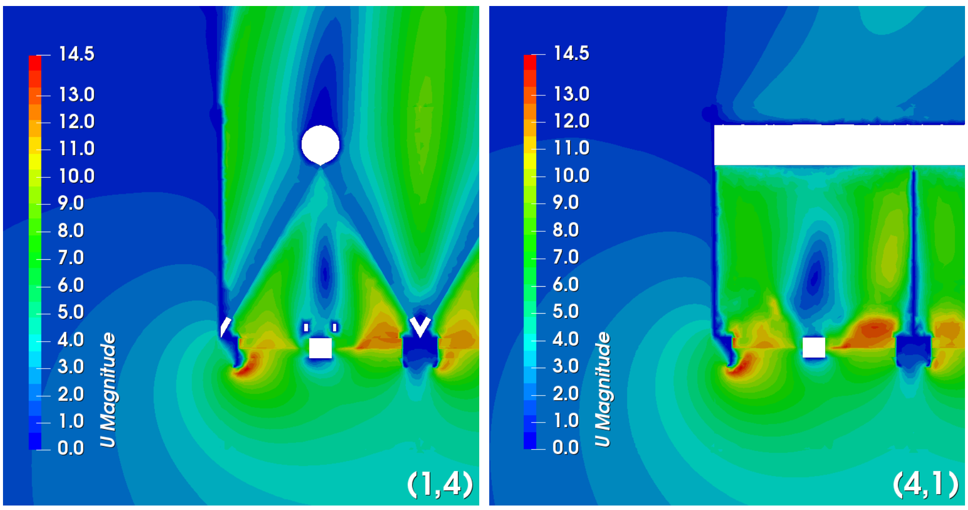

Figure 5.5: Forced Draft Flow Separation ($U_{ref} = 0$ m/s)

The results show some flow separation at the leading edge of the bellmouths of the fan-units at the perimeter of the ACC. The flow separation shown is purely due to the cross drafts induced by the inner fan-units.

Heat Exchanger Performance

The total heat transfer rate and mean heat exchanger inlet air temperatures per fan-unit for the Forced Draft ACC under normal conditions are shown in Fig. 5.6. The inlet temperatures shown are distributed relatively uniformly over the ACC's fan-units.

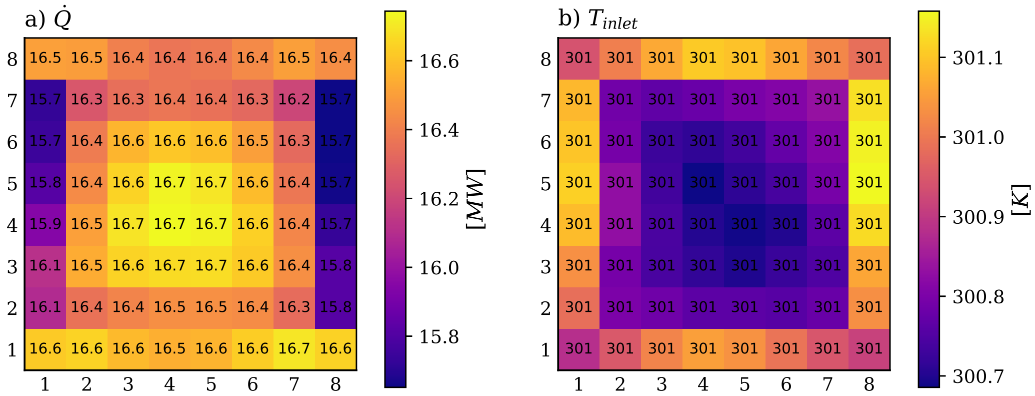

Figure 5.6: Forced Draft Heat Exchanger Performance ($U_{ref} = 0$ m/s)

The heat transfer rate correlates well with the fan volumetric flow rates, as shown in Fig. 5.6. This suggests that the volumetric flow rate through each fan-unit is the driving force behind the heat transfer rate, which is in agreement both with theory (Eqn. (3.25)) and previous numerical results (Engelbrecht, 2018).

Larger heat transfer rates are present at the centre located fan-units, while lower heat transfer is present at the left ($i = 1$) and right ($i = 8$) sides of the ACC. At the centre the mean heat transfer rate is approximately 0.15 MW greater that that of its neighbouring fan-units. At the left and right sides of the ACC the mean heat transfer rate per fan-unit is approximately 0.57 MW less than that of the neighbouring inner fan-units.

No significant difference in heat transfer rate is present at the front and back of the ACC. This is due to the L-fan's ability to mitigate the effect of the induced cross drafts on the volumetric flow rates through the units.

System Performance

The volumetric and heat transfer effectiveness of the Forced Draft ACC under normal operating conditions is shown in Fig. 5.7. The results show an almost direct mapping of volumetric effectiveness to heat transfer effectiveness.

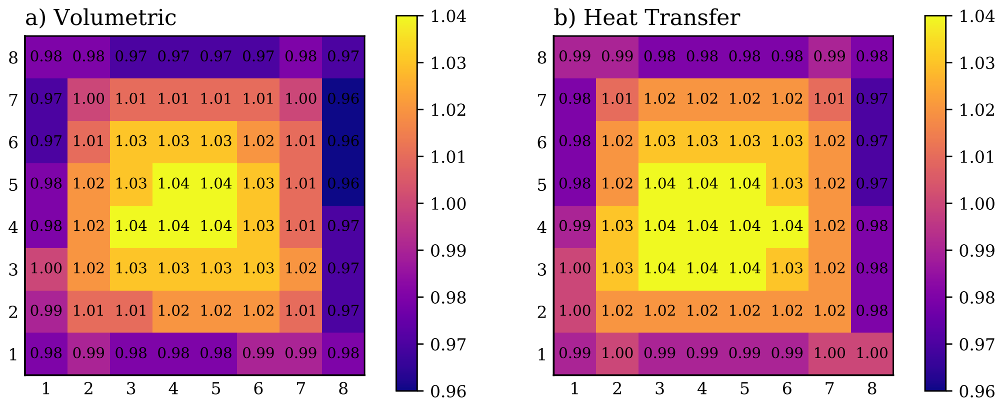

Figure 5.7: Forced Draft System Effectiveness ($U_{ref} = 0$ m/s)

The volumetric effectiveness of the L-fan fan-units located at the front ($j = 1$) and back ($j = 8$) sides of the ACC are near identical to that of the N-fan fan-units at the left ($i = 1$) and right ($i = 8$) sides of the ACC. This suggests that the relative performance decrease due to induced cross drafts is independent of the fan used in each fan-unit. A similar observation can be made from the results presented by Engelbrecht (2018).

The volumetric and heat transfer effectiveness of the inner fan-units are greater than 1, i.e. the effective performance of those fan-units exceeds that of a single isolated ACC fan-unit. Similar observations were made by Owen (2010), Louw (2011) and Engelbrecht (2018).

The fan-unit heat-to-power ratios of the Forced Draft ACC under normal operating conditions are shown in Fig. 5.8.

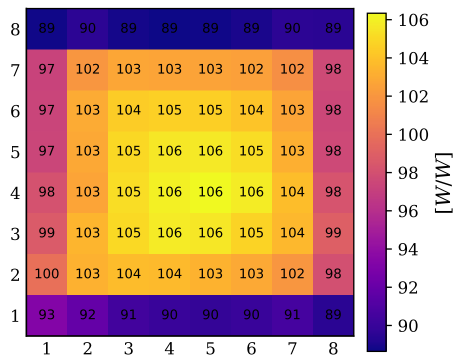

Figure 5.8: Forced Draft Heat-to-Power Ratio ($U_{ref} = 0$ m/s)

The heat-to-power results show similarities with the heat transfer results shown in Fig. 5.6. However, the results deviate at the front and back sides of the ACC where the high power requirement of the L-fan, as shown in Fig. 5.4, reduces the mean heat-to-power ratio of those units to an average of 90.1 W/W, while at the left and right hand sides where the N-fan is used the mean heat-to-power ratio only decreases to an average of 98.1 W/W. The clear difference in heat-to-power ratios between the two fans suggests that under normal operating conditions the use of the N-fan is preferred for its higher heat-to-power ratio.

5.3.2 Primary Crosswind Conditions

The results obtained for the Forced Draft ACC under primary crosswind conditions are presented in this section. The primary crosswind direction is in the y-direction, i.e. aligned with the steam ducts, and thus parallel to the heat exchanger bundles. The primary crosswinds put the L-fan configured front row fan-units ($j = 1$) at the leading edge of the ACC.

System Performance

The volumetric effectiveness and heat transfer effectiveness results of the Forced Draft ACC under primary crosswind condition of 3, 6 and 9 m/s are shown in Figs. 5.9 to 5.11. The volumetric effectiveness decreases as the crosswind velocity increases, and the decrease in heat transfer effectiveness that follows, is comparable to that observed by Louw (2011) and Engelbrecht (2018).

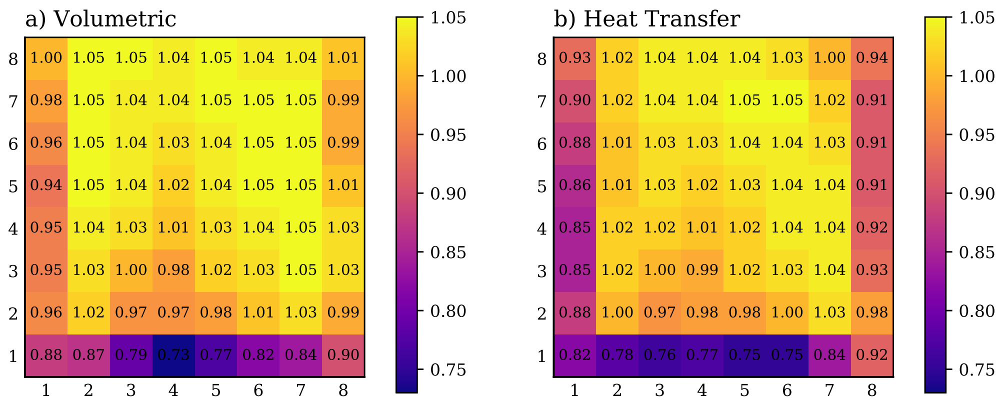

Figure 5.9: Forced Draft System Effectiveness ($U_y = 3$ m/s)

Similar to the Forced Draft ACC under normal operating conditions, the heat transfer effectiveness shows an almost direct one-to-one mapping to the volumetric effectiveness. This breaks down at the leading edge fan-units ($j = 1$) as well as at the left ($i = 1$) and right ($i = 8$) side fan-units downwind of the leading edge.

The mean volumetric effectiveness of the leading edge fan-units, excluding the corner units, decreases from 0.99 under normal operating conditions to 0.80, 0.16 and 0.02 under crosswinds of 3, 6 and 9 m/s respectively. The

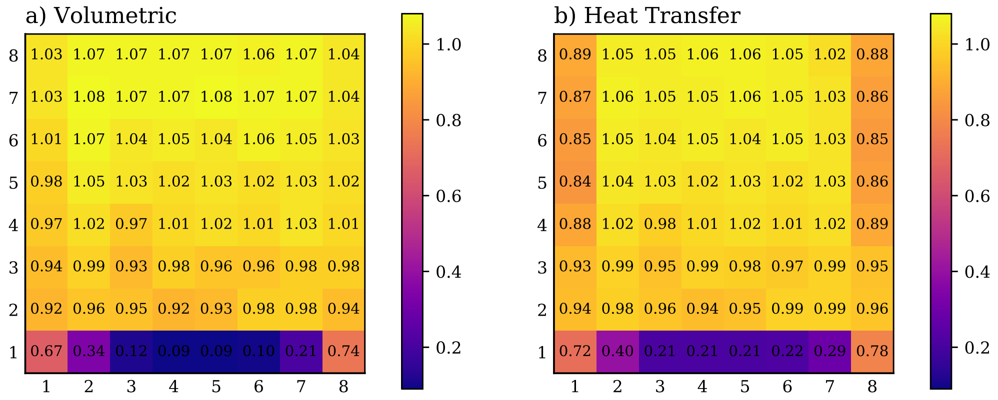

Figure 5.10: Forced Draft System Effectiveness ($U_y = 6$ m/s)

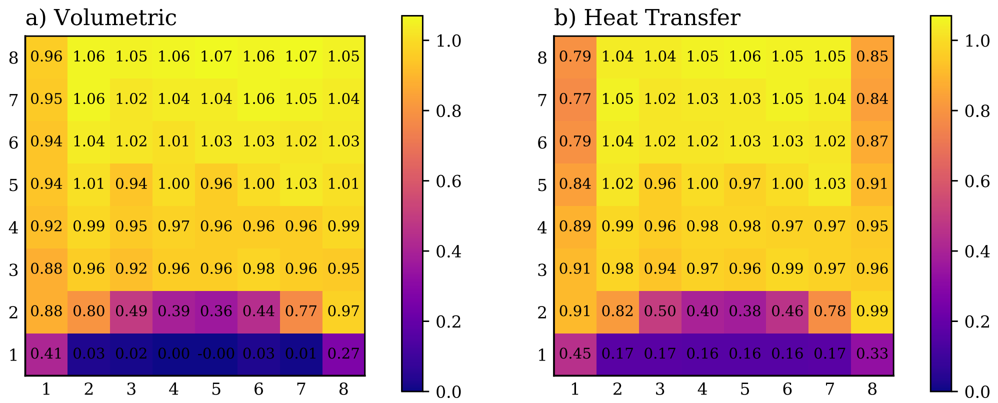

Figure 5.11: Forced Draft System Effectiveness ($U_y = 9$ m/s)

mean heat transfer effectiveness of the above-mentioned fan-units decreases less, from 0.99 under normal operating conditions to 0.78, 0.26 and 0.17 under the same crosswind velocities. The difference in volumetric and heat transfer effectiveness is attributed to some reverse flow occuring through the leading edge fan-units' heat exchangers. The reverse flow negatively affects the net volumetric flow rate, reducing the mean to nearly 0 at 9 m/s crosswinds, but it does still facilitate some heat transfer which is why the heat transfer effectiveness is greater than the volumetric effectiveness.

The fan-units directly downwind of the leading edge, $j = 2$, also exhibit decreases in volumetric and heat transfer effectiveness. The mean volumetric effectiveness of the above-mentioned fan-units decreases from the norm of 1.02 to 1.00, 0.95 and 0.54 under crosswinds of 3, 6 and 9 m/s respectively. Similar effectiveness values are seen for the heat transfer effectiveness.

The mean heat transfer effectiveness of the downwind fan-units ($j \geq 2$) at the left and right sides of the ACC is marginally less than the volumetric effectiveness under all three crosswinds velocities. This suggests that under crosswind conditions an additional factor affecting the heat transfer at the sides of the ACC exists, i.e. increased inlet temperatures due to hot plume recirculation.

The mean volumetric and heat transfer effectiveness of the fan-units far downwind of the leading edge ($j \geq 6$) is greater than 1 for all crosswind velocities. This indicates that the downwind fan-units are exploiting the energy in the wind to supplement their own performance. Similar effectiveness trends were observed in previous full sized ACC studies (van Rooyen, 2007; Joubert, 2010; Owen, 2010; Louw, 2011).

The fan-unit heat-to-power ratios of the Forced Draft ACC under primary crosswinds of 3, 6 and 9 m/s are shown in Figs. 5.12 to 5.14. Low heat-to-power ratios are found at the leading edge fan-units as well as left and right sides of the ACC. This is consistent with the reduced volumetric and heat transfer effectiveness found at these locations.

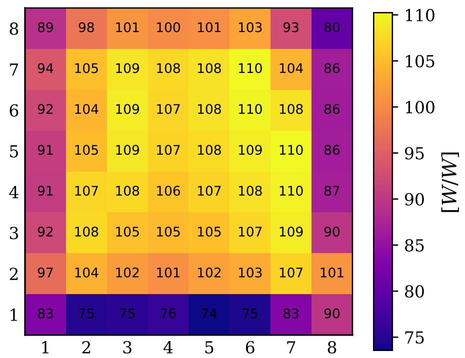

Figure 5.12: Forced Draft Heat-to-Power Ratio ($U_y = 3$ m/s)

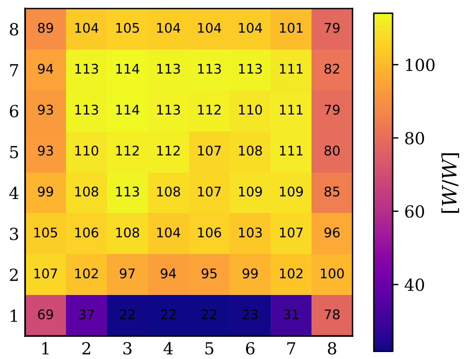

Figure 5.13: Forced Draft Heat-to-Power Ratio ($U_y = 6$ m/s)

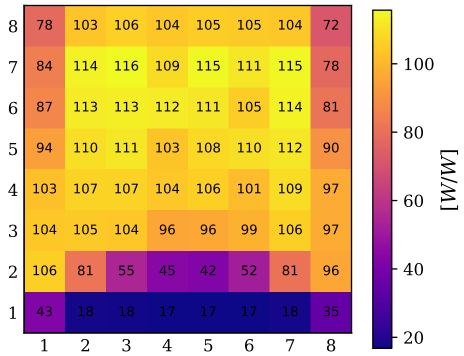

Figure 5.14: Forced Draft Heat-to-Power Ratio ($U_y = 9$ m/s)

The overall mean heat-to-power ratio of the ACC decreases from 99.4 W/W under normal operating conditions to 98.9 W/W under 3 m/s crosswinds, to 95.2 W/W under 6 m/s crosswinds, and to 88.7 W/W under 9 m/s crosswinds. The mean heat-to-power ratio of the leading edge fan-units, excluding the corner units, decreases from 90.7 W/W to 76.3, 26.2 and 17.5 W/W at crosswinds of 3, 6 and 9 m/s.

The heat-to-power ratios of the left and right sides fan-units of the ACC decreases from a mean of 96.1 W/W under normal operating to a mean of 89.7, 89.2 and 84.1 W/W under crosswinds of 3, 6 and 9 m/s respectively. Under the above-mentioned crosswinds the heat-to-power ratios of the left side fan-units are on average 2.9, 8.8 and 6.6 W/W greater than that of the right side fan-units. The asymmetry is attributed to the crosswinds affecting the inflow angle to the rotating fans differently, depending on which side of the ACC the fans are located and thereby affecting their effectiveness.

The leading edge corner fan-units, $(1, 1)$ and $(8, 1)$, are excluded in the preceding analysis of the leading edge and side fan-units' performance. The corner fan-units are capable of drawing in airflow laterally and therefore do not accurately represent the reduction in performance due to flow separation at the leading edge. Nor do the corner fan-units accurately represent the hot plume recirculation that affects the sides of the ACC. Both the above-mentioned phenomena will be investigated in the sections to follow.

Flow Separation

Flow separation at the leading edge ($j = 1$) of the Forced Draft ACC under primary crosswind conditions is shown in Figs. 5.15 to 5.17 for crosswinds of 3, 6 and 9 m/s. The flow separation is shown using velocity plots on the yz-plane through the centres of fan-units $(1, 1)$ and $(4, 1)$.

The figures show that the flow separation increases as the crosswind velocity

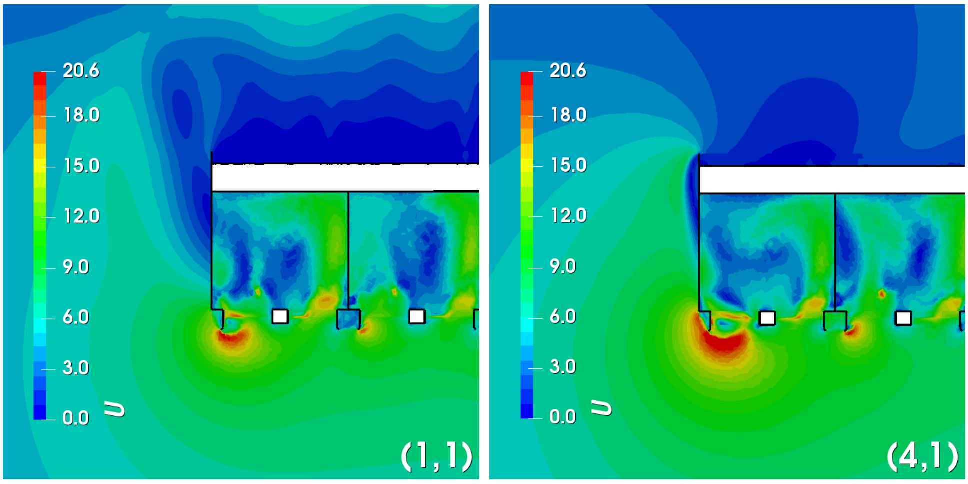

Figure 5.15: Forced Draft Flow Separation at Leading Edge ($U_y = 3$ m/s)

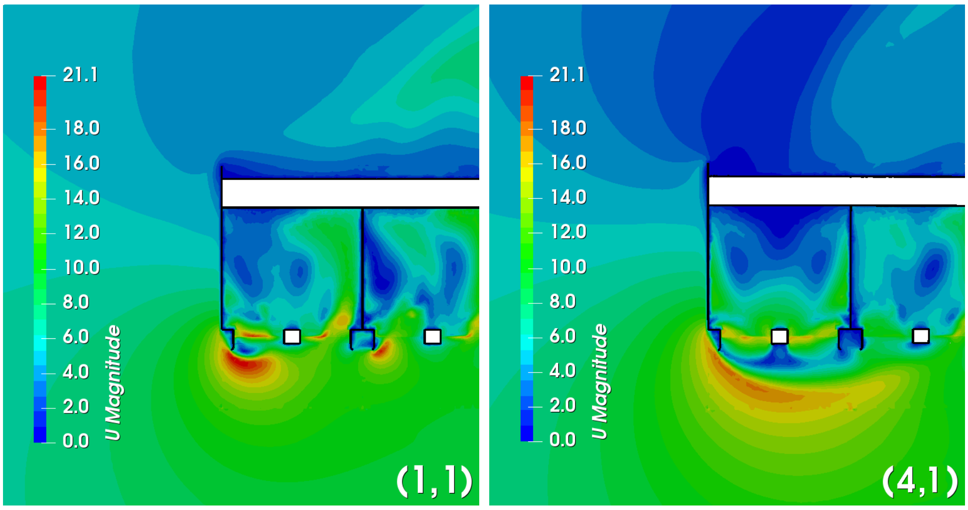

Figure 5.16: Forced Draft Flow Separation at Leading Edge ($U_y = 6$ m/s)

increases. Greater flow separation occurs at the centre fan-unit $(4, 1)$ where the flow into the fan-units is primarily two-dimensional flow, while the corner fan-unit $(1, 1)$ is able to draw in air laterally and thereby mitigate some of the effects of flow separation. The above-mentioned trends are consistent with the volumetric effectiveness of the leading edge fan-units as shown in Figs. 5.9 to 5.11.

A low velocity region is shown to develop, connecting the bellmouth and hub of the centre fan-unit $(4, 1)$ for the 6 m/s and 9 m/s crosswind cases. This is indicative of the flow separation restricting airflow to the fan, thereby limiting fan performance.

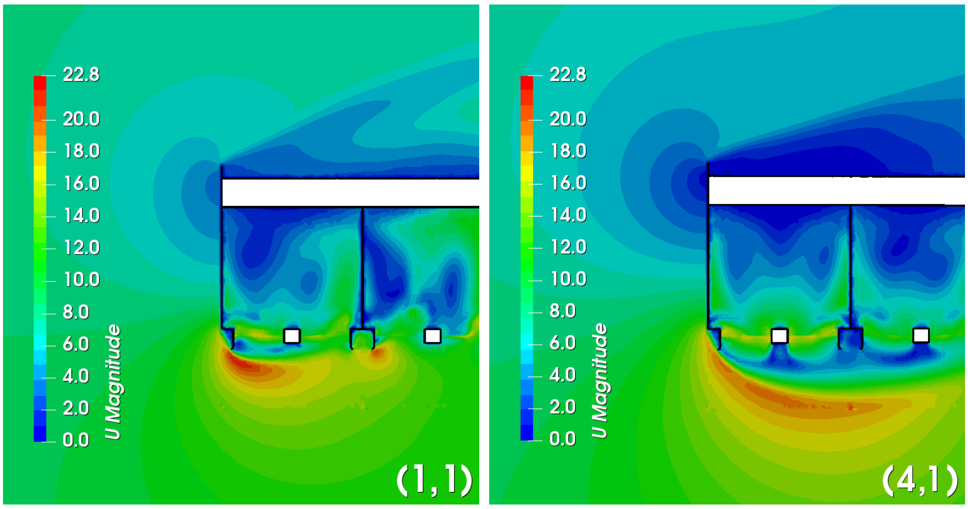

Figure 5.17: Forced Draft Flow Separation at Leading Edge ($U_y = 9$ m/s)

Heat Exchanger Performance

The total heat transfer rate per fan-unit and mean heat exchanger inlet air temperatures of the Forced Draft ACC under primary crosswinds of 3, 6 and 9 m/s are shown in Figs. 5.18 to 5.20.

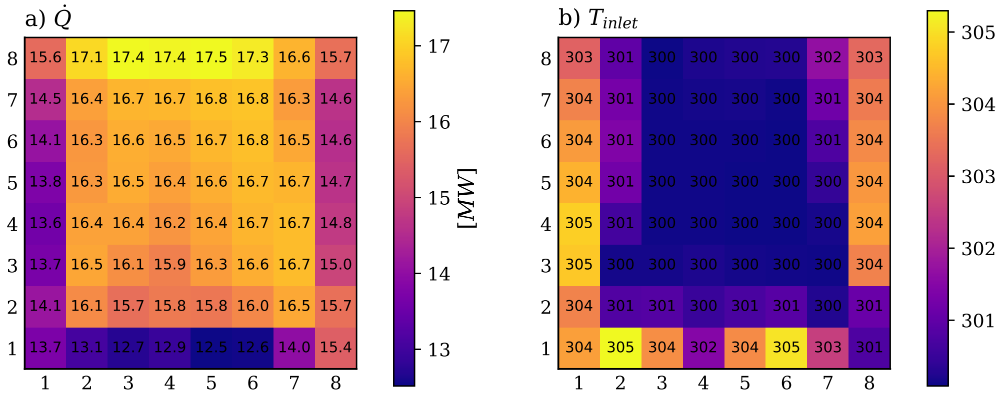

Figure 5.18: Forced Draft Heat Exchanger Performance ($U_y = 3$ m/s)

The heat transfer results shown are consistent with the system effectiveness results shown in Figs. 5.9 to 5.11. Increases in the heat exchanger inlet air temperatures account for the difference in volumetric and heat transfer effectiveness at the leading edge ($j = 1$) and the left ($i = 1$) and right ($i = 8$) sides of the ACC.

The decrease in heat transfer is most prevalent at the leading edge fan-units, and to a lesser extent at the fan-units directly downwind of leading edge. The

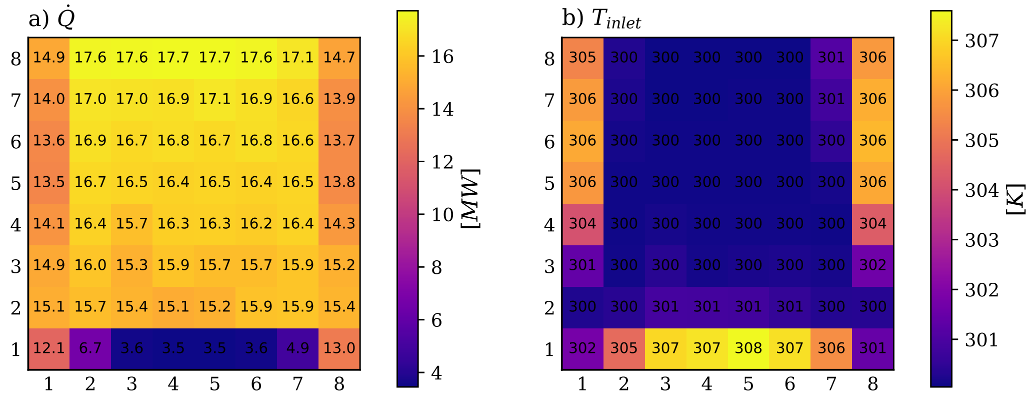

Figure 5.19: Forced Draft Heat Exchanger Performance ($U_y = 6$ m/s)

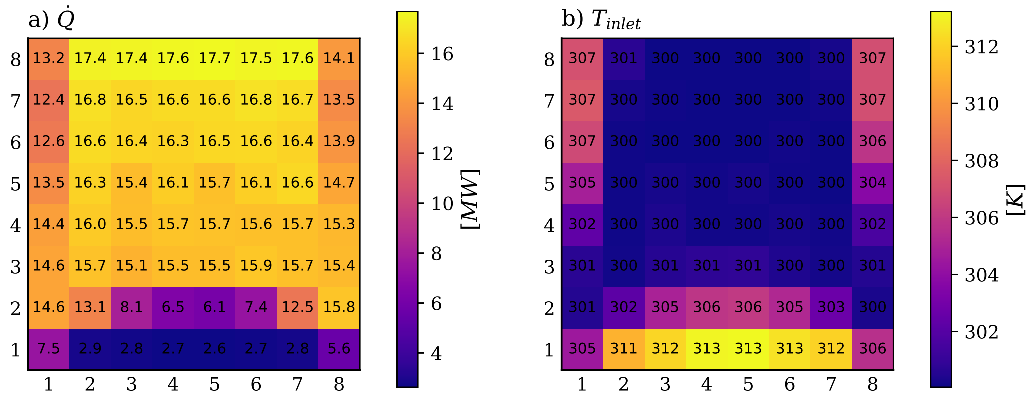

Figure 5.20: Forced Draft Heat Exchanger Performance ($U_y = 9$ m/s)

heat transfer rate decreases as the crosswind velocity increases due to the decrease in volumetric flow rate. The mean heat transfer at the leading edge fan-units decreases from the norm of 16 MW by 3.63, 12.3 and 13.9 MW under crosswinds of 3, 6 and 9 m/s respectively. The decrease in heat transfer at the leading edge is primarily attributed to lower volumetric flow rates through the fan-units.

Increases in heat exchanger inlet air temperatures is identified as a secondary factor contributing to the decrease in heat transfer at the leading edge fan-units. The mean inlet air temperature increases from 301 K under normal operating conditions to 303.8, 305.9 and 306.3 K under crosswinds of 3, 6 and 9 m/s resepectively. The increase in inlet temperatures is attributed to reverse flow through the fan-units.

Reverse flow at the leading edge fan-units is also responsible for increasing the inlet temperatures of the units directly downwind of the leading edge ($i = 2$). This phenomena occurs at high crosswind velocities, i.e. 9 m/s, when the volumetric flow rates through the centre most fan-units of the leading edge ($3 \leq i \leq 6$) is near zero. As a result some heated air escapes into the supply airflow of the downwind fan-units thereby increasing the mean inlet air temperatures by 4.5 K. This contributes to the low heat transfer of 7 MW at these fan-units. Similar observations were made for leading edge fan-units at high crosswind velocities by Louw (2011) and Engelbrecht (2018).

The decrease in heat transfer effectiveness at the left and right sides of the ACC is attributed to hot plume recirculation, i.e. heated air from upwind heat exchangers recirculating through the downwind fan-units. The effect can be seen for all crosswind velocities where it affects the fan-units further downstream of the leading edge ($j \geq 3$). The mean heat exchanger inlet air temperatures of the above-mentioned fan units increase to 303.8, 305.9 and 306.3 K at crosswinds of 3, 6 and 9 m/s respectively. The increase in inlet temperatures of the side fan-units is consistent with the results obtained by Engelbrecht (2018) where increases of similar magnitudes, approximately 5 K, were observed for the downstream fan-units.

The heat transfer is asymmetrical with the left side fan-units ($i = 1$) exhibiting a mean heat transfer rate that is 0.7 MW less on average than their right side fan-units ($i = 8$). This difference is not reflected in the inlet temperatures of the above-mentioned fan-units, indicating that the decrease is due to the asymmetric volumetric flow rates caused by fan rotation at the sides of the ACC.

Hot Plume Recirculation

Hot plume recirculation for the 9 m/s primary crosswind is shown in Figs. 5.21 and 5.22. The velocity and temperature fields are shown on the xz-plane through the centres of three different fan-units: $(1, 4)$, $(1, 6)$ and $(1, 8)$.

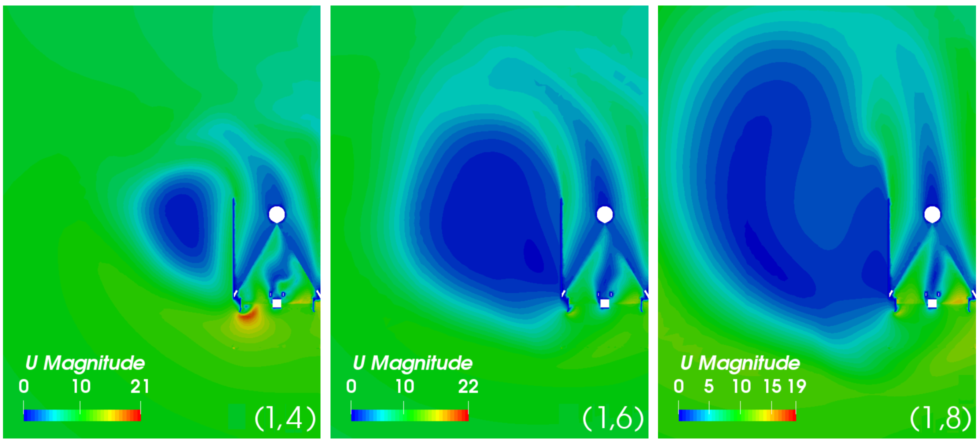

Figure 5.21: Forced Draft Recirculation Velocities ($U_y = 9$ m/s)

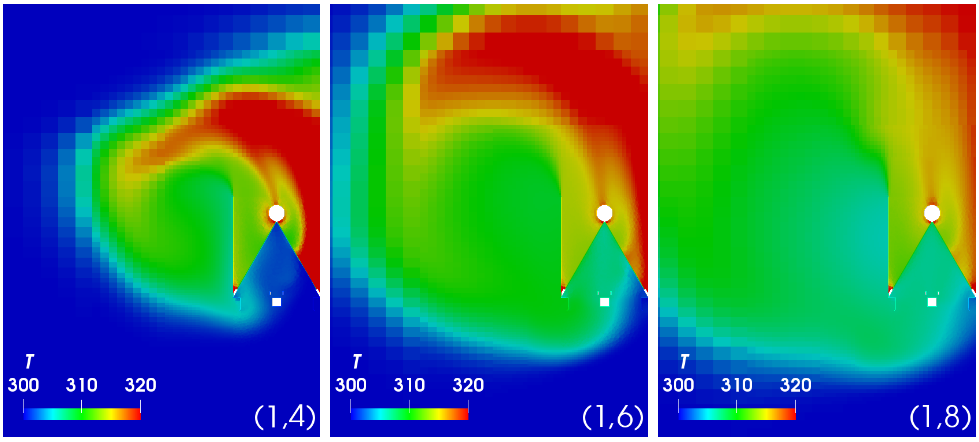

Figure 5.22: Forced Draft Recirculation Temperatures ($U_y = 9$ m/s)

The recirculation vortices are observed to grow larger as they move downwind of the leading edge. This is consistent with observations made by Louw (2011) and Engelbrecht (2018)

The flow field streamlines for the 9 m/s primary crosswind are shown in Fig. 5.23. The streamlines show the vortex that forms at the side of the ACC, starting from the corner fan-unit at the leading edge. The vortex formed is only large enough to recirculate hot air starting at the third downwind fan-unit. The orientation of the A-frames in the ACC, i.e. parallel to the crosswind direction, allows the recirculation to occur relatively smoothly over the windwall of the ACC.

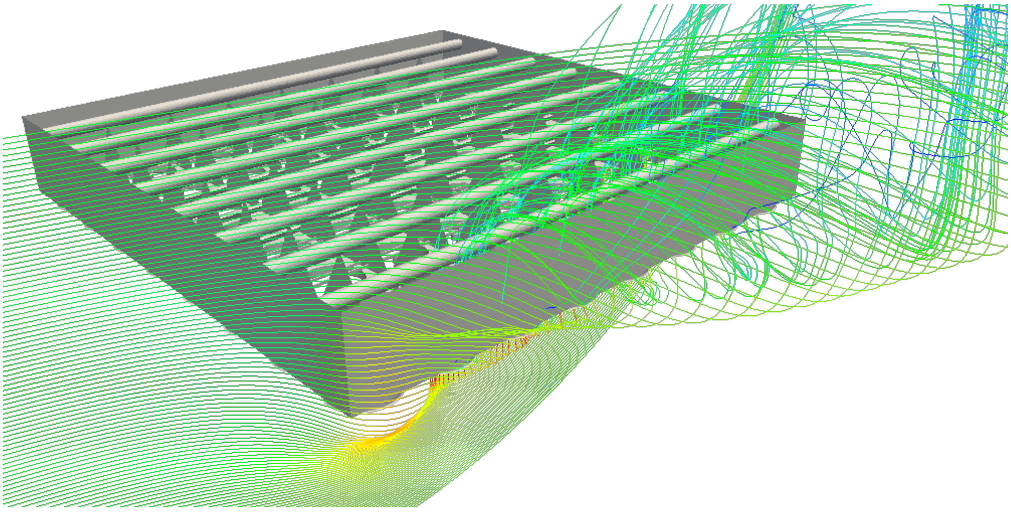

Figure 5.23: Forced Draft Recirculation Streamlines: $U_y = 9$ m/s

5.3.3 Secondary Crosswind Conditions

The results obtained for the Forced Draft ACC under secondary crosswinds conditions are presented in this section. The secondary crosswind direction is in the x-direction, i.e. perpendicular to the steam ducts and the heat exchanger bundles. The secondary crosswinds put the N-fan configured left column fan-units ($i = 1$) at the leading edge of the ACC.

System Performance

The volumetric effectiveness and heat transfer effectiveness results of the Forced Draft ACC under secondary crosswinds of 3, 6 and 9 m/s are shown in Figs. 5.24 to 5.26. The ACC shows similar performance trends under secondary crosswind conditions to those that were observed under primary crosswind conditions.

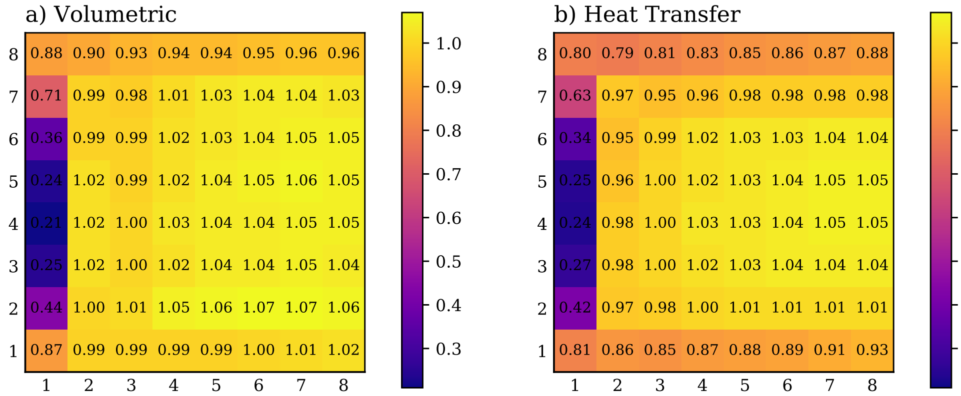

Figure 5.24: Forced Draft System Effectiveness ($U_x = 3$ m/s)

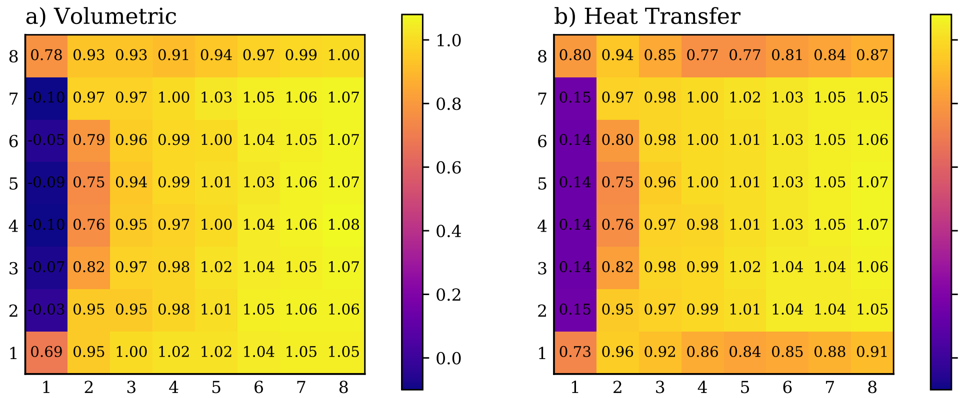

Figure 5.25: Forced Draft System Effectiveness ($U_x = 6$ m/s)

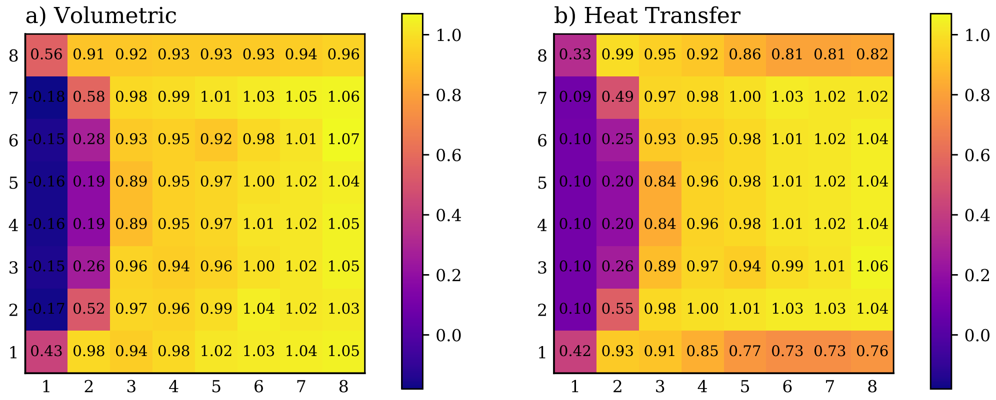

Figure 5.26: Forced Draft System Effectiveness ($U_x = 9$ m/s)

The mean volumetric effectiveness of the leading edge fan-units ($i = 1$) decreases from 0.98 under normal operating conditions to 0.37, -0.07 and -0.16 under crosswinds of 3, 6 and 9 m/s. The mean heat transfer effectiveness of the leading edge fan-units decreases from 0.99 under normal operating conditions to 0.36, 0.14 and 0.10. Under secondary crosswinds of 3, 6 and 9 m/s the decrease in volumetric effectiveness is respectively 3.4, 1.28 and 1.18 times greater than it is under primary crosswinds of similar magnitudes. Similar trends are present for the heat transfer effectiveness. The negative volumetric effectiveness values are indicative of reverse flow through the fan-units.

The difference in effectiveness is attributed to the different fans used at the leading edge of the ACC – the L-fan for primary crosswinds and the N-fan for secondary crosswinds. The L-fan with its steeper pressure characteristic curve mitigates the adverse effect of flow separation at the leading edge better than the N-fan does. Engelbrecht (2018) noted similar differences regarding comparable fans located at the periphery of the ACC.

Similar to primary crosswind condition, the front ($j = 1$) and back ($j = 8$) sides of the ACC show different volumetric and heat transfer effectiveness results. The volumetric and heat transfer effectiveness of the front fan-units are on average 0.064 and 0.055 greater than that of the back fan-units.

The fan-units immediately downwind of the leading edge ($i = 2$) also show decreases in volumetric and heat transfer effectiveness. The mean volumetric effectiveness of the above-mentioned fan-units decreases from 1.01 under normal operating conditions to 1.01, 0.84 and 0.34 at crosswinds of 3, 6 and 9 m/s. Similar effectiveness values are seen for the heat transfer, as was the case for primary crosswind conditions. At higher crosswind velocities, 6 and 9 m/s the mean effectiveness of the fan-units immediately downwind of the leading edge is respectively 0.11 and 0.20 less under secondary crosswinds than under primary crosswinds.

Similar to primary crosswind conditions, fan-units far downwind of the leading edge ($j \geq 6$) show volumetric and heat transfer effectiveness values greater than one for all secondary crosswind velocities. This is again attributed to the downwind fan-units exploiting the energy in the wind to supplement their own performance.

The fan-unit heat-to-power ratios of the Forced Draft ACC under secondary crosswinds of 3, 6 and 9 m/s are shown in Figs. 5.27 to 5.29. Similar trends are shown to those present under primary crosswinds, with low heat-to-power ratios at the leading edge and sides of the ACC.

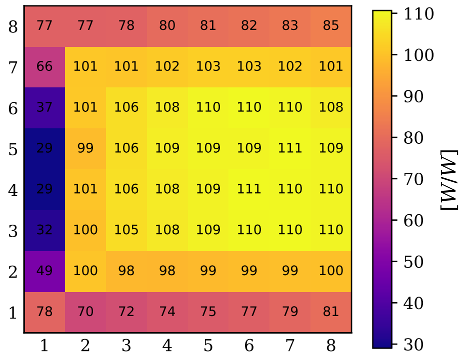

Figure 5.27: Forced Draft Heat-to-Power Ratio ($U_x = 3$ m/s)

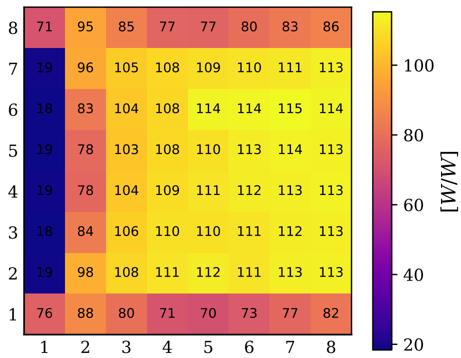

Figure 5.28: Forced Draft Heat-to-Power Ratio ($U_x = 6$ m/s)

The overall mean heat-to-power ratio of the ACC decreases from 99.4 W/W under normal operating conditions to 92.3 W/W under 3 m/s crosswinds, to 91.8 W/W under 6 m/s crosswinds, and to 84.1 W/W under 9 m/s crosswinds. The mean heat-to-power ratios of the leading edge fan-units decreases from 98.2 W/W under normal operating conditions to 40.3, 18.7 and 13.3 W/W at crosswinds of 3, 6 and 9 m/s. The decrease is on average 36.0, 7.5 and 4.2 W/W greater than it is under primary crosswind of similar crosswind magnitudes.

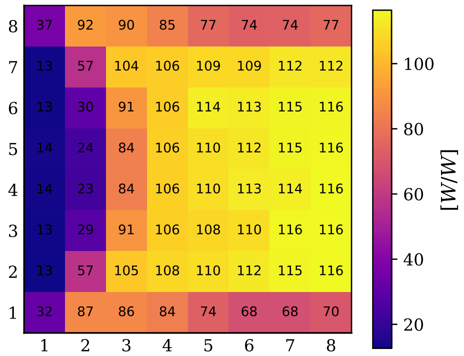

Figure 5.29: Forced Draft Heat-to-Power Ratio ($U_x = 9$ m/s)

The difference between primary and secondary heat-to-power ratios is attributed to the L-fan used at the leading edge of the ACC under primary crosswind conditions. While the L-fan's power consumption is higher than that of the N-fan, as shown in Fig. 5.4, it is capable of keeping a favorable heat-to-power ratio as the crosswind velocity increases. This is again attributed to the L-fan's steeper pressure characteristic ensuring a higher volumetric flow rate through the fan-unit.

The mean heat-to-power ratios of the fan-units at the front and back sides of the ACC decreases from 96.1 W/W under normal operating conditions, to a mean of 75.1, 69.1 and 61.8 W/W under crosswinds of 3, 6 and 9 m/s respectively. The decrease at the sides is attributed to hot plume recirculation increasing the heat exchanger inlet temperatures. The decreases in the heat-to-power ratio of the front and back fan-units is larger under secondary crosswinds than the decreases seen under primary crosswinds. The difference is attributed to the lower heat-to-power ratios of the L-fan used at the front and back fan-units, as shown for normal operating conditions in Fig. 5.8, which means that the increase in inlet temperature has a greater effect on the unit.

Flow Separation

Flow separation at the leading edge ($i = 1$) of the Forced Draft ACC under secondary crosswinds of 3, 6 and 9 m/s is shown in Figs. 5.30 to 5.32. The flow separation is shown using velocity magnitude plots on the xz-plane through the centres of fan-units $(1, 1)$ and $(1, 4)$.

The flow separation under secondary crosswind conditions show similar trends to those observed under primary crosswind conditions. The flow separation is greater at the centre fan-unit $(1, 4)$ than at the corner fan-unit $(1, 1)$ and increases as the crosswind velocity increases. However, the separation under secondary crosswind conditions is greater than under primary crosswind conditions, which is consistent with the differences in volumetric effectiveness

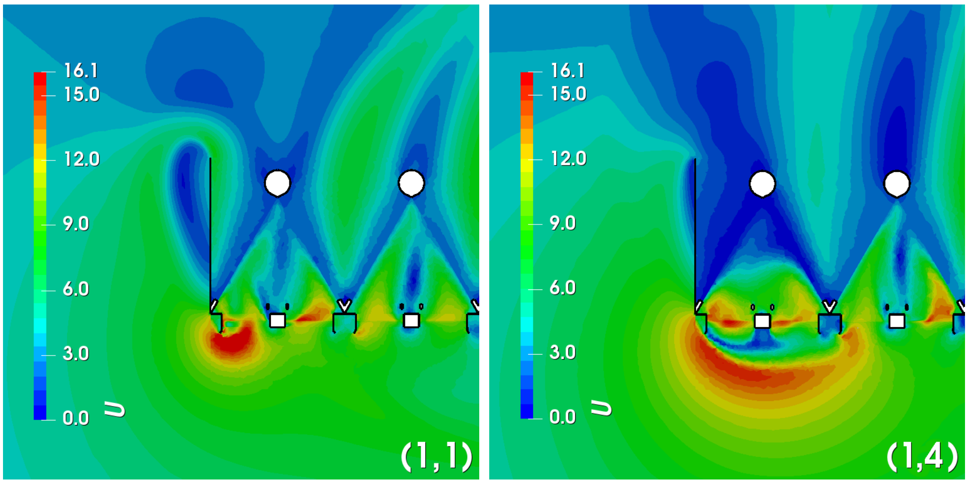

Figure 5.30: Forced Draft Flow Separation at Leading Edge ($U_x = 3$ m/s)

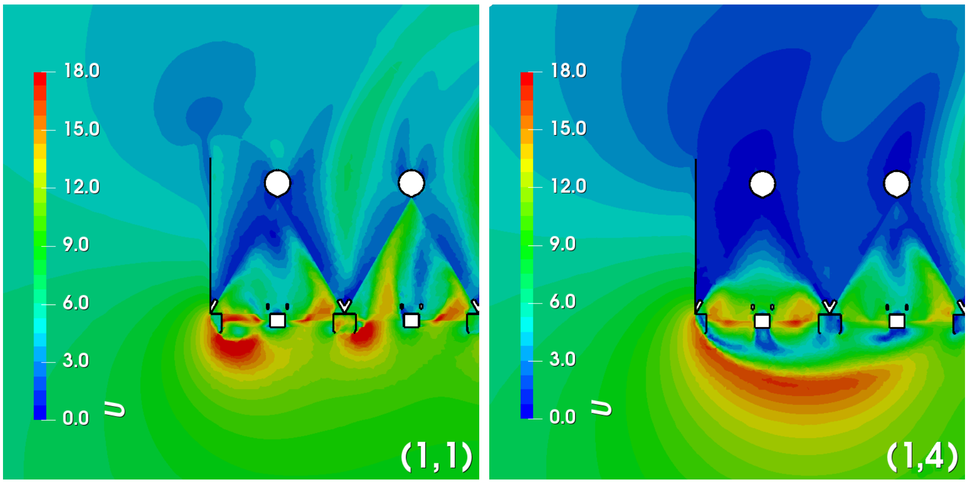

Figure 5.31: Forced Draft Flow Separation at Leading Edge ($U_x = 6$ m/s)

shown.

An additional observation can be made regarding the flow at the outlet of the plenum chambers. Under secondary crosswind conditions the flow over the top of the ACC is perpendicular to the A-frame's steam ducts. As the crosswind velocity increases, a stagnant region between the windwall and the upwind side of the A-frame starts to develop.

Heat Exchanger Performance

The total heat transfer rate per fan-unit and mean heat exchanger inlet air temperatures of the Forced Draft ACC under secondary crosswinds of 3, 6, and 9 m/s are shown in Figs. 5.33 to 5.35. The results show similarities to

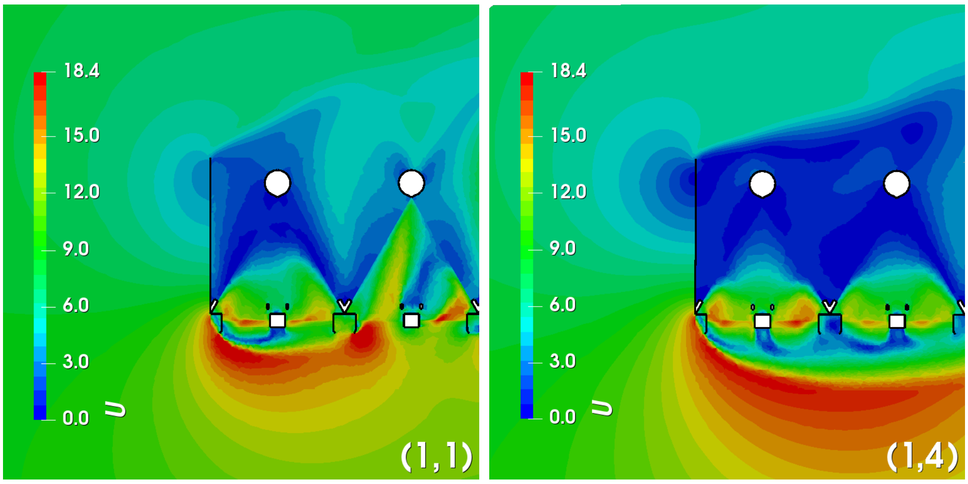

Figure 5.32: Forced Draft Flow Separation at Leading Edge ($U_x = 9$ m/s)

that seen under primary crosswind conditions.

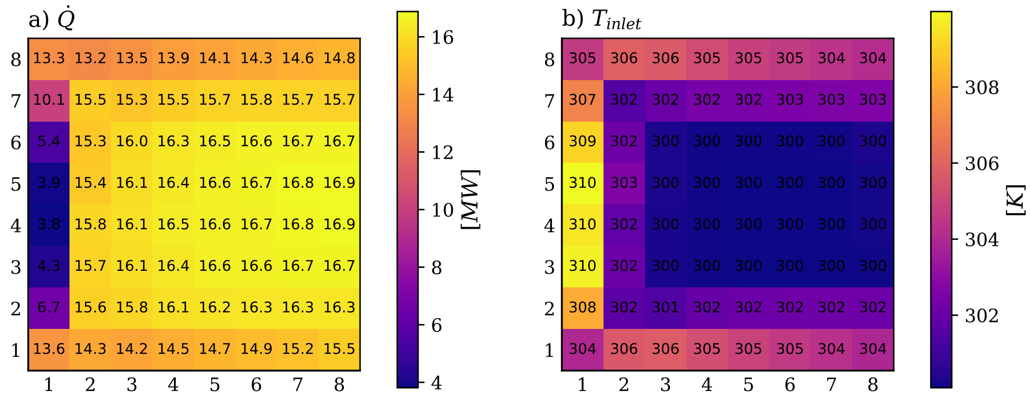

Figure 5.33: Forced Draft Heat Exchanger Performance ($U_x = 3$ m/s)

The mean heat transfer rate at the leading edge fan-units ($i = 1$) decreases from the norm by 10.2, 13.5 and 14.3 MW under crosswinds of 3, 6 and 9 m/s respectively. The mean heat exchanger inlet air temperatures of the above-mentioned fan-units increases by 8.0, 11.2 and 20.3 K. The decrease in heat transfer rate and the increase in inlet air temperatures at the leading edge fan-units are greater under secondary crosswind conditions than they are under primary crosswinds.

Greater reverse flow was noted at the leading edge fan-units under secondary crosswinds than under primary crosswinds. As a result the mean inlet air temperatures of the fan-units immediately downwind of the centre most fan-units ($3 \leq j \leq 6$) at the leading edge increase from 301.0 K to 302.2, 303.0

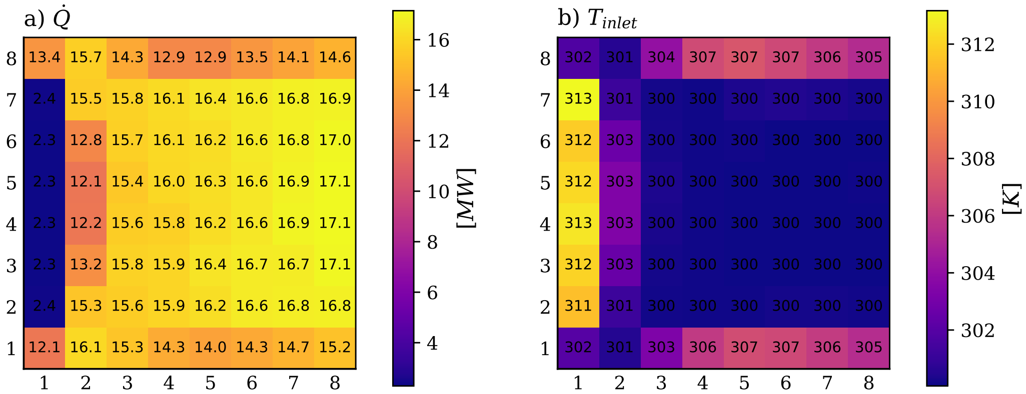

Figure 5.34: Forced Draft Heat Exchanger Performance ($U_x = 6$ m/s)

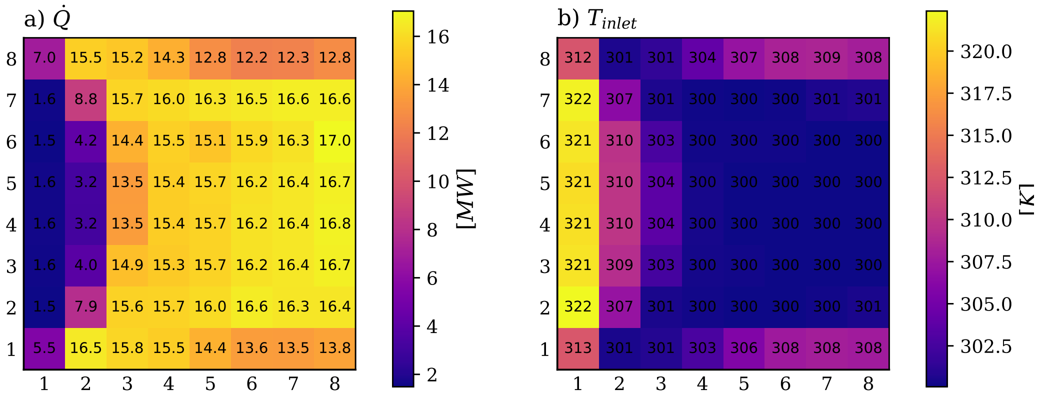

Figure 5.35: Forced Draft Heat Exchanger Performance ($U_x = 9$ m/s)

and 309.8 K under crosswinds of 3, 6 and 9 m/s respectively. The increase is on average 2.6 K greater than that seen under primary crosswind conditions.

The effect of hot plume recirculation is also present under secondary crosswind conditions. The mean inlet air temperatures of the downwind fan-units ($i \geq 3$) at the front ($j = 1$) and back ($j = 8$) sides of the ACC increases to 304.5, 306.2 and 307.8 K at crosswinds of 3, 6 and 9 m/s. The increases are slightly higher than that seen under primary crosswind conditions.

Hot Plume Recirculation

Hot plume recirculation for the 9 m/s secondary crosswind is shown in Figs. 5.36 and 5.37. The velocity and temperature fields are shown on the yz-plane through the centres of three different fan-units, $(4, 1)$, $(6, 1)$ and $(8, 1)$.

The flow field streamlines for the 9 m/s secondary crosswind are shown in Fig. 5.38. Similar to the primary crosswind streamlines shown in Fig. 5.38 the

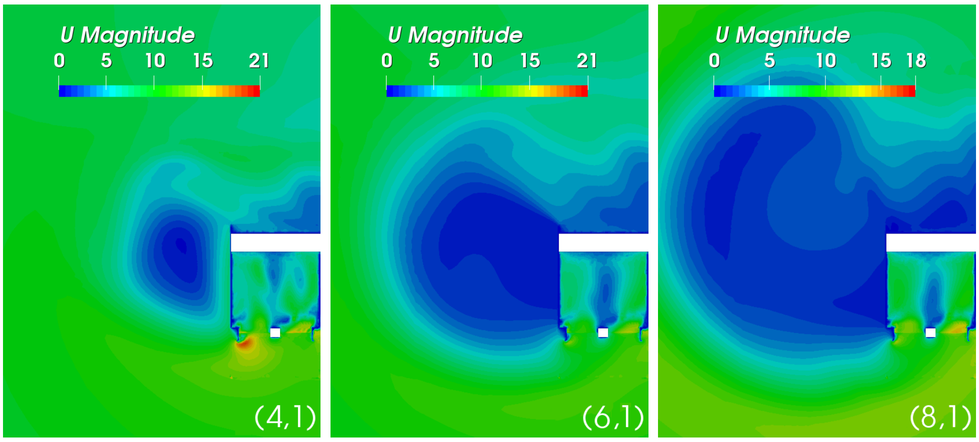

Figure 5.36: Forced Draft Recirculation Velocities ($U_x = 9$ m/s)

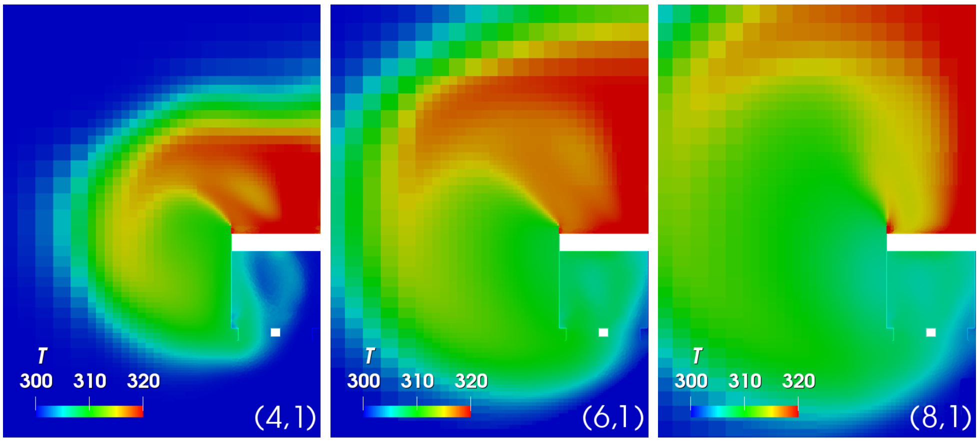

Figure 5.37: Forced Draft Recirculation Temperature ($U_x = 9$ m/s)

vortices form on the ACC's sides that are parallel with the crosswind direction and grow larger as they move further downwind of the leading edge.

The orientation of the A-frames in the ACC, i.e. orthogonal to the crosswind direction, accelerates the flow non-uniformly out of the top of the ACC. This is in contrast with the primary crosswind condition's hot plume recirculation which is more uniform. The accelerated outlet flow increases the growth rate of the vortex being formed.

5.3.4 Comparison of Primary & Secondary Crosswinds

An analysis of the results under both primary and secondary crosswind conditions shows that the crosswinds affect the performance of the leading edge fan-units the most. Under primary crosswinds the leading and trailing edges of the ACC are respectively found at the front and back sides where the L-fan

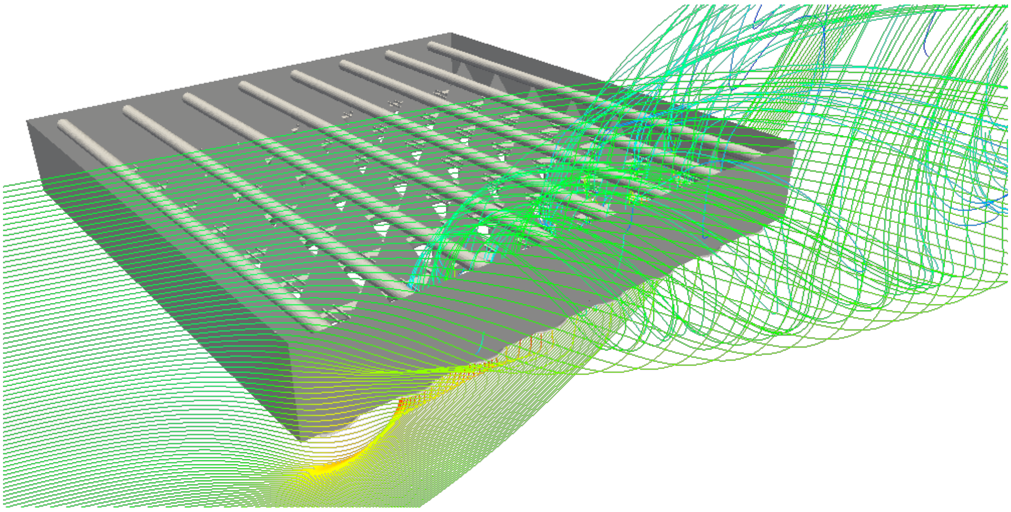

Figure 5.38: Recirculation Streamlines: $U_x = 9$ m/s

is located. Under secondary crosswinds the leading and trailing edges shift to the left and right sides respectively where the N-fan is located. It follows that the fan characteristics of the fan's located at the leading edge will be the deciding factor regarding the performance of those units.

Comparisons of the mean volumetric effectiveness, the mean heat transfer effectiveness and the heat-to-power ratios of the ACC under primary and secondary crosswind conditions are shown in Figs. 5.39 to 5.41. The figures show the performance of the leading edge fan-units as well as that of the entire ACC.

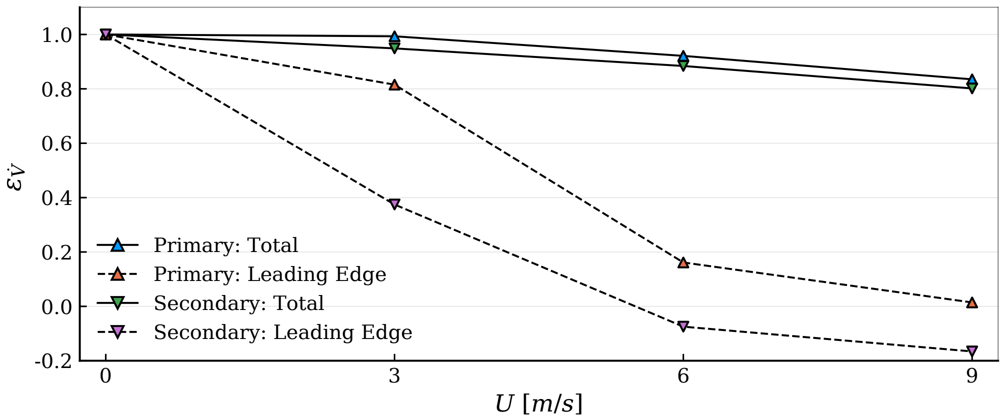

Figure 5.39: Forced Draft Mean Volumetric Effectiveness

The ACC as a whole performs marginally better under primary crosswind conditions of all magnitudes. This is true for the volumetric effectiveness, heat transfer effectiveness and heat-to-power ratios. However, this difference

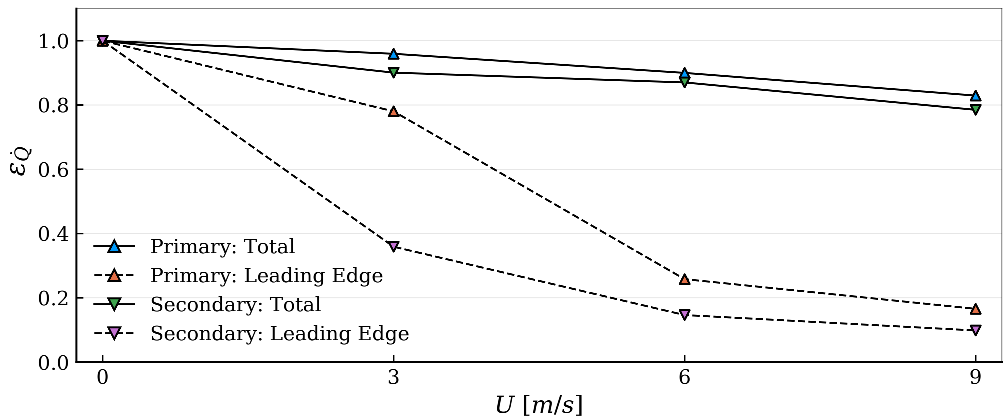

Figure 5.40: Forced Draft Mean Heat Transfer Effectiveness

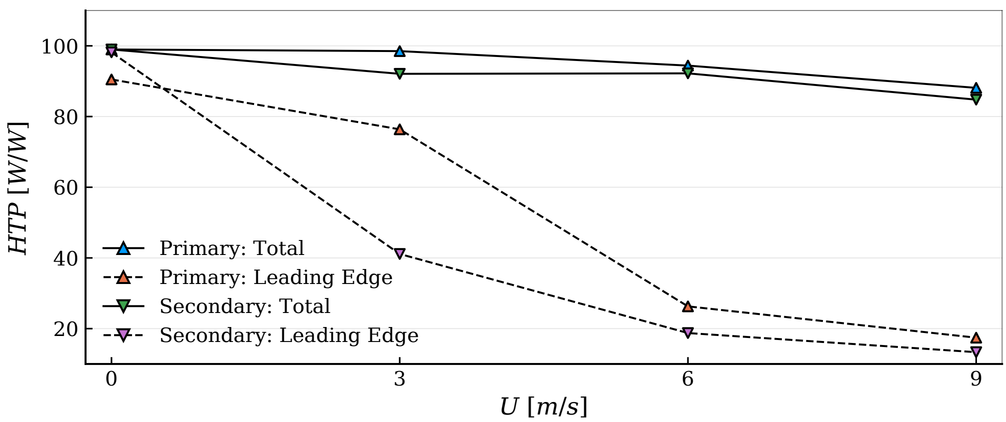

Figure 5.41: Forced Draft Mean Heat-to-Power Ratio

in performance between primary and secondary crosswinds for the entire ACC is negligible when compared to the difference shown at the leading edge fan-units.

The mean leading edge volumetric effectiveness is higher under primary cross-wind conditions, i.e. when the L-fan is found at the leading edge. At low cross-wind velocities the L-fan performs significantly better than the N-fan with a smaller reduction in volumetric effectiveness. At higher crosswind velocities the L-fan still performs better than the N-fan, but the difference between the fan-units is less prominent. The difference in performance between the two fans is attributed to the steeper pressure characteristic curve of the L-fan which allows it to mitigate the effect of flow separation at the leading edge better that the N-fan is able to do. This is consistent with Engelbrecht (2018) who found that using a fan with a greater pressure characteristic at the periphery of the ACC improved the ACC's performance under crosswind conditions.

It is noted that the L-fans are able to maintain a positive volumetric effectiveness at the leading edge under high crosswind velocities which is something that the N-fans fail to do.

The heat transfer effectiveness of the ACC follows the same trend shown for the volumetric effectiveness. For both crosswind conditions the heat transfer effectiveness was shown to be a near direct mapping of the volumetric effectiveness values, with slight deviations from this mapping located primarily at the leading edge. As a result the comparison of the heat transfer effectiveness under different crosswind conditions results in the same conclusions as were made for volumetric effectiveness.

The heat transfer effectiveness remains positive under both crosswind conditions due to the fact that any flow through the fan-unit can only result in a positive heat transfer rate. This results in the difference between the volumetric and heat transfer effectiveness at the leading edge fan-units.

The heat-to-power ratios share similar performance trends with the volumetric and heat transfer effectiveness. The notable difference is that the heat-to-power ratio of the leading edge L-fans starts off lower than that of the leading edge N-fans due to the higher fan power characteristic of the L-fan. However, as the crosswind velocity increases the heat-to-power ratio of the leading edge L-fans does not decrease as much as the leading edge N-fans do. This indicates that as the crosswinds velocity increases the L-fan, despite poor heat-to-power performance under normal operating conditions, is able to perform better than the N-fan.

Hot plume recirculation was identified as the secondary cause of reduced ACC performance, however it remained relatively independent of the crosswind direction. This implies that the hot plume recirculation is also independent of the fans found at the sides where it occurs, i.e. N-fans under primary crosswinds and L-fans under secondary crosswinds. The effect of hot plume recirculation on the overall ACC performance is marginal compared to the performance decrease attributed to flow separation at the leading edge. This is consistent with conclusions drawn in previous studies by Owen (2010) and Engelbrecht (2018).

Chapter 6

Induced Draft ACC Model Development

6.1 Axial Flow Fan Model

6.1.1 Computational Domain

The 3-dimensional computational domain used to validate the compressible implementation of the actuator disk model is shown in Fig. 6.1. The domain differs slightly from that used for the incompressible actuator disk model's validation. The settling chamber is longer but used a slightly smaller diameter, and the atmospheric domain is greater in diameter. The bellmouth used follows a 180° arc, compared to the 90° arc used previously. This reduces the diffulcty in meshing, and increases the quality of the mesh.

6.1.2 Computational Mesh

The computational mesh consists of three distinct regions that were meshed individually before being joined together. The settling chamber and atmospheric region of the computational domain were meshed using a fully unstructured tetrahedral mesh. The fan region that contains the actuator disk model was meshed using a semi-structured triangular prismatic mesh that was created by extruding an unstructured triangular mesh at the upstream disk up to the downstream disk using a regular interval.

A total of 706×10^3 cells were used to discretize the computational domain. A subtotal of 585×10^3 of the cells belong to the unstructured tetrahedral mesh used for the settling chamber and atmospheric regions of the domain. The remaining 121 cells belong to a semi-structured triangular-prismatic mesh used to discretized the actuator disk region.

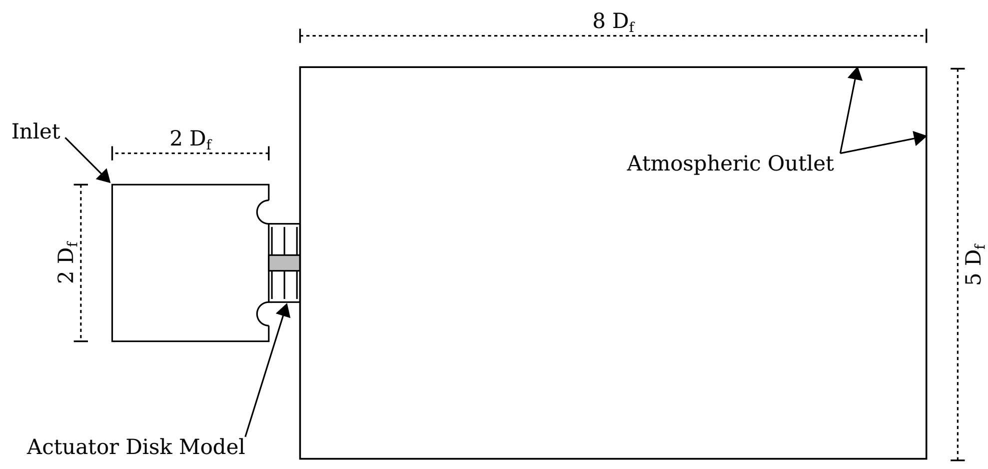

Figure 6.1: BS 848 Domain Schematic (Compressible)

The mesh density is increased near the actuator disk region so that the flow field can be calculated with greater accuracy. The computational mesh has a mean 4.17 faces per cell and a mean non-orthogonality of 13.2°.

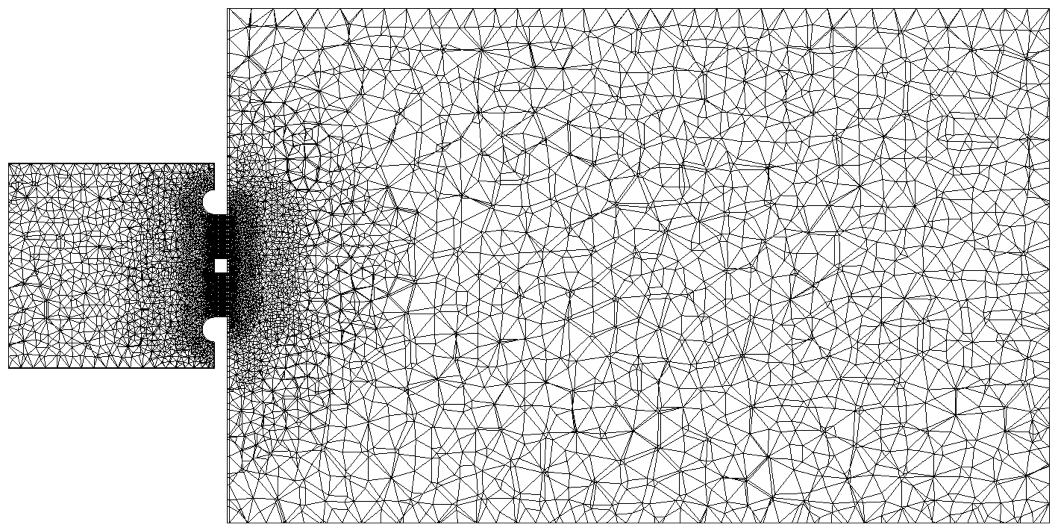

Figure 6.2: BS 848 Mesh Cross-Sectional Slice (Compressible)

6.1.3 Boundary Conditions

The boundary conditions used for the compressible flow BS 848 simulations are tabulated in Table 6.1.

Table 6.1: BS 848 Boundary Conditions (Compressible)

Field	Boundary	Type	Value
p	Inlet	`zeroGradient`	$\nabla p_{\perp} = 0$
	Outlet	`totalPressure`	p_{ref}
	Walls	`zeroGradient`	$\nabla p_{\perp} = 0$
U	Inlet	`flowRateInletVelocity`	$\dot{m}_{ref}$
	Outlet	`pressureInletOutletVelocity`	$\nabla U_{\perp} = 0$
	Walls	`noSlip`	$U = 0$

A total pressure boundary condition is used to constrain the pressure at the outlet of the domain with the reference pressure, p_{ref}, set to 101325 Pa. A zero-gradient boundary condition is used at the inlet of the domain.

The `OpenFOAM` specific `flowRateInletVelocity` boundary condition is used to set a non-uniform velocity at the inlet of the domain with the total flow through the boundary equal to the reference mass flow rate, $\dot{m}_{ref}$. Multiple mass flow rates are used to test the fan model.

The `OpenFOAM` specific `pressureInletOutletVelocity` boundary condition is used to set the velocity at the outlet of the domain. Under outflow conditions this is equivalent to the zero-gradient boundary used during the incompressible flow simulations.

Standard wall-functions are used for the *standard* k-ϵ turbulence model.

6.1.4 Results

The compressible flow actuator disk model's fan static pressure results for the L-fan and N-fan are shown in Figs. 6.3 and 6.4 respectively. The predicted operating region for both axial flow fans are also shown. At high volumetric flow rates the numerical results show good correlation with the experimental results obtained by Augustyn (2013). At lower volumetric flow rates the numerical results under-predict the experimental results.

The compressible flow actuator disk model's fan shaft power consumption results for the L-fan and N-fan are shown in Figs. 6.5 and 6.6 respectively. The numerical results show good correlation with the experimental results for all volumetric flow rates. At higher volumetric flow rates the fan power is marginally over-predicted.

The compressible flow actuator disk model's fan efficiency results for the L-fan and N-fan are shown in Figs. 6.7 and 6.8 respectively. The fan efficiency is derived from the fan static pressure and fan power consumption and therefore the correlation between the numerical and experimental shows similar trends

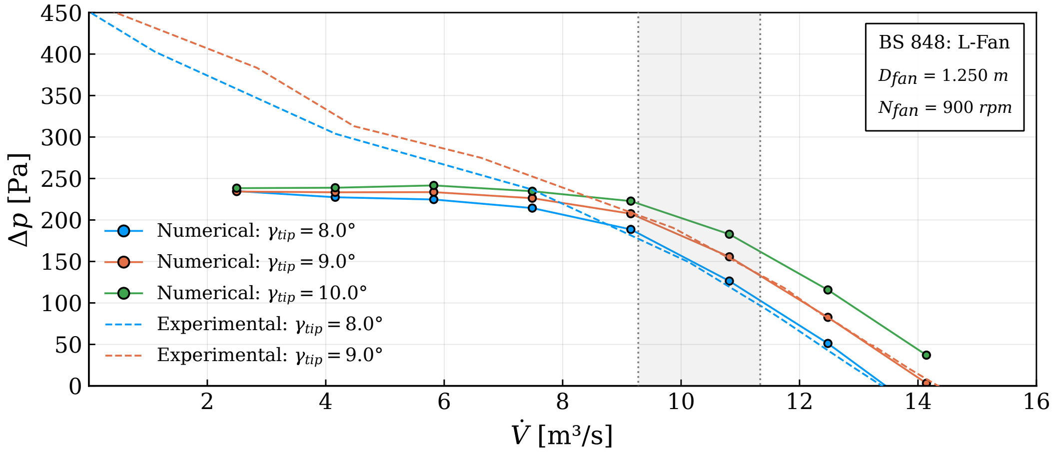

Figure 6.3: L-Fan Static Pressure (Compressible) vs. Volumetric Flow Rate

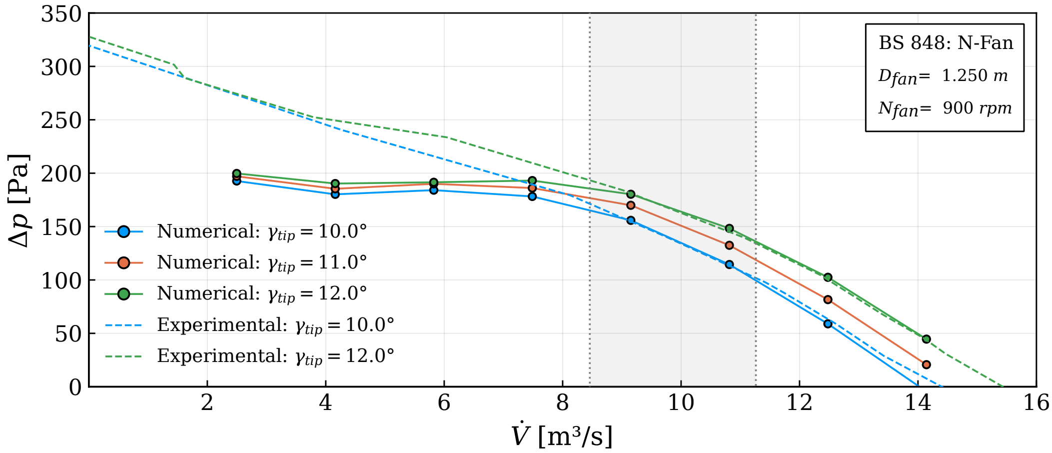

Figure 6.4: N-Fan Static Pressure (Compressible) vs. Volumetric Flow Rate

to those mentioned earlier. At lower volumetric flow rates the fan efficiency is under-predicted, while at higher volumetric flow rates the results are closer but are slightly under-predicted.

6.1.5 Conclusions

The numerical results obtained from the compressible flow actuator disk model correlate well with experimental results obtained by Augustyn (2013).

The under-predicted fan static pressure at lower volumetric flow rates is an expected phenomena of the actuator disk model. The low volumetric flow rates where the fan pressure is under-predicted are well below the predicted operating point, $\dot{V}_{OP}$, where the fan's are expected to function when installed

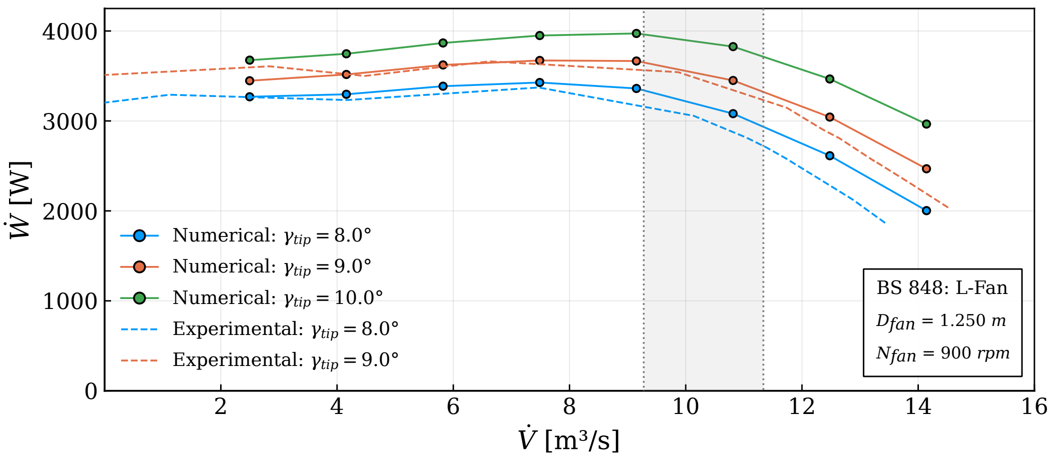

Figure 6.5: L-Fan Shaft Power (Compressible) vs. Volumetric Flow Rate

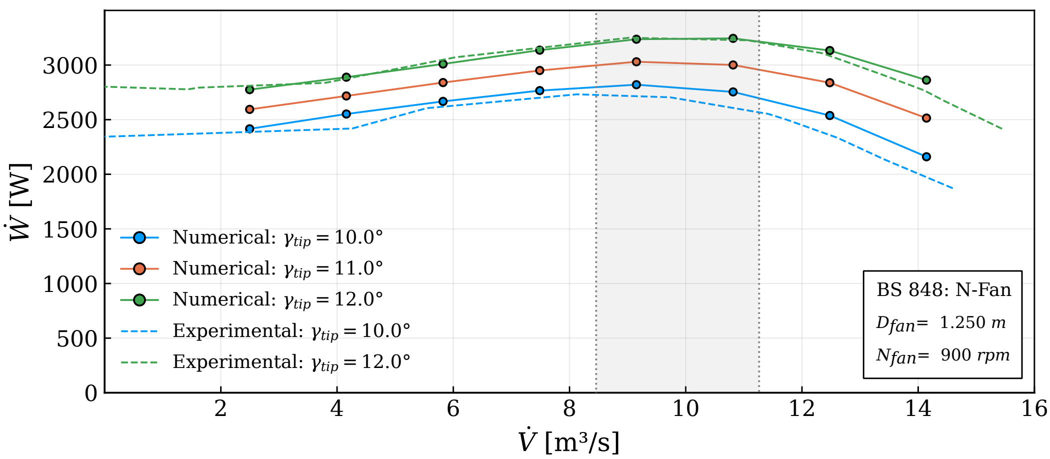

Figure 6.6: N-Fan Shaft Power (Compressible) vs. Volumetric Flow Rate

in the ACC's fan-units.

The performance of the compressible flow actuator disk model's results matches that of the incompressible flow actuator disk model's results reasonably well.

6.2 Heat Exchanger Model

The heat exchanger modeled is based on an elliptical finned tube heat exchanger tested by Zietsman and Kröger (2010).

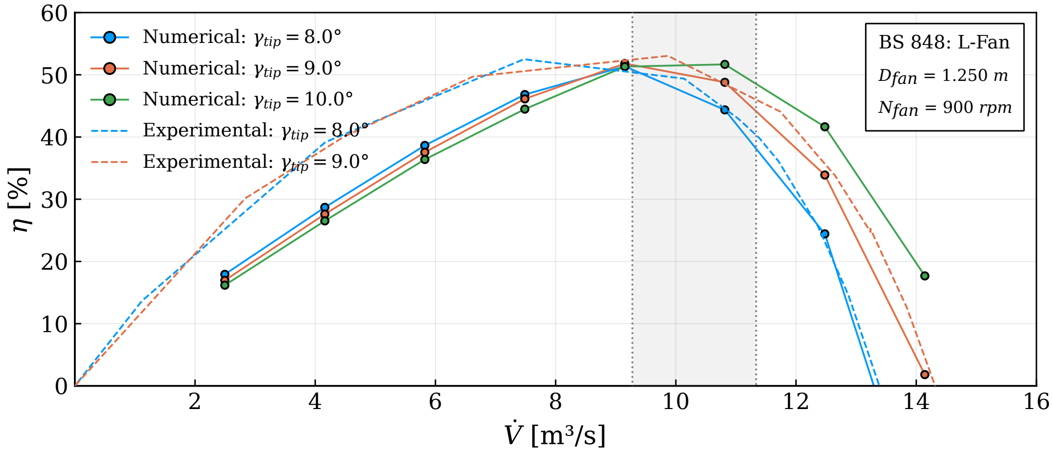

Figure 6.7: L-Fan Static Efficiency (Compressible) vs. Volumetric Flow Rate

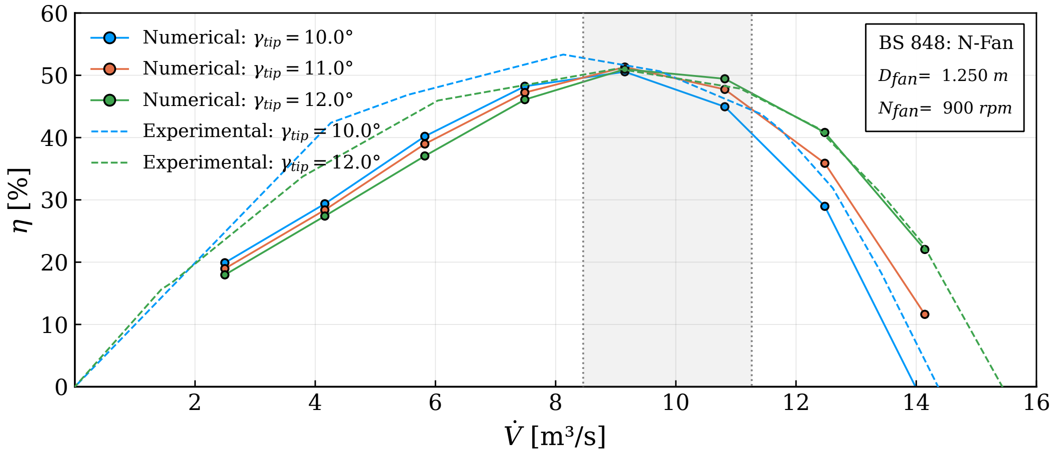

Figure 6.8: N-Fan Static Efficiency (Compressible) vs. Volumetric Flow Rate

6.2.1 Computational Domain & Mesh

The same computational domain used in the incompressible flow heat exchanger simulations is used for the compressible flow simulations. The computational mesh is shown in Fig. 6.9. The mesh is comprised entirely of hexahedral cells, using a total of 43750 hexahedral cells to discretized the domain.

6.2.2 Boundary Conditions

The boundary conditions used for the compressible flow heat exchanger simulations are tabulated in Table 6.2. The boundary conditions used in the current compressible flow heat exchanger model simulations are similar to those used in the incompressible flow heat exchanger model's simulations, with modifications made as required by the compressible flow solver.

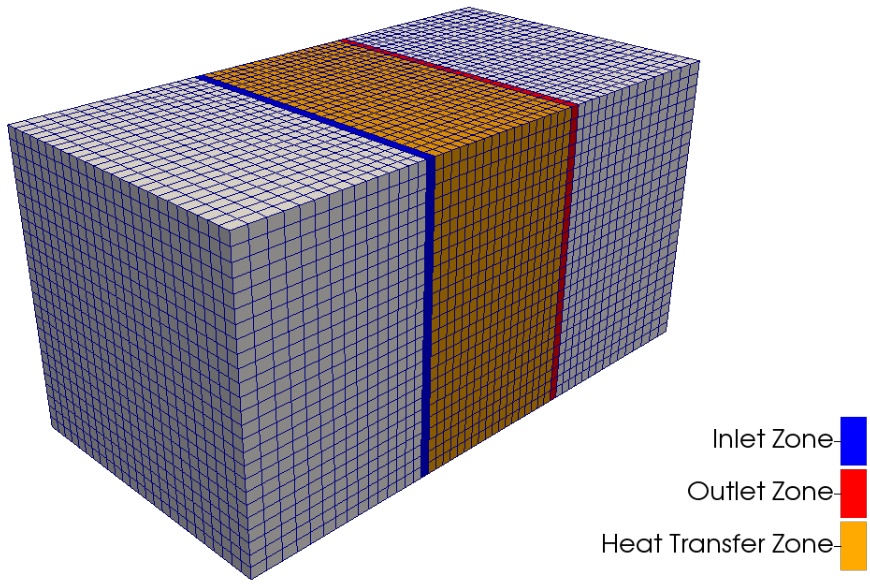

Figure 6.9: Heat Exchanger Domain Mesh (Compressible)

Table 6.2: Heat Exchanger Boundary Conditions (Compressible)

Field	Boundary	Type	Value
p	Inlet	`totalPressure`	p_{ref}
	Outlet	`zeroGradient`	$\nabla p_{\perp} = 0$
	Sides	`symmetry`	$\nabla p_{\perp} = 0$
U	Inlet	`fixedValue`	U_{ref}
	Outlet	`zeroGradient`	$\nabla U_{\perp} = 0$
	Sides	`symmetry`	$U_{\perp} = 0$
T	Inlet	`fixedValue`	T_{ref}
	Outlet	`zeroGradient`	$\nabla T_{\perp} = 0$
	Sides	`symmetry`	$T_{\perp} = 0$

A total pressure boundary condition is used to constrain the pressure at the inlet of the domain with the reference pressure, p_{ref}, set to 100236 Pa. A zero-gradient boundary condition is used to constrain the pressure at the outlet of the domain, while a symmetry boundary condition is used at the sides of the domain.

A fixed value boundary condition is used to set a uniform velocity field at the inlet of the domain. Multiple reference velocities, U_{ref}, are used to test the heat exchanger model at various volumetric flow rates, with the velocities calculated to match the various experimental mass flow rates. A zero-gradient boundary condition is used to set the velocity at the outlet of the domain, while a symmetry boundary condition is used at the sides of the domain.

A fixed value boundary condition is used to set a uniform temperature field at the inlet of the domain. The reference temperature, T_{ref}, is set to match that measured for each experimental flow rate. A zero gradient boundary condition is used to set the temperature at the outlet of the domain, while a symmetry boundary condition is used at the sides of the domain.

6.2.3 Results

The Darcy-Forchheimmer porosity model provides a near perfect static pressure drop over the heat exchanger when compared to the experimental results (Zietsman and Kröger, 2010), as shown in Fig. 6.10.

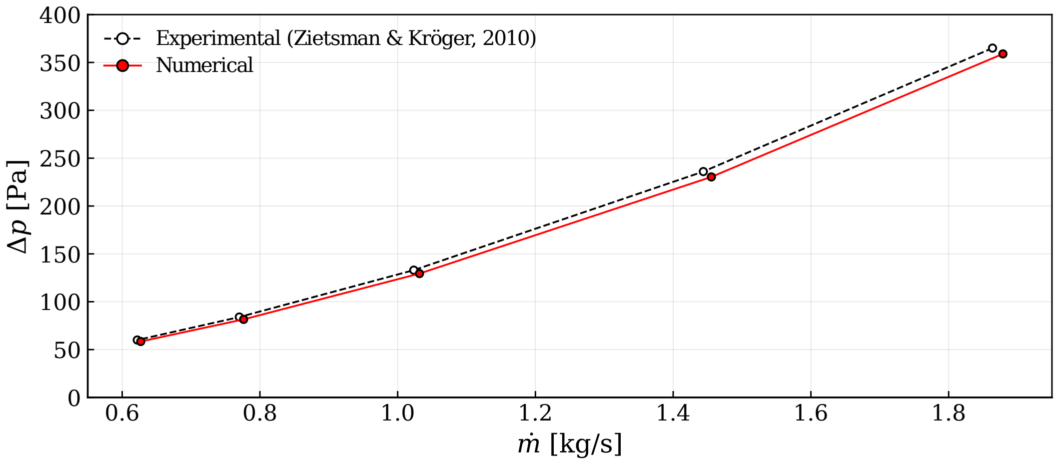

Figure 6.10: Heat Exchanger Isothermal Pressure Drop (Compressible)

The heat transfer rate to the airflow correlates approximately with the experimental results Zietsman and Kröger (2010) as shown in Fig. 6.11. The numerical and experimental heat transfer rates deviate at the lower flow rates where it is slightly under-predicted and at the higher flow rates where it is over-predicted.

6.2.4 Conclusions

The compressible flow heat exchanger model is capable of accurately simulating the pressure drop across the heat exchanger bundle. The numerical heat transfer correlates well with experimental data at the relatively low flow rates where the heat exchanger model is expected to operate, but deviates at higher flow rates further away from the expected operating point of the heat exchanger.

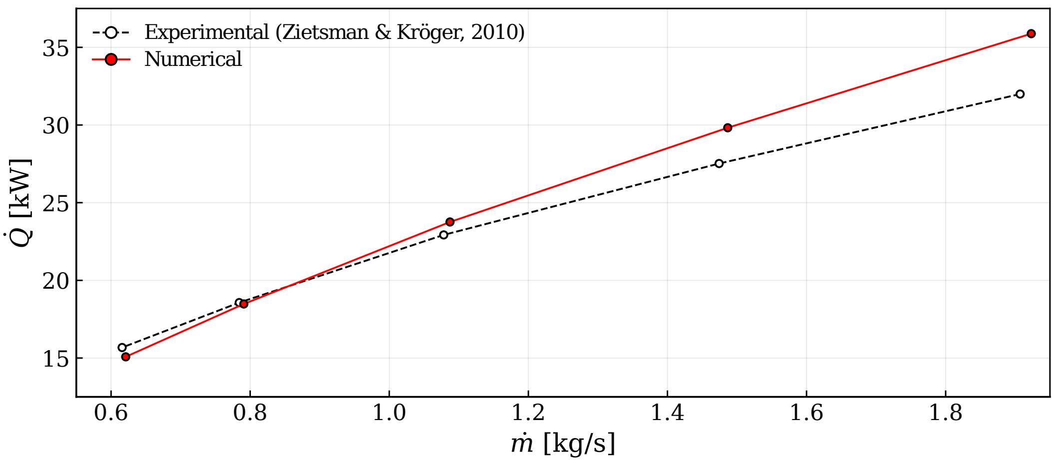

Figure 6.11: Heat Exchanger Heat Transfer Rate (Compressible)

6.3 Single Fan Induced Draft ACC Model

6.3.1 Analytical Model

A draft equation as defined by Kröger (1998) is used to provide a one-dimensional analytical model for preliminary analysis of the Single Fan Induced Draft ACC, similar as to what was done for the Single Fan Forced Draft ACC. The results of the draft equation are used as a reference point for comparison to the CFD results. The draft equation is solved uniquely for both the full scale L-fan and the N-fan, with the results tabulated in Table 6.3.

Table 6.3: Single Fan Induced Draft ACC Analytical Solution

Perfomance Characteristic		**L-Fan**	**N-Fan**	
Fan Blade Angle	γ_{tip}	9.3	11.6	°
Volumetric Flow Rate	$\dot{V}$	831.56	826.19	m^3/s
Fan Static Pressure Rise	Δp	86.61	85.48	Pa
Fan Power Consumption	$\dot{W}$	181.50	171.58	kW
Heat Transfer	$\dot{Q}$	19.42	19.33	MW

6.3.2 Computational Domain

The computational domain for the Single Fan Induced Draft ACC is created with a single induced draft V-frame fan-unit ACC embedded inside a larger atmospheric domain, similar to the computional domain used for the Single Fan Forced Draft ACC. The computational domain is shown in Fig. 6.12, and the domain dimensions are tabulated in Table 6.4.

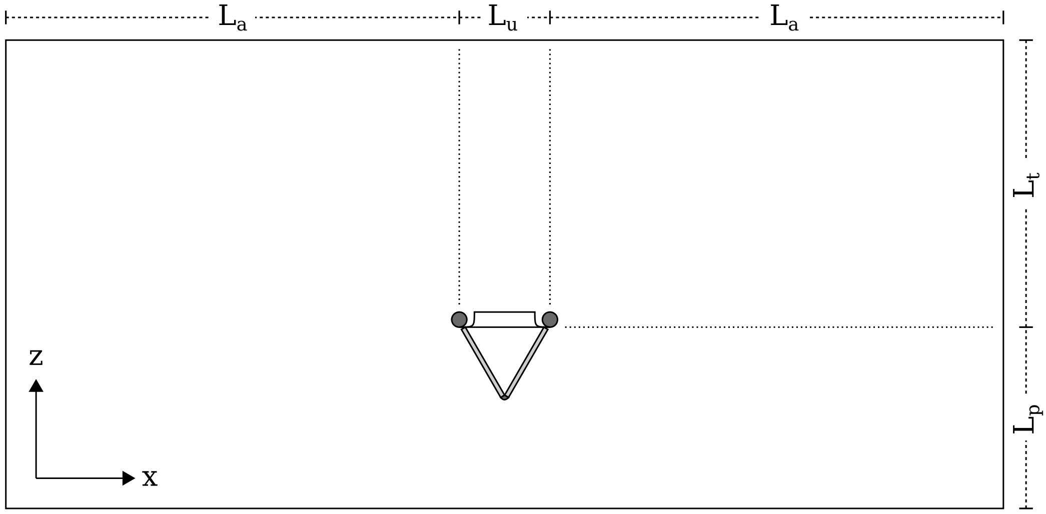

Figure 6.12: Single Fan Induced Draft Domain

Table 6.4: Single Fan Induced Draft Domain Dimensions

Dimension	Symbol	Value	
Unit Width	L_u	12.5	m
Platform Height	L_p	60.0	m
Distance to Atmospheric Sides	L_a	155.0	m
Distance to Atmospheric Top	L_t	190.0	m

6.3.3 Computational Mesh

The domain and mesh for the Single Unit Induced Draft ACC are created in a modular fashion and joined together to form the complete domain. The various submesh components created to form the entire computational domain are listed in Table 6.5.

Table 6.5: Single Fan Induced Draft ACC Submesh Components

Submesh Region	Mesh Type	
Actuator Disk	Triangular-Prismatic	Untructured
Heat Exchanger	Hexahedral	Structured
Fan-Unit Lower	Triangular-Prismatic	Unstructured
Fan-Unit Plenum	Tetrahedral	Unstructured
Fan-Unit Upper	Tetrahedral	Unstructured
Atmosphere	Hexahedral	Structured

The computational domain is discretized using total of 5.5×10^6 cells which have a mean 5.5 faces per cell and a mean non-orthogonality of 7.1°. The mesh primarily consists of 3.8×10^6 hexahedral cells of which the majority are used in the atmospheric domain. The remainder of the domain is discretized using 488×10^3 triangular-prismatic cells and 1.1×10^6 tetrahedral cells which are used where complex geometries are present. A small number of polyhedral cells (28×10^3) exist as artifacts of mesh refinement.

An isolated section of the computational mesh near the fan-unit is shown in Fig. 6.13. The hexahedral atmospheric submesh is shown to have been repeatedly refined near the fan-unit such that the atmospheric mesh density matches that used in the fan-unit submesh components.

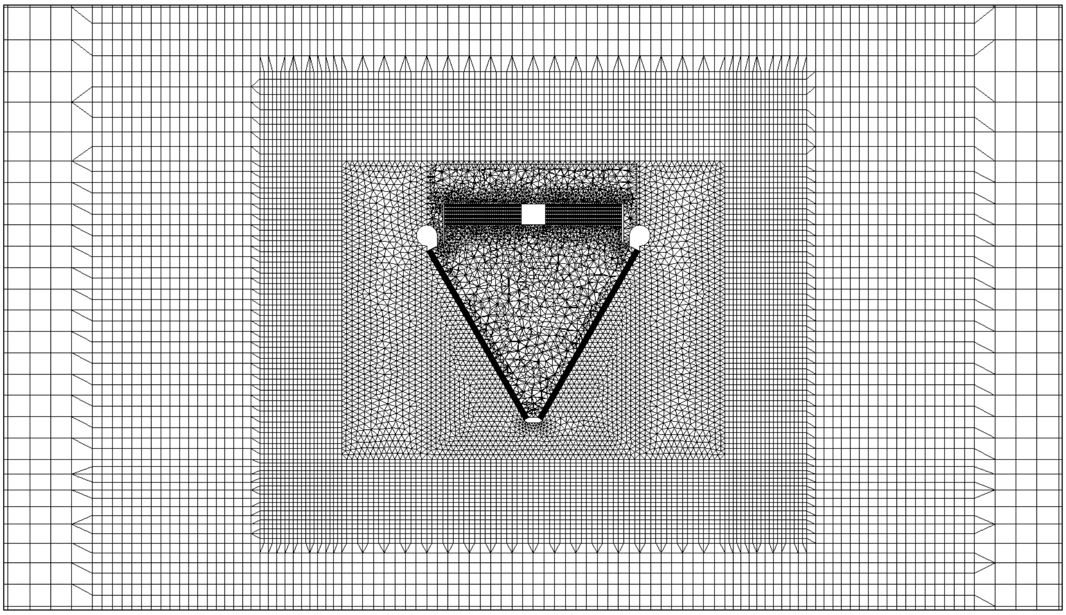

Figure 6.13: Single Fan Induced Draft ACC Mesh

6.3.4 Boundary Conditions

The Single Fan Induced Draft ACC's computational domain's boundary conditions are set to match atmospheric conditions. The boundary conditions used are tabulated in Table 6.6.

The ambient conditions for the simulation are calculated using a reference pressure, p_{ref}, of 101325 Pa and a reference temperature, T_{ref}, of 300 K. For numerical stability the equation of state used to calculate the density (Eqn. (3.9)) assumes a constant reference pressure. This approximation is sufficient for the purposes of this study where the density is primarily dependent on the temperature changes near the heat exchangers, i.e.:

$$\frac{d\rho}{dT} \gg \frac{d\rho}{dp}$$

Table 6.6: Single Fan Induced Draft ACC Boundary Conditions

Field	Boundary	Type	Value
p	Sides/Top	`fixedValue`	Eqn. (6.1)
	Walls	`zeroGradient`	$\nabla p = 0$
	Floor	`fixedValue`	p_{ref}
U	Sides/Top	`pressureInletOutletVelocity`	$\nabla U = 0$
	Walls/Floor	`noSlip`	$U = 0$
T	Sides/Top	`inletOutlet`	$\nabla T = 0$
	Walls	`zeroGradient`	$\nabla T = 0$
	Floor	`fixedValue`	T_{ref}

A fixed value boundary condition is used to constrain the pressure at the atmospheric boundaries with the pressure at the boundaries calculated by:

$$p = p_{ref} - \rho g h \tag{6.1}$$

where h is the height above ground level.

A zero-gradient boundary condition is used to constrain the pressure field at the walls of the ACC.

The `OpenFOAM` specific `pressureInletOutletVelocity` velocity boundary condition is used to for atmospheric boundaries at the top and the side of the domain. For inflow conditions the internal flow field is used to determine the inlet flux, while for outflow conditions a zero-gradient boundary condition is used.

The `OpenFOAM` specific `inletOutlet` boundary condition is used to set the temperature at the atmospheric boundaries of the domain. Under inflow conditions this boundary specifies a reference temperature, T_{ref}, set to 300 K, while under outflow conditions a zero-gradient boundary condition is specified.

Standard wall-functions are used for the *standard* k-ϵ turbulence model.

6.3.5 Results

Fan Angles

The Single Fan Induced Draft ACC Model was solved for a range of fan blade angles, γ_{tip}. The fan blade angles are listed in Table 6.7. The results of the Single Fan Induced Draft ACC simulations are listed in Table 6.8. The results show consistent linear increase in the volumetric flow rate, $\dot{V}$, the fan power, $\dot{W}$, and the heat transfer rate, $\dot{Q}$, for each 1° increase in the fan blade angle.

Table 6.7: Single Fan Induced Draft ACC Blade Angles

Fan	**Blade Angles**
L-Fan	$\gamma_{tip} \in \{8.0°, 9.0°, 9.3°, 10.0°\}$
N-Fan	$\gamma_{tip} \in \{10.0°, 11.0°, 11.6°, 12.0°\}$

Table 6.8: Single Fan Induced Draft ACC Results

L-Fan	8.0°	9.0°	9.3°	10.0°	
$\dot{V}$	838.73	884.01	897.48	928.79	m^3/s
$\dot{W}$	180.15	195.77	200.74	212.81	kW
$\dot{Q}$	17.49	18.20	18.41	18.90	MW

N-Fan	10.0°	11.0°	11.6°	12.0°	
$\dot{V}$	886.19	924.16	946.69	961.74	m^3/s
$\dot{W}$	168.12	182.40	191.49	197.73	kW
$\dot{Q}$	18.24	18.82	19.17	19.41	MW

The L-fan results show that the volumetric flow rate increases at a rate of 45 $m^3/s/°$, the fan power consumption increases at a rate of 16.3 kW/° and the total heat transfer rate increases at a rate of 0.71 MW/°. The N-fan results show that the volumetric flow rate increases at a rate of 37.8 $m^3/s/°$, the fan power consumption increases at a rate of 14.8 kW/° and the total heat transfer rate increases at a rate of 0.59 MW/°.

Flow Fields

Velocity and temperature contour plots on the xz-plane through the Single Fan Induced Draft ACC configured with the L-fan are shown in Fig. 6.14 and for the N-fan are shown in Fig. 6.15. The results are shown for the L-fan set to a nominal blade angle of 9.3° and the N-fan set to a nominal blade angle of 11.6°.

The flow fields predicted by the Single Fan Induced Draft ACC are shown to be very similar. The N-fan shows a marginally larger exit flow at the top of the ACC.

Comparison to Analtyic Draft Equation

The numerical results of the Single Fan Induced Draft ACC model are compared against the operating points obtained by solving the analytical draft equation Eqn. (4.9). A comparison of the numerical results and the analytical draft equation results are listed in Table 6.9. The results are shown for fan blade setting angles of 9.3° and 11.6° for the L-fan and N-fan respectively.

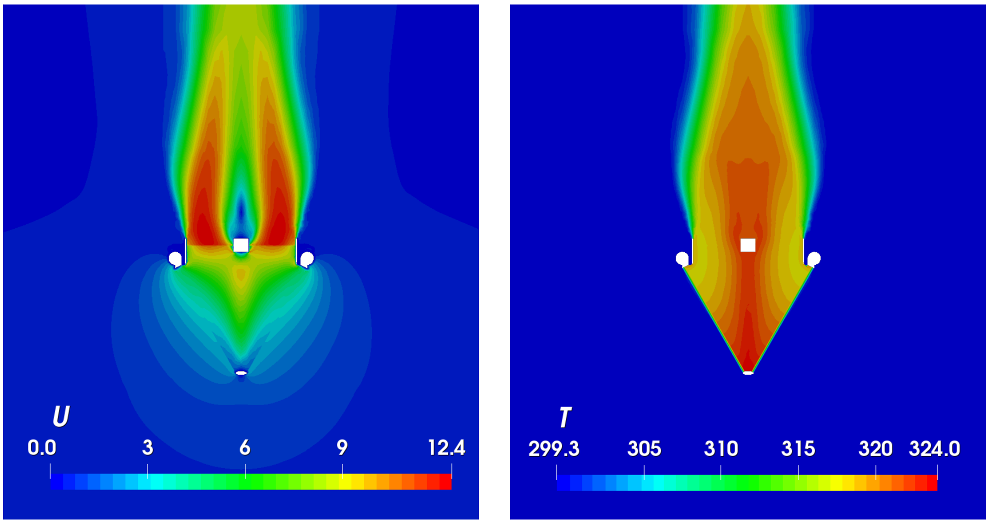

Figure 6.14: L-Fan Single Unit Induced Draft ACC: a) Velocity [m/s], b) Temperature [K]

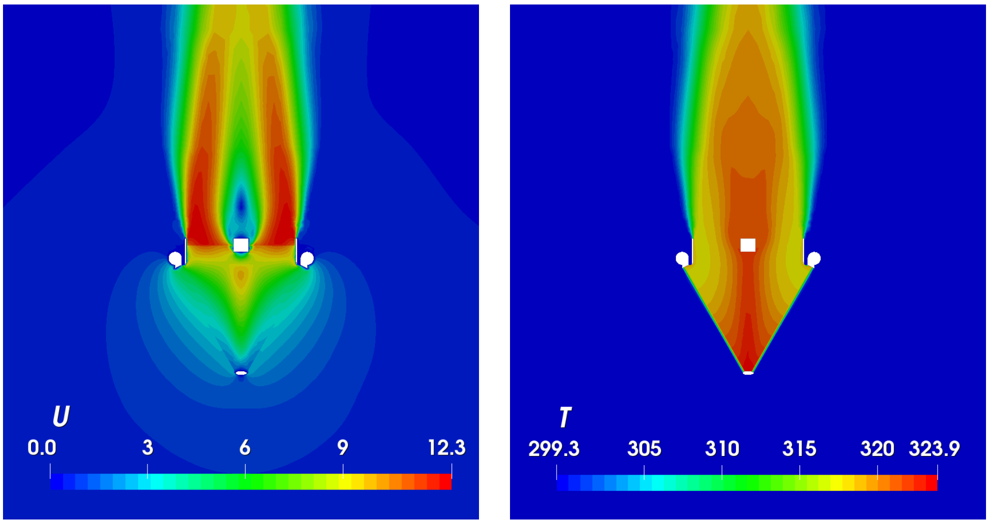

Figure 6.15: N-Fan Single Unit Induced Draft ACC: a) Velocity , b) Temperature

The numerical and analytical results for the L-fan match reasonably well, while the N-fan results match approximately. The numerical volumetric flow rate is 7.9% greater than the analytical flow rate for the L-fan, and 14.6% greater than the analytical for the N-fan. The numerical fan power is 10.6% greater than the analytical fan power for the L-fan, and 11.3% greater for the N-fan. The numerical heat transfer rate is 5.2% less than the analytical heat transfer for the L-fan, while only 0.8% less for the N-fan.

It is to be noted that the analytical draft equation used for the Single Fan Induced Draft ACC is approximate. Very few losses are defined for the induced

Table 6.9: Single Fan Induced Draft ACC Draft Equation Validation

L-Fan ($\gamma_{tip} = 9.3°$)		**Analytic**	**Numerical**	
Volumetric Flow Rate	$\dot{V}$	831.56	897.48	m^3/s
Fan Power	$\dot{W}$	181.50	200.74	kW
Heat Transfer	$\dot{Q}$	19.42	18.41	MW

N-Fan ($\gamma_{tip} = 11.6°$)		**Analytic**	**Numerical**	
Volumetric Flow Rate	$\dot{V}$	826.19	946.69	m^3/s
Fan Power	$\dot{W}$	171.58	191.49	kW
Heat Transfer	$\dot{Q}$	19.33	19.17	MW

draft equation by Kröger (1998) due to the relative novelty of the induced draft V-frame design when compared to the ubiquity of forced draft A-frame designs. Additionally the same limitations regarding the one-dimensional uniform flow approximations made by the analytical draft equation (see § 4.4.5) are present.

Compared to the Single Fan Forced Draft ACC the following differences with the Single Fan Induced Draft ACC are noted:

- Less deviation between the analytically and numerically calculated volumetric flow rates for the Forced Draft ACC,
- Less deviation between the analytically and numerically calculated fan power consumptions for the Forced Draft ACC, and
- Greater deviation between the analytically and numerically calculated heat transfer rates for the Forced Draft ACC.

6.3.6 Conclusions

The numerical model of the Single Fan Induced Draft ACC succesfully combined the compressible flow implementations of the actuator disk model used for the axial flow fan and the Darcy-Forchheimer porosity model and ε-NTU heat transfer model used for the heat exchangers. The numerical results obtained from the Single Fan Induced Draft ACC model are sufficiently close to the analytical draft equation results to validate the combined numerical model, but the differences are noted to be larger than those observed for the Single Fan Forced Draft ACC. Differences between the analtyical draft equation and numerical Single Fan Induced Draft ACC model are attributed to the approximate nature of the induced draft equation.

Chapter 7

Induced Draft ACC Analysis

7.1 Induced Draft ACC Model Setup

7.1.1 Computational Domain

The Induced Draft ACC is compromised of an 8 $\times$ 8 array of V-frame induced draft fan-units which are located in an extended atmospheric domain, similar to the Forced Draft ACC. The computational domain is shown in Figs. 7.1 and 7.2, and the dimensions are tabulated in Table 7.1.

The 64 fan-units are identified using the same (i, j)-indexing scheme used in the Forced Draft ACC, with the layout schematic shown in Fig. 7.1. The (i, j)-indexing scheme corresponds to the x- and y-coordinates of the fan-units. Similar to the Forced Draft ACC the fan-units in the same street (i.e. same i-index) share steam ducts, and the fan-units have separated plenum chambers.

The fan configuration of the Induced Draft ACC is identical to that of the Forced Draft ACC:

1. The L-fan is located at front ($j = 1$) and back ($j = 8$) sides of the ACC and is configured using a blade setting angle $\gamma_{tip} = 9.3°$.
2. The N-fan is used for the remainder of the fan-units ($2 \leq j \leq 7$) and is configured using a blade setting angle $\gamma_{tip} = 11.6°$.

7.1.2 Computational Mesh

The computational domain and mesh for the 64-fan Induced Draft ACC Model re-uses the modular domain and mesh components used in the Single Fan Induced Draft Model, similar to what was done for the Forced Draft ACC

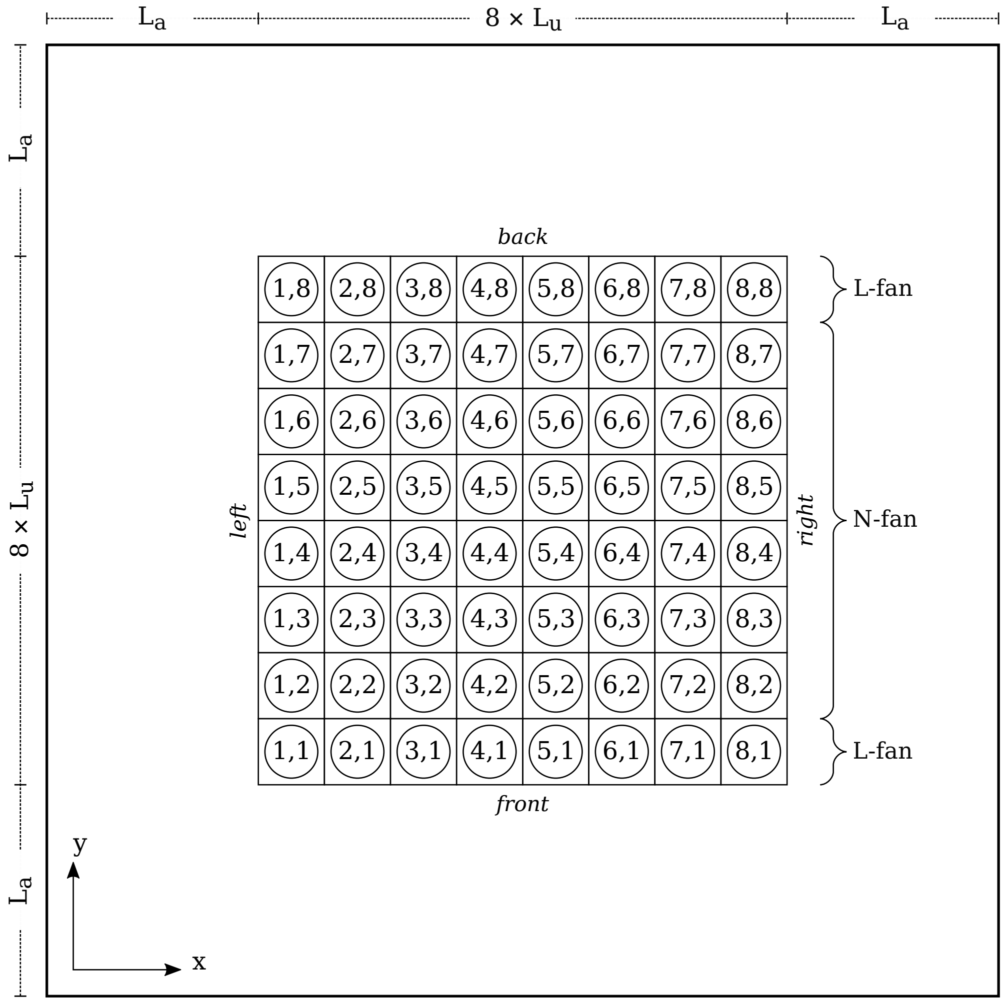

Figure 7.1: Induced Draft ACC Schematic (Top View)

Table 7.1: Induced Draft Domain Dimensions

Dimension	**Symbol**	**Value**	
Unit Width	L_u	12.5	m
Platform Height	L_h	60.0	m
Distance to Atmospheric Sides	L_a	155.0	m
Distance to Atmospheric Top	L_t	210.0	m

Model. The submesh components created to form the entire computational domain were previously listed in Table 6.5.

Each individual fan-unit's submesh consists of 1040×10^3 cells with a mean of 4.263 faces per cell after all the separate components were merged together by connecting adjacent facets of the submeshes. The combined fan-unit submesh

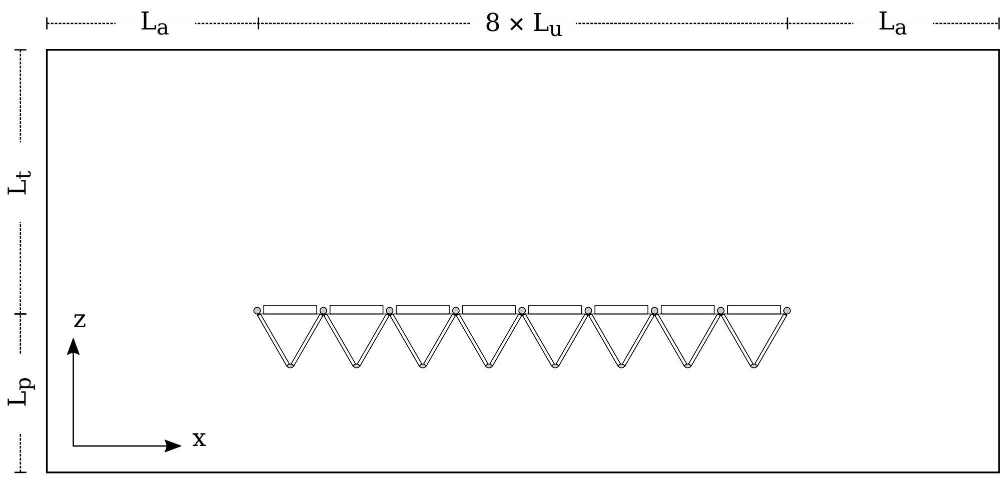

Figure 7.2: Induced Draft ACC Schematic (Front View)

was copied and translated 64 times to create a submesh of the entire 64-fan Induced Draft ACC.

The atmospheric submesh component is the only mesh component created anew due the difference in size between the Single Fan and 64-fan Induced Draft ACCs. The atmospheric submesh was constructed as structured hexahedral mesh with cell sizes biased to create smaller cells near the ACC region. The atmospheric submesh consists of 14.3×10^6 structured hexahedral cells after successive refinements of the atmospheric submesh in the vicinity of the ACC region were applied using a cell-splitting method.

With all submesh components merged and connected the computational mesh for the entire domain consists of 86.8×10^6 cells with a mean of 4.554 faces per cell and a mean non-orthogonality of 11.78°.

7.1.3 Boundary Conditions

The Induced Draft ACC Model's boundary conditions are set to match atmospheric conditions, similar to Single Fan Induced Draft ACC Model. The boundary conditions used are tabulated in Table 7.2.

Similar to the Single Fan Induced Draft ACC Model the ambient conditions for the simulation are calculated using a reference pressure, p_{ref}, of 101325 Pa and a reference temperature, T_{ref}, of 300 K. Similarly for numerical stability the equation of state used to calculate the density (Eqn. (3.9)) assumes a constant reference pressure.

A fixed-value boundary condition is used to constrain the pressure at the

Table 7.2: Induced Draft Boundary Conditions

Field	Boundary	Type	Value
p	Sides/Top	`fixedValue`	Eqn. (6.1)
	Walls	`zeroGradient`	$\nabla p = 0$
	Floor	`fixedValue`	p_{ref}
U	Inlet	`fixedProfile`	Eqn. (3.31)
	Sides/Top	`inletOutlet`	$U = 0$, $\nabla U = 0$
	Walls/Floor	`noSlip`	$U = 0$
T	Sides/Top	`inletOutlet`	T_{ref}, $\nabla T = 0$
	Walls	`zeroGradient`	$\nabla T = 0$
	Floor	`fixedValue`	T_{ref}

atmospheric boundaries using Eqn. (6.1), similar to what was done for the Single Fan Induced Draft Model. Similarly, a zero-gradient boundary condition is used to constrain the pressure field at the walls of the ACC.

The crosswind velocity profile is applied to the appropriate atmospheric boundary directly upwind of the ACC. The crosswinds velocity is applied using a fixed value boundary condition using Eqn. (3.31) to calculate the velocity magnitude. The remaining velocity boundaries are set similar to the Single Fan Induced Draft ACC Model.

The temperature boundary condition are set similar to those used in the Single Fan Induced Draft ACC Model.

Standard wall-functions are used for the *standard* k-ϵ turbulence model.

7.1.4 Simulations

The Induced Draft ACC Model was solved for a total of seven different crosswind conditions, similar to what was done for the Forced Draft ACC Model. The first solution served as the reference case with no crosswind applied, i.e. $U_{ref} = 0$ m/s. Thereafter the numerical model was solved for three different crosswind magnitudes in both the primary and secondary crosswind directions, with 3 m/s, 6 m/s and 9 m/s used as the three reference crosswinds magnitudes (U_{ref}).

The primary and secondary crosswind directions are defined similar to the crosswind directions defined for the Forced Draft ACC. The primary crosswind direction is definded as aligned with the steam ducts, and thus parallel to the heat exchanger bundles, which puts the L-fan configured front row fan-units ($j = 1$) at the leading edge of the ACC. The secondary crosswind direction is defined as perpendicular to the steam ducts and the heat exchanger bundles, which puts the N-fan configured left column fan-units ($i = 1$) at the leading edge of the ACC.

The Induced Draft ACC Model also required parallel computing to solve the flow fields due to its size. All the simulation were run on the computer cluster at the Centre for High Performance Computing (CHPC) in Cape Town. The model was slightly larger in size than the Forced Draft ACC Model and required the use of ten 24-core `Intel Xeon`®(2.6 GHz) compute nodes on the CHPC, with a total runtime of five days per simulation.

The same performance criteria used for the Forced Draft ACC's performance analysis are used for the Induced Draft ACC's perfomance analysis, namely the fan-unit volumetric effectiveness, the fan-unit heat transfer effectiveness and the fan-unit heat-to-power ratio.

7.2 Induced Draft ACC Performance Analysis

7.2.1 Normal Operating Conditions

The results obtained for the Induced Draft ACC under normal operating conditions are presented in this section. Normal operating conditions are defined by the lack of crosswinds, i.e. the reference crosswind velocity is zero: $U_{ref} = 0$ m/s.

Fan Performance

The volumetric flow rate and the fan power of the Induced Draft ACC under normal operating conditions is shown in Fig. 7.3. The results show a mean volumetric flow rate of 968.2 m^3/s and a mean fan power consumption of 161.9 kW.

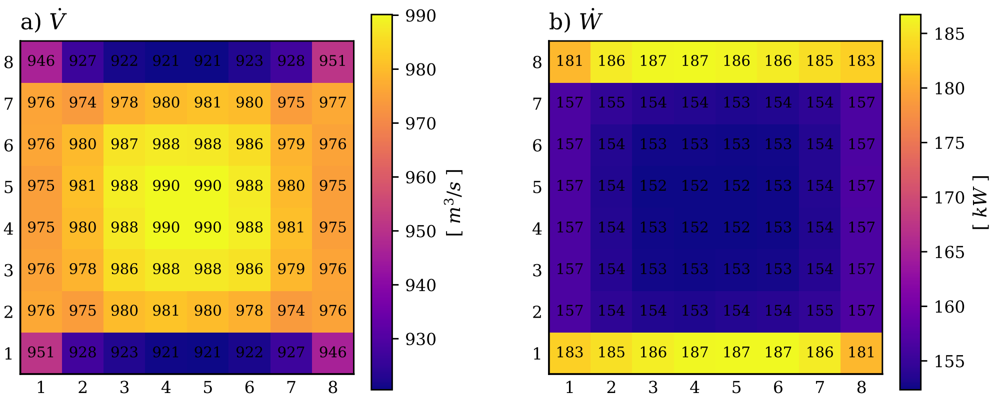

Figure 7.3: Induced Draft Fan Performance ($U_{ref} = 0$ m/s)

Higher volumetric flow rates are seen at the inner fan-units ($2 \leq i \leq 7$ & $2 \leq j \leq 7$) where the mean volumetric flow rate is 982.8 m^3/s, and at the left ($i = 1$) and right ($i = 8$) side fan-units where the mean volumetric flow rate is 975.6 m^3/s. The mean volumetric flow rate at the front and back side fan-units, $j = 1$ and $j = 8$, is lower at 923.4 m^3/s which is 6.0% less than that of the inner fan-units.

Conversely, lower fan power consumption is seen at the inner fan-units where the mean fan power is 153.2 kW, and at the left and right sides fan-units where the mean fan power is 156.7 kW. The mean fan power at the front and back fan-units is 186.0 kW, or 21.4% greater than that of the inner fan-units.

The difference in performance of the front and back side fan-units when compared to the inner fan-units is attributed to both to the use of the L-fan and to flow separation at those fan-units. The steeper power characteristic curve of the L-fan, compared to the N-fan, is directly responsible for the increased fan power consumption of the abovementioned fan-units The decrease in volumetric flow rate is primarily attributed to flow separation at the front and back sides of the ACC. The flow separation phenomena is discussed in further detail in the following section.

Flow Separation

Flow separation at the sides of the Induced Draft ACC is shown in Fig. 7.4. The flow separation is shown as velocity contour plots on the yz-plane between fan-units $(4, 1)$ & $(5, 1)$ at the front side of the ACC and on the xz-plane through the centre of fan-unit $(1, 4)$ at the left side of the ACC.

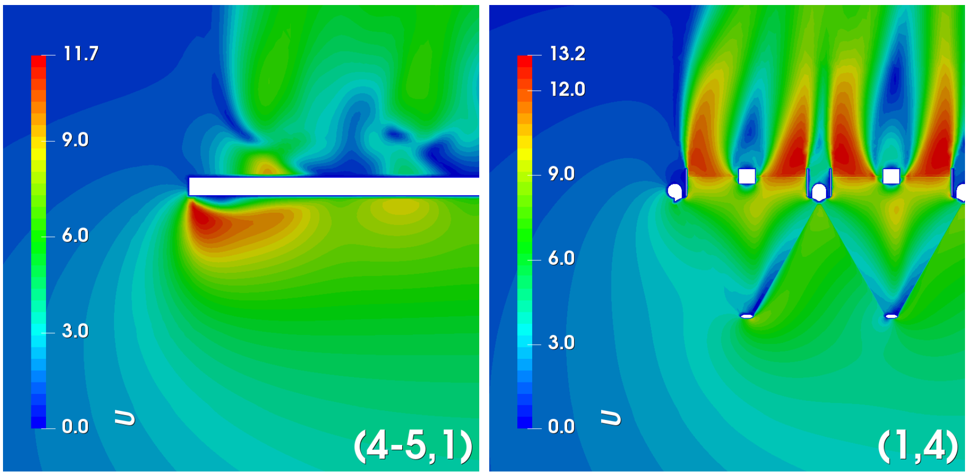

Figure 7.4: Induced Draft Flow Separation ($U_{ref} = 0$ m/s)

Greater flow separation is shown between heat exchangers at the apex between the V-frames of fan-units $(4, 1)$ & $(5, 1)$ where the flow accelerates down into the region between the V-frames. The high velocity region does not extend further than one fan-unit, after which the velocity is relatively uniform.

Less severe flow separation is shown through fan-unit $(1, 4)$ at the left side of the ACC. However the velocity contour plot does show relatively low velocities at the downwind heat exchanger of the V-frame, which is indicative of low flow rates due to decreased pressure downwind of the V-frame caused by flow separation.

Heat Exchanger Performance

The total heat transfer rate and mean heat exchanger inlet air temperature per fan-unit for the Induced Draft ACC are shown Fig. 7.5. The results show a mean heat transfer rate of 19.3 MW and a mean heat exchanger inlet air temperature of 301.6 K.

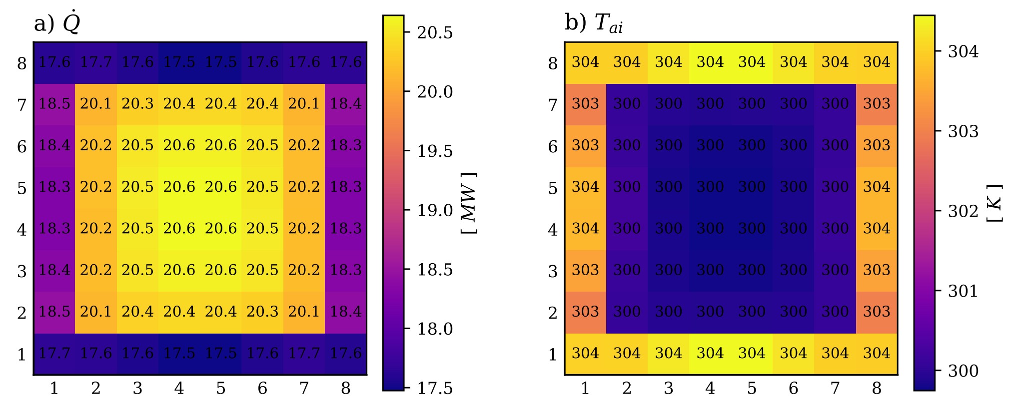

Figure 7.5: Induced Draft Heat Exchanger Performance ($U_{ref} = 0$ m/s)

Greater heat transfer is seen at the inner fan-units ($2 \leq i \leq 7$ and $2 \leq j \leq 7$) of the ACC where the mean heat transfer rate is 20.6 kW. At the left ($i = 1$) and right ($i = 8$) sides the mean heat transfer rate is lower at 18.4 kW, and at the front ($j = 1$) and back ($j = 8$) sides the mean heat transfer rate is even less at 17.6 kW.

The opposite is seen for the heat exchanger inlet air temperatures where the front and back sides have higher mean inlet air temperatures of 304.2 K, and the left and right sides have higher mean inlet temperatures of 303.4 K, while the mean inlet air temperatures of the inner fan-units is lower at 299.8 K.

The mean heat transfer rate follows a combination of the volumetric flow rates, as seen in Fig. 7.3, and the heat exchanger inlet air temperatures. The higher inlet temperatures at the sides of the ACC is responsible for the deviation from the volumetric flow rate and is attributed to flow separation present at those fan-units, as seen in Fig. 7.4.

System Performance

The volumetric effectiveness and heat transfer effectiveness of the Induced Draft ACC under normal operating conditions is shown in Fig. 7.6. The mean volumetric effectiveness for the ACC is 1.07 and the mean heat transfer effectiveness 1.04.

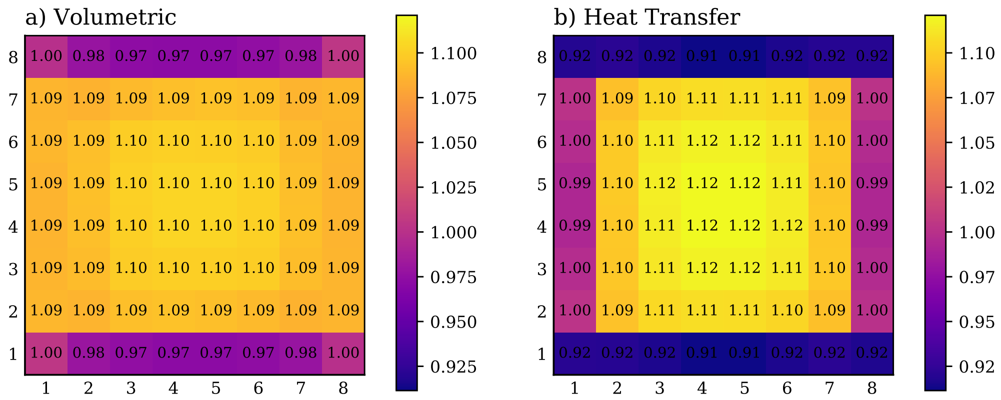

Figure 7.6: Induced Draft System Effectiveness ($U_{ref} = 0$ m/s)

The volumetric effectiveness results follows the same pattern as seen for the volumetric flow rate shown in Fig. 7.3, and similarly the heat transfer effectiveness follows the heat transfer rate shown in Fig. 7.5.

Higher volumetric effectiveness and heat transfer effectiveness values are seen at the inner fan-units ($2 \leq i \leq 7$ and $2 \leq j \leq 7$) of the ACC where the mean volumetric effectiveness is 1.10 and the mean heat transfer effectiveness is 1.12. Lower effectiveness values are seen at the front ($j = 1$) and back ($j = 8$) sides of the ACC with a mean volumetric effectiveness of 0.98 and a mean heat transfer effectiveness of 0.92, which are respectively 11.4% and 17.9% smaller than that of the inner fan-units. The volumetric effectiveness at the left ($i = 1$) and right ($i = 8$) sides of the ACC is very similar to that of the inner fan-units where it only 1.3% lower, however the heat transfer effectiveness for those fan-units is 10.7% lower than that of the inner fan-units.

The differences in effectiveness between the front and back side fan-units and the remaining fan-units, $j \in [2, 7]$, is primarily attributed to the two different axial flow fans used and then secondary to flow seperation at the front and back sides of the ACC. Flow separation is also responsible for the increased heat exchanger effectiveness at the left and right sides of the ACC.

The heat-to-power ratio of the Induced Draft ACC under normal operating conditions is shown in Fig. 7.7. The mean heat-to power ratio of the the ACC under normal operating conditions is 120.6 W/W.

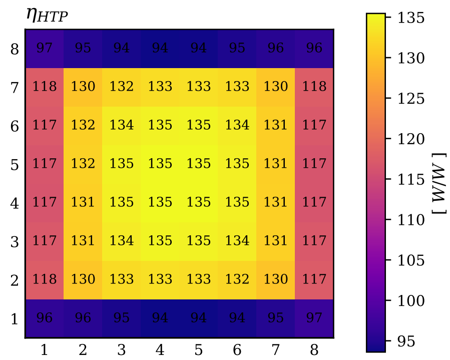

Figure 7.7: Induced Draft Heat-to-Power Ratio ($U_{ref} = 0$ m/s)

The mean heat-to-power ratio of the inner fan-units of the ACC is 134.8 W/W or 11.8% greater than the overall mean. At the left and right sides of the ACC the mean heat-to-power ratio is 94.5 W/W and at the front and back sides is lower at 117.1 W/W, or respectively 29.9% and 13.1% less than that of the inner fan-units.

The lower heat-to-power ratio at the front and back sides is primarily attributed to the higher power consumption of the L-fan used at those fan-units.

7.2.2 Primary Crosswind Conditions

The results obtained for the Induced Draft ACC under primary crosswind conditions are presented in this section. The primary crosswind direction is in the y-direction, i.e. aligned with the steam ducts, and thus parallel to the heat exchanger bundles, which is the same as for the Forced Draft ACC. This orientation puts the L-fan configured front row fan-units ($j = 1$) at the leading edge of the ACC.

System Performance

The volumetric effectiveness and heat transfer effectiveness results of the Induced Draft ACC under primary crosswinds of 3, 6 and 9 m/s are shown in Figs. 7.8 to 7.10.

The results show some correlation between the volumetric effectiveness and the heat transfer effectiveness results. However, the effectiveness values do deviate from one another rather prominently at the left ($i = 1$) and right ($i = 8$) sides of the ACC. Furthermore, as the crosswind velocity increases the deviation in

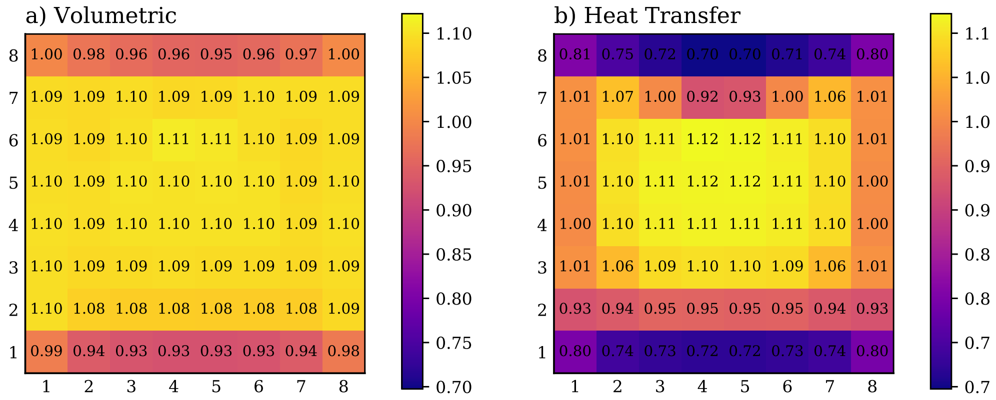

Figure 7.8: Induced Draft System Effectiveness ($U_y = 3$ m/s)

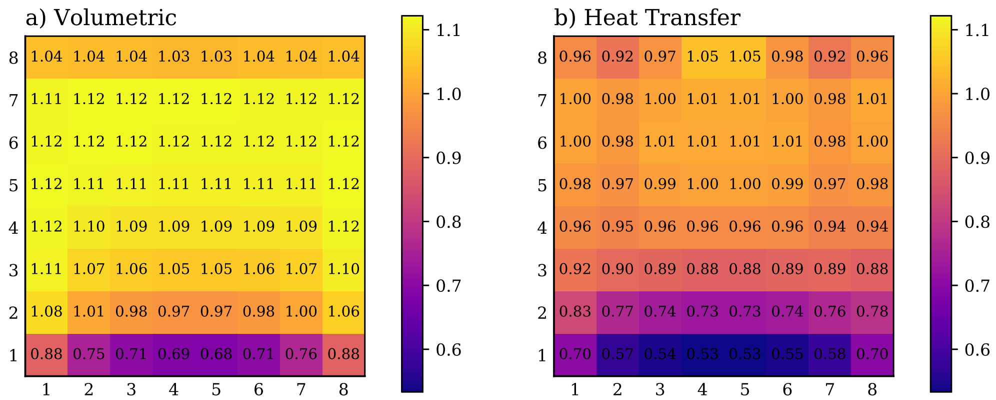

Figure 7.9: Induced Draft System Effectiveness ($U_y = 6$ m/s)

volumetric and heat transfer effectiveness increases and the region where they deviate becomes larger.

The mean volumetric effectiveness of the Induced Draft ACC decreases from 1.07 under normal operating conditions by 0.5% under 3 m/s crosswinds, by 2.3% under 6 m/s crosswinds and by 10.1% under 9 m/s crosswinds.

The mean volumetric effectiveness at the leading edge fan-units ($j = 1$) of the Induced Draft ACC, excluding the corner fan-units, decreases from 0.98 under normal operating conditions by 4.5%, 26.5% and 59.1% under crosswind velocities of 3, 6 and 9 m/s respectively. At the fan-units immediately downwind of the leading edge the mean volumetric effectiveness decreases from 1.09 by 1.1%, 9.4% and 29.2% under the same crosswind velocities.

The mean volumetric effectiveness at the trailing edge ($j = 8$) initially decreases by 1.2% under 3 m/s crosswind velocities from 0.98 under normal operating conditions, where-after it increases by 6.0% and 7.1% under 6 and

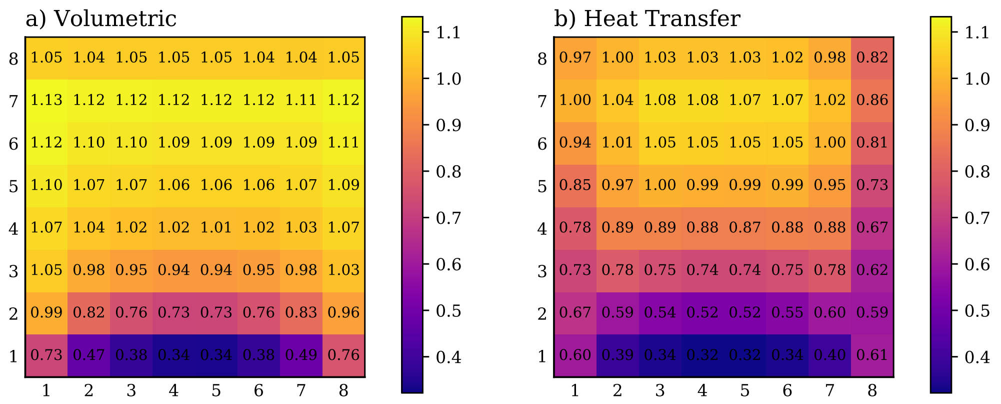

Figure 7.10: Induced Draft System Effectiveness ($U_y = 9$ m/s)

9 m/s crosswind conditions respectively. The increase in volumetric effectiveness is attributed to the increased airflow beneath the ACC supplied by the high velocity crosswind which supplements the airflow supply to the trailing edge fan-units.

The mean heat transfer effectiveness of the Induced Draft ACC under primary crosswind velocities decreases from 1.04 by 6.8% under 3 m/s crosswind velocities, by 14.0% under 6 m/s crosswinds and by 21.7% under 9 m/s crosswinds. The decrease in the heat transfer effectiveness is greater than the decrease in volumetric effectiveness under the same crosswind conditions.

The mean heat transfer effectiveness at the leading edge fan-units, excluding the corner fan-units, decreases from 0.92 under normal operating conditions by 20.5%, 39.9% and 61.5% under crosswind velocities of 3, 6 and 9 m/s respectively. At the fan-units immediately downwind of the leading edge the mean heat transfer effectiveness decreases from 1.10 by 14.1%, 32.4% and 49.6% under the same crosswinds.

At the trailing edge the mean heat transfer effectiveness initially decreased by 21.6% from normal operating conditions under a 3 m/s crosswind where-after it increased from normal operating conditions by 7.0% and 10.6% under 6 and 9 m/s crosswinds respectively. Similar to the volumetric effectiveness, the increase in heat transfer effectiveness is attributed to increased airflow supply to the trailing edge fan-units.

A comparison of the changes between the volumetric effectiveness and heat transfer effectiveness shows a greater decrease in the heat transfer effectiveness than in the volumetric effectiveness. This is present in the overall mean for the Induced Draft ACC, the mean at the leading edge of the ACC and immediately downwind thereof and also at the trailing edge of the ACC.

At crosswind velocities of 9 m/s an asymmetry between the left ($i = 1$) and right ($j = 8$) sides of the ACC is seen in the heat transfer effectiveness. The mean heat transfer effectiveness at the left side is 0.11 or 11.3% greater than that at the right side of the ACC. The asymmetry is not seen at lower crosswind velocities, nor is it seen in any comparable degree for the volumetric effectiveness. The asymmetry is attributed to the rotational flow at the outlet of the axial flow fans interacting with the hot plume recirculation vortices that form at the sides of the ACC.

The heat-to-power ratios of the Induced Draft ACC under primary crosswind of 3, 6 and 9 m/s are shown in Figs. 7.11 to 7.13. Low heat-to-power ratios are found at the leading and trailing edge fan-units, and to a lesser degree at the left and right sides of the ACC. The low heat-to-power ratios at the leading and trailing edge of the ACC is attributed to the the higher power requirement of the L-fan that is used at those fan-units.

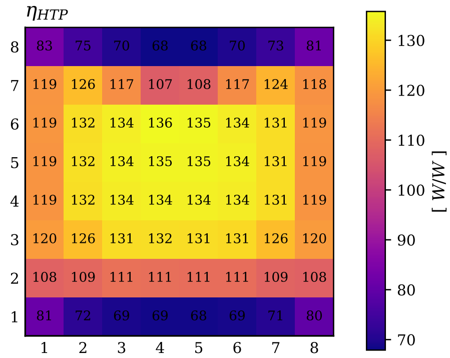

Figure 7.11: Induced Draft Heat-to-Power Ratio ($U_y = 3$ m/s)

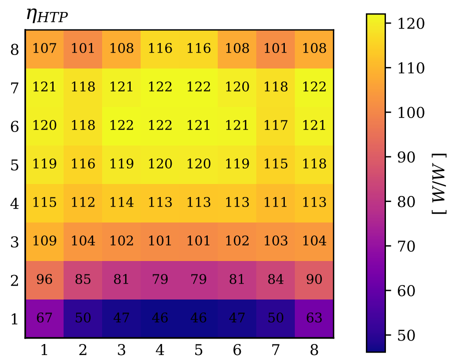

Figure 7.12: Induced Draft Heat-to-Power Ratio ($U_y = 6$ m/s)

The mean heat-to-power ratio of the Induced Draft ACC under primary crosswind conditions decreases from 120.6 W/W to 111.2 W/W under a 3 m/s

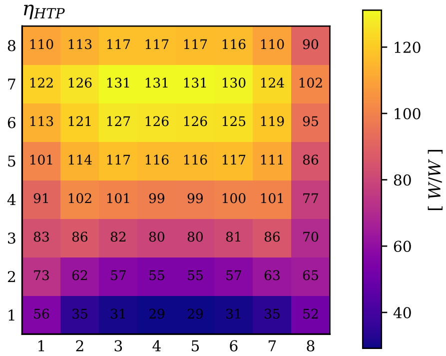

Figure 7.13: Induced Draft Heat-to-Power Ratio ($U_y = 9$ m/s)

crosswind, to 102.5 W/W under 6 m/s crosswind and 92.5 W/W under 9 m/s crosswind.

The mean heat-to-power ratio at the leading edge fan-units of the Induced Draft ACC, excluding the corner fan-units, decreases from 94.5 W/W by 26.3%, 49.3% and 66.5% under crosswind velocities of 3, 6 and 9 m/s respectively. At the fan-units immediately downwind of the leading edge fan-units the heat-to-power decreases from 131.8 W/W by 16.3%, 38.3% and 55.8% respectively. Lastly the mean heat-to power ratios at the trailing edge fan-units initially decrease from 94.5 W/W by 25.2%, where-after it increases by 14.9% and 21.63%.

At high crosswind velocities of 9 m/s the asymmetry seen in the heat transfer effectiveness presents itself again in the heat-to-power ratios at the sides of the ACC. The mean heat-to-power ratios at the left side of the ACC is 14.7 W/W or 12.6% greater than that at the right hand side of the ACC. This is difference is comparable in degree to that seen in heat transfer effectiveness (11.3%), suggesting that the asymmetry is primarily due to differences in heat transfer. Indeed when comparing the difference in the mean fan power consumption between the left and right sides of the ACC the difference is an order of magnitudes less at 1.6% – albeit in the opposite direction.

Flow Separation

The flow separation at the leading edge of the Induced Draft ACC under primary crosswinds of 3, 6 and 9 m/s is shown in Figs. 7.14 to 7.16. The flow separation is shown as velocity field slices on the yz-plane between fan-units $(1-2, 1)$ at the corner of the ACC and $(4-5, 1)$ at the centre of the leading edge.

Greater flow separation is present between fan-units $(4-5, 1)$ than is found between fan-units $(1-2, 1)$, however the difference in maximum flow field

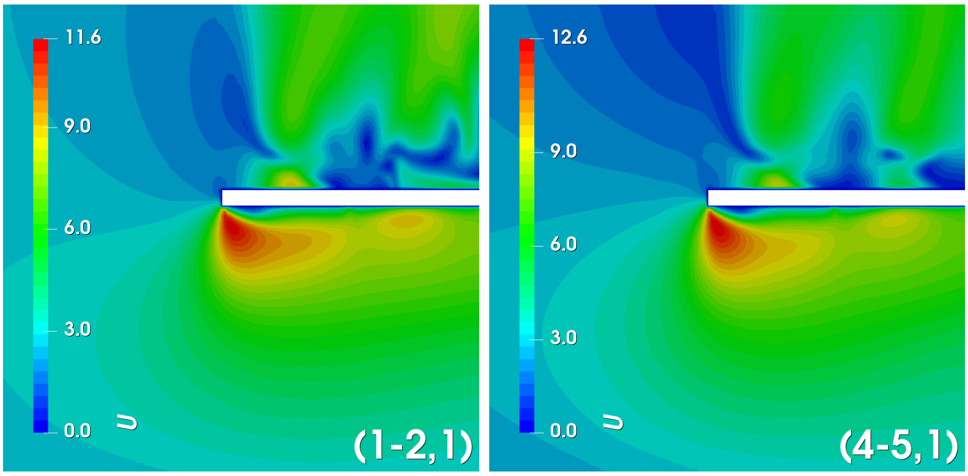

Figure 7.14: Flow Separation at Leading Edge ($U_y = 3$ m/s)

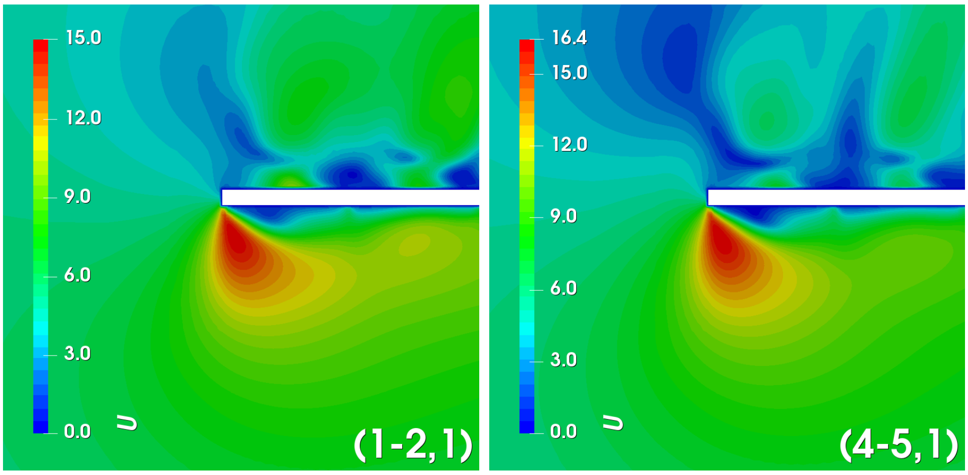

Figure 7.15: Flow Separation at Leading Edge ($U_y = 6$ m/s)

magnitude between the two locations is relatively minimal. The severity of the flow separation is also shown to increase as the crosswind velocity increases with much greater accelerated flow fields existing between the fan-units at the higher crosswind velocities

Heat Exchanger Performance

The total heat transfer and mean heat exchanger inlet air temperatures per fan-unit for the Induced Draft ACC under primary crosswinds of 3, 6 and 9 m/s are shown in Figs. 7.17 to 7.19.

The mean heat transfer rate of the Induced Draft ACC decreases from 19.3 MW under normal operating conditions by 7.0% under a 3 m/s crosswind, by 14.0% under a 6 m/s crosswind and by 21.8% under a 9 m/s crosswind. At the leading

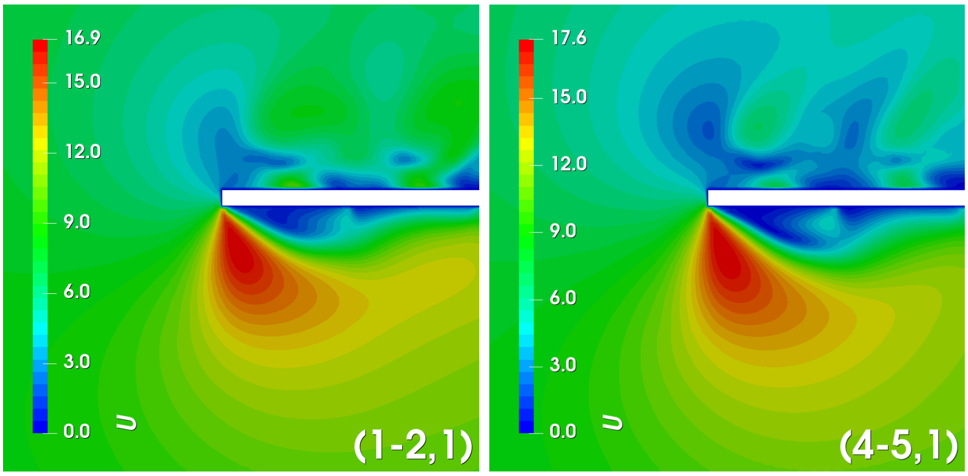

Figure 7.16: Flow Separation at Leading Edge ($U_y = 9$ m/s)

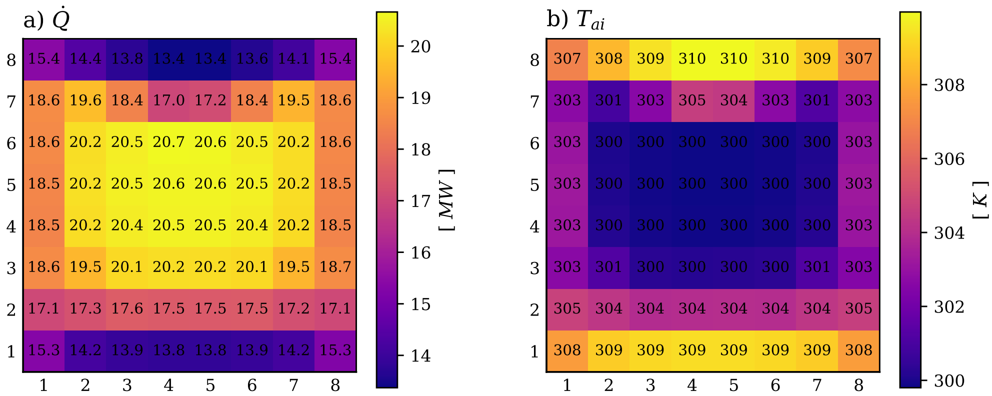

Figure 7.17: Induced Draft Heat Exchanger Performance ($U_y = 3$ m/s)

edge ($j = 1$) the mean heat transfer rate decreases from 17.6 m/s under normal operating conditions by 20.5%, 39.9% and 61.5% under crosswind velocities of 3, 6 and 9 m/s respectively. At the fan-units immediately downwind of the leading edge ($j = 2$) the mean heat transfer rate decreases from 20.3 MW under normal operating conditions by 14.1%, 32.4%, 49.6%.

At the trailing edge of the ACC ($j = 8$) the mean heat transfer rate initially decreased by 21.6% from 17.6 MW under normal operating conditions, whereafter it increased by 7.0% and 10.6% under 6 and 9 m/s crosswind velocities respectively.

At the heat exchangers the mean inlet air temperatures increase from 301.6 K under normal operating conditions to 303.5 K under a 3 m/s crosswind, to 305.8 K under a 6 m/s crosswind and to 306.5 K under a 9 m/s crosswind. At the leading edge the mean inlet air temperatures increase from 304.2 K under

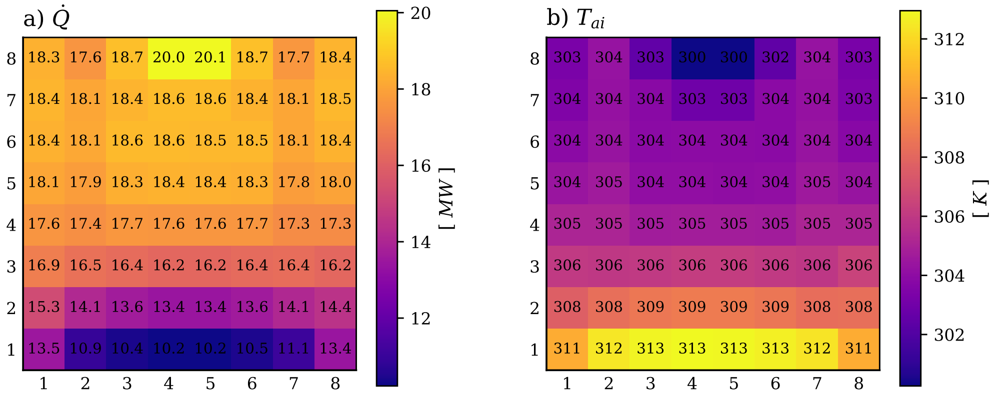

Figure 7.18: Induced Draft Heat Exchanger Performance ($U_y = 6$ m/s)

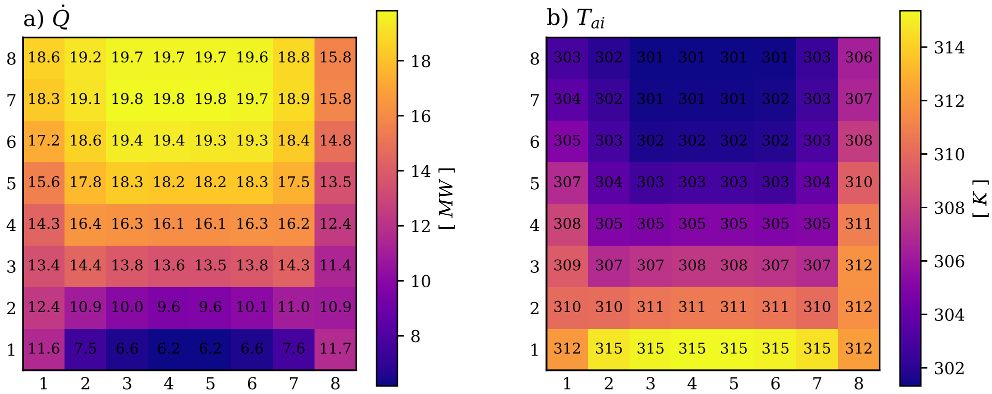

Figure 7.19: Induced Draft Heat Exchanger Performance ($U_y = 9$ m/s)

normal operating conditions to 309.1, 312.7 and 315.19 K under 3, 6 and 9 m/s crosswind velocities respectively. At the fan-units immediately downwind of the leading edge the mean inlet air temperatures increase from 300.0 K to 304.1, 308.6 and 310.4 K respectively.

At the trailing edge of the ACC the mean inlet air temperatures initially increased from 304.2 K to 309.4 K under a crosswind of 3 m/s, where-after it decreased to 302.4 and 301.7 K under crosswinds of 6 and 9 ms/ respectively.

The asymmetry seen in the heat transfer effectiveness and heat-to-power ratios is also seen in the heat transfer rate and in the heat exchanger inlet air temperatures. At crosswind velocities of 9 m/s the left side fan-units ($i = 1$) have a mean heat transfer rate that is 2.07 MW or 11.3% greater than that of the right side fan-units ($i = 8$) which makes it directly comparable to the asymmetry in the heat transfer effectiveness. The heat exchangers of the right side fan-units have inlet temperatures that are 2.5 K greater than that at the left side fan-units. At high crosswind velocities the rotational flow at the outlet of the axial flow fan appears to interact with the hot plume recirculation vortices that form at the sides of the ACC. The effect is an asymmetrical distribution of heated air entering the hot plume recirculation vortices and thus an asymmetrical effect on the performance of the downwind fan-units.

Hot Plume Recirculation

The flow field recirculation at the sides of the Induced Draft ACC is shown for the 9 m/s crosswind in the primary direction. The recirculation is shown for both the left ($i = 1$) and right ($i = 8$) side fan-units as contour plots on the xz-plane through the fan-units located at $j \in \{4, 6, 8\}$. The velocity field recirculation is shown in Figs. 7.20 and 7.21, and the temperature field recirculation is shown in Figs. 7.22 and 7.23.

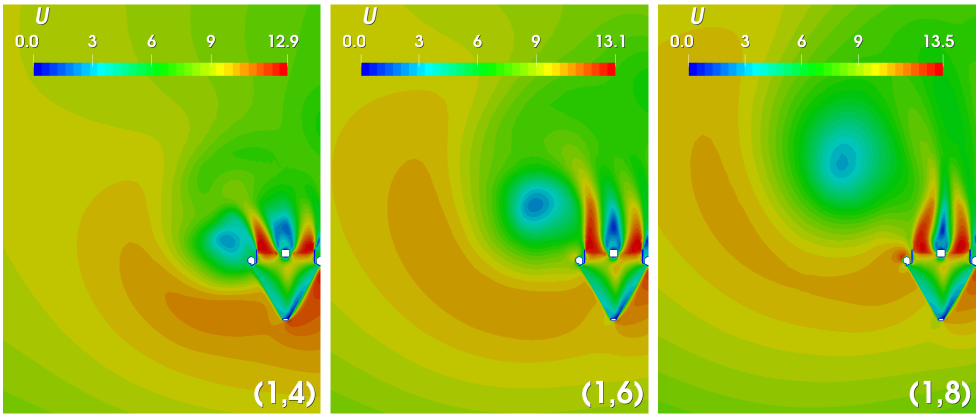

Figure 7.20: Induced Draft Recirculation Velocities ($U_y = 9$ m/s, Left Side)

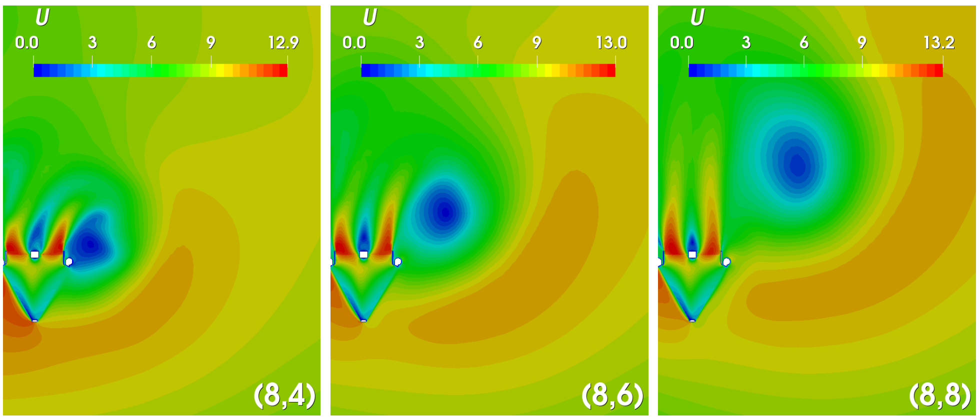

Figure 7.21: Induced Draft Recirculation Velocities ($U_y = 9$ m/s, Right Side)

The flow field recirculation vortices are shown to be attached at the top of the sides of the ACC where they grow larger as they move down the sides of the

ACC. The vortices are shown to be larger on the right hand side of the ACC than on the left hand side. Additionally, the right hand vortex has a larger inner region in the centre of the vortex where the velocity magnitude is very small.

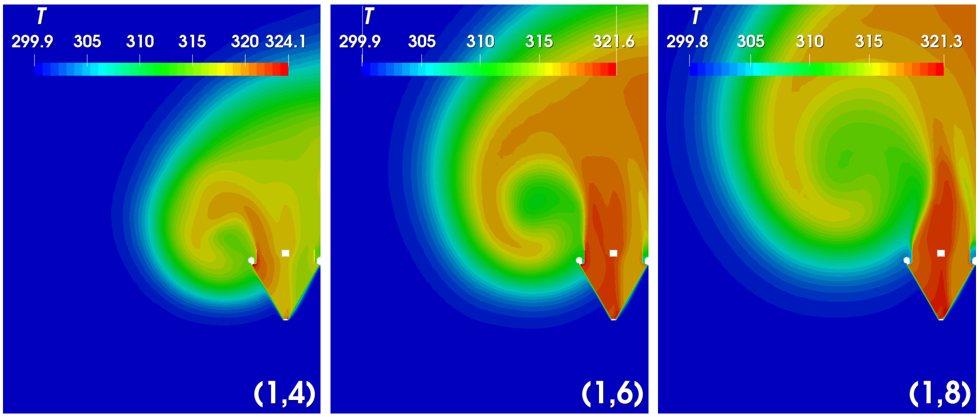

Figure 7.22: Induced Draft Recirculation Temperatures ($U_y = 9$ m/s, Left Side)

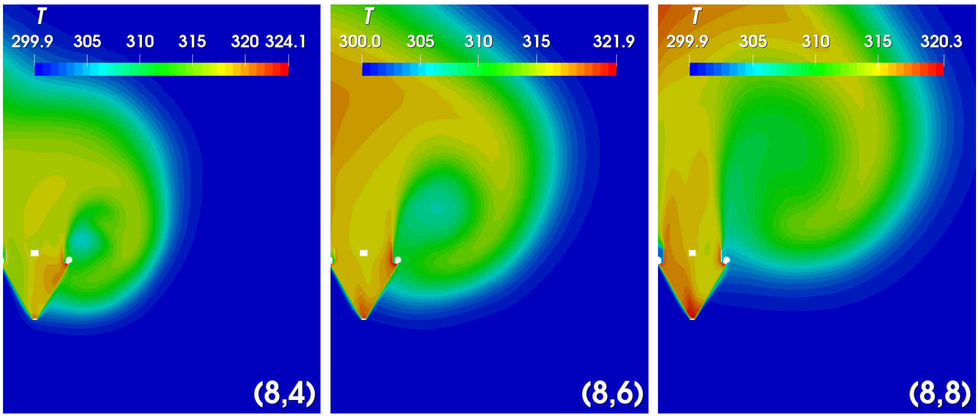

Figure 7.23: Induced Draft Recirculation Temperatures ($U_y = 9$ m/s, Right Side)

The temperature recirculation plots show increased entrainment of hot air ejected out the tops of the fan-units in the vortices that form at the sides of the ACC. As the vortices move down the side of the ACC the vortices start to detach, with the vortices at the left side of the ACC located lower than those found on the right side of the ACC. This results in increased recirculation through the fan-units at the left side of the ACC.

The flow field streamlines for the 9 m/s crosswind in the primary direction is shown in Fig. 7.24. The streamlines show the vortex formation which starts at the corner fan-unit of the leading edge. The vortex grows in size as it moves down the side of the ACC as seen in Figs. 7.21 to 7.23. The vortex's centre moves upwards as it moves down the side of the ACC, with the lowest part of the vortex appearing to remain at the same height.

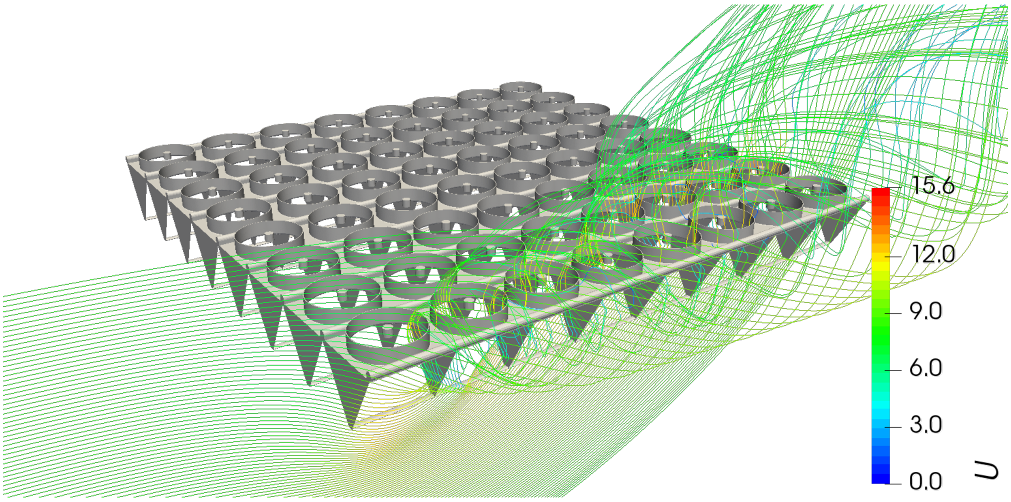

Figure 7.24: Induced Draft Streamlines ($U_y = 9$ m/s)

7.2.3 Secondary Crosswind Conditions

The results obtained for the Induced Draft ACC under secondary crosswind conditions are presented in this section. The secondary crosswind direction is in the x-direction, i.e perpendicular to the steam ducts and the heat exchanger bundles, similar to that done for the Forced Draft ACC. This orientation puts the N-fan configured left column fan-units ($i = 1$) at the leading edge of the ACC.

System Performance

The volumetric effectiveness and heat transfer effectiveness of the Induced Draft ACC under secondary crosswinds of 3, 6 and 9 m/s are shown in Figs. 7.25 to 7.27.

The mean volumetric effectiveness rate of the Induced Draft ACC decreases from 1.07 under normal operating conditions by 0.5% under a 3 m/s crosswind, by 2.6% under a 6 m/s crosswind and by 10.3% under a 9 m/s crosswind. The decreases in the overall mean volumetric effectiveness under secondary crosswind are very similar to that seen under primary crosswind conditions.

The mean volumetric effectiveness at the leading edge fan-units ($i = 1$) of the ACC, excluding corner fan-units, decrease from 1.09 under normal operating condition by 4.1%, 17.9% and 35.7% under 3, 6 and 9 m/s crosswinds respectively. At the fan-units immediately downwind of the leading edge ($i = 2$) the

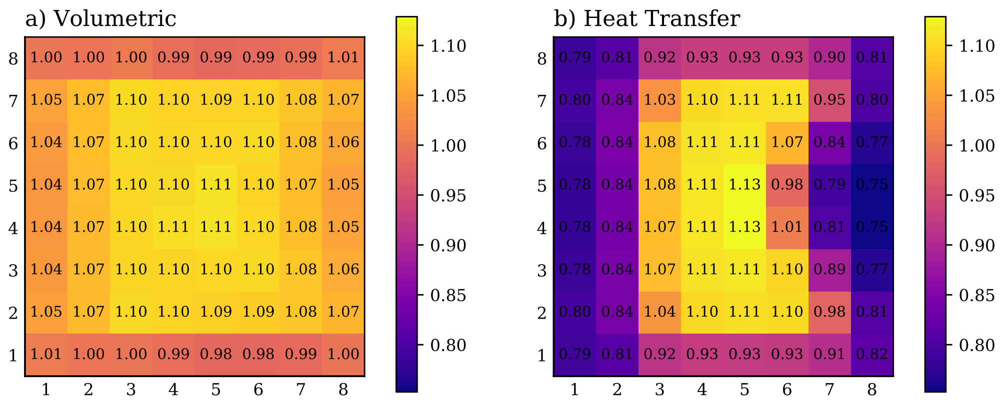

Figure 7.25: Induced Draft System Effectiveness ($U_x = 3$ m/s)

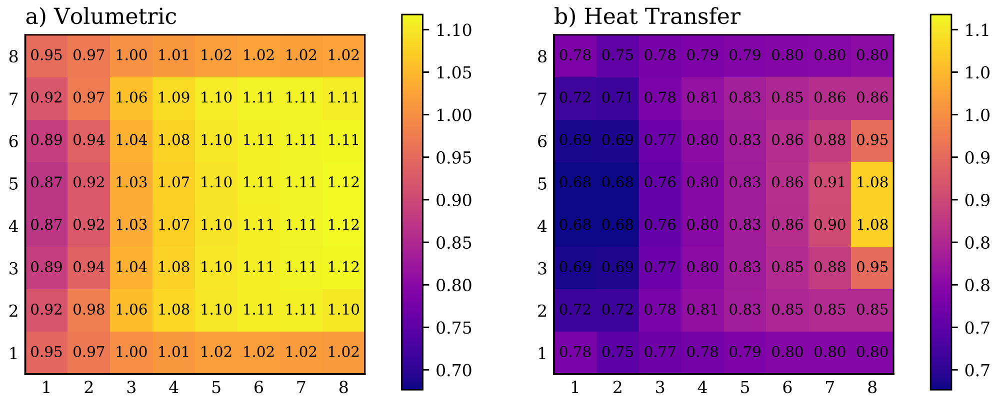

Figure 7.26: Induced Draft System Effectiveness ($U_x = 6$ m/s)

mean volumetric effectiveness decreases from 1.09 by 1.5%, 13.2% and 38.0% respectively. The above-mentioned mean volumetric effectiveness values exclude the front and back fan-units ($j = 1$) and ($j = 8$), as these fan-units have a three-dimensional airflow supply which prevents a fair comparison of their performance.

The decreases in volumetric effectiveness seen at the leading edge fan-units are smaller under secondary crosswind conditions than the decreases seen under primary crosswind conditions. At the fan-units immediately downwind of the leading edge the decreases are closer to those seen under primary crosswind conditions.

At the trailing edge of the ACC the mean volumetric effectiveness of the fan-units decreases by 2.8% under 3 m/s crosswind velocities from 1.09 under normal operating conditions, increases by 2.3% under 6 m/s crosswind velocities and decreases by 2.4% under 9 m/s crosswind velocities.

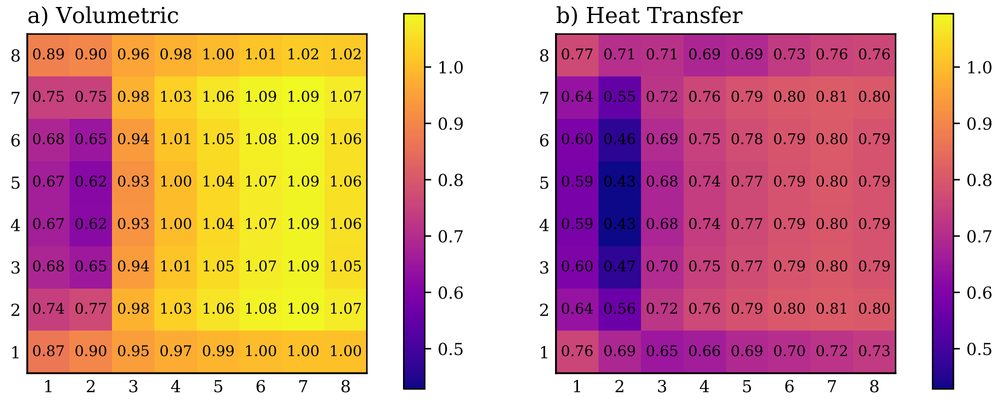

Figure 7.27: Induced Draft System Effectiveness ($U_x = 9$ m/s)

The mean heat transfer effectiveness of the ACC decreases from 1.04 under normal operating conditions by 10.1% under a 3 m/s crosswind, by 22.6% under a 6 m/s crosswind and by 31.3% under a 9 m/s crosswind. At the leading edge fan-units the mean heat transfer effectiveness decreases from 1.00 by 21.1%, 30.5% and 39.1% under crosswinds of 3, 6 and 9 m/s respectively.

The decrease in heat transfer effectiveness immediately downwind of the leading edge is shown to be greater than that seen at the leading edge of the ACC. The decrease in heat transfer effectiveness at the abovementioned fan-units is much greater than that seen for the volumetric effectiveness. This indicates that some flow field phenomena not directly linked to the fan performance of the fan-units in question is responsible for the decrease in heat transfer effectiveness.

Lastly at the fan-units immediately downwind of the leading edge fan-units the mean heat transfer effectiveness decreases from 1.10 by 23.3%, 36.7% and 55.9% under the same crosswind velocities. At the trailing edge of the ACC the mean volumetric effectiveness decreases from 1.00 under normal operating conditions by 22.2%, 3.6% and 20.4% under crosswinds of 3, 6 and 9 m/s respectively.

The asymmetry in heat transfer effectiveness between the front ($j = 1$) and back ($j = 8$) side fan-units under secondary crosswind conditions is an order of magnitude less than the asymmetry seen between the left and right side fan-units under primary crosswind conditions. At crosswind velocities of 9 m/s the front side fan-units have a mean heat transfer effectiveness that is 3.16% less than that seen at the back side fan-units. Under crosswinds velocities of 6 m/s the difference is an order of magnitude less at only 0.56%.

The heat-to-power ratios of the Induced Draft ACC under secondary crosswinds of 3, 6 and 9 m/s are shown in Figs. 7.28 to 7.30.

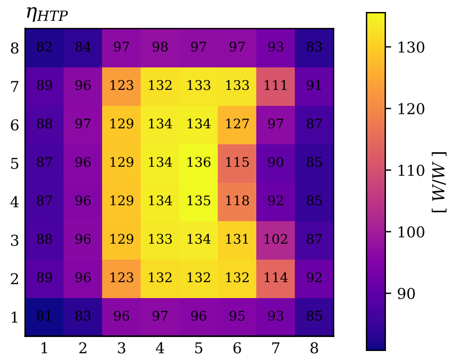

Figure 7.28: Induced Draft Heat-to-Power Ratio ($U_x = 3$ m/s)

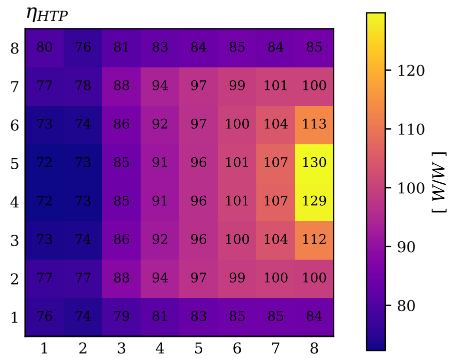

Figure 7.29: Induced Draft Heat-to-Power Ratio ($U_x = 6$ m/s)

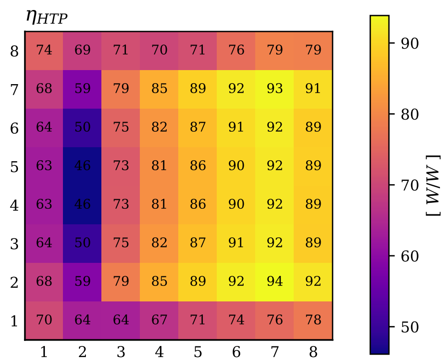

Figure 7.30: Induced Draft Heat-to-Power Ratio ($U_x = 9$ m/s)

The mean heat-to-power ratio of the Induced Draft ACC under secondary crosswind conditions decreases from 120.6 W/W under normal operating conditions to 106.5 W/W under a 3 m/s crosswind, to 90.0 W/W under a 6 m/s crosswind and to 77.6 W/W under a 9 m/s crosswind. The decrease in the mean heat-to-power ratio is greater under all secondary crosswind velocities than the corresponding decrease under similar primary crosswind velocities.

At the leading edge of the ACC the mean heat-to-power ratio of the ACC decreases from 117.2 W/W under normal operating conditions by 24.9%, 36.6% and 44.6% under crosswinds of 3, 6 and 9 m/s respectively. At the fan-units immediately downwind of the leading edge fan-units the mean heat-to-power ratio decreases from 131.1 W/W under normal operating conditions by 26.8%, 43.0% and 60.6% under similar crosswind velocities.

The asymmetry seen in the heat transfer effectiveness is also present in the heat-to-power ratios. Under crosswind velocities of 9 m/s the front side fan-units have a heat-to-power ratio that is 3.67 MW or 3.88% less than that of the back side fan-units. The difference is comparable to that seen in the heat transfer effectiveness results.

Flow Separation

The flow separation at the leading edge of the Induced Draft ACC under secondary crosswinds of 3, 6 and 9 m/s is shown in Figs. 7.31 to 7.33. The flow separation is shown for fan-units $(1, 1)$ and $(1, 4)$ which are respectively located at the side and the centre of the leading edge.

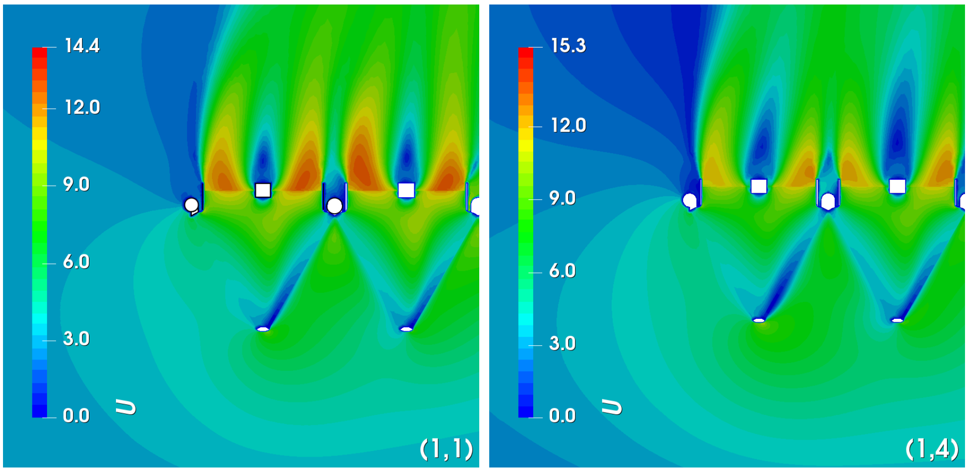

Figure 7.31: Induced Draft Flow Separation ($U_x = 3$ m/s)

The flow separation increases as the crosswind velocity increases. The separation is shown to form behind the V-frame of the leading edge fan-unit where it starts forming at the lower vertex of the V-frame. The flow separation is greater at the centre-located fan-unit $(1, 4)$ where the airflow supply to the fan-units is two-dimensional. The corner located fan-unit $(1, 1)$ is able to draw in air from multiple directions and therefore the flow separation seen is noticeably less.

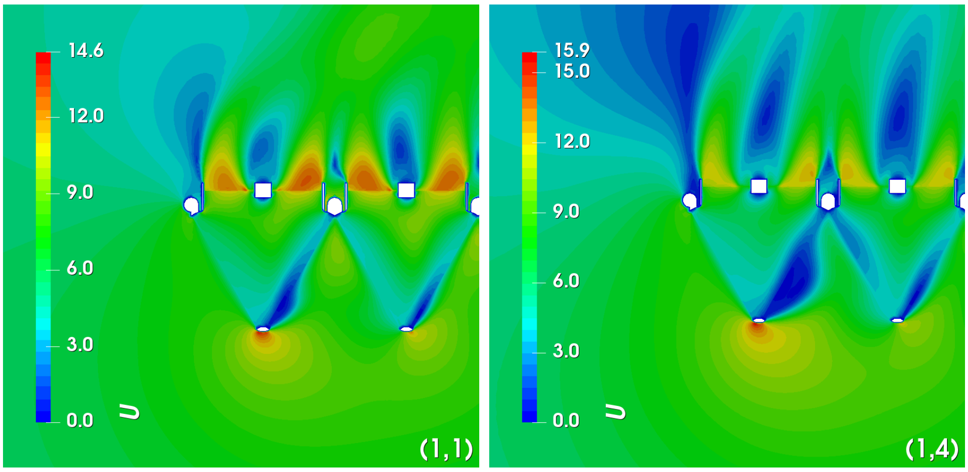

Figure 7.32: Induced Draft Flow Separation ($U_x = 6$ m/s)

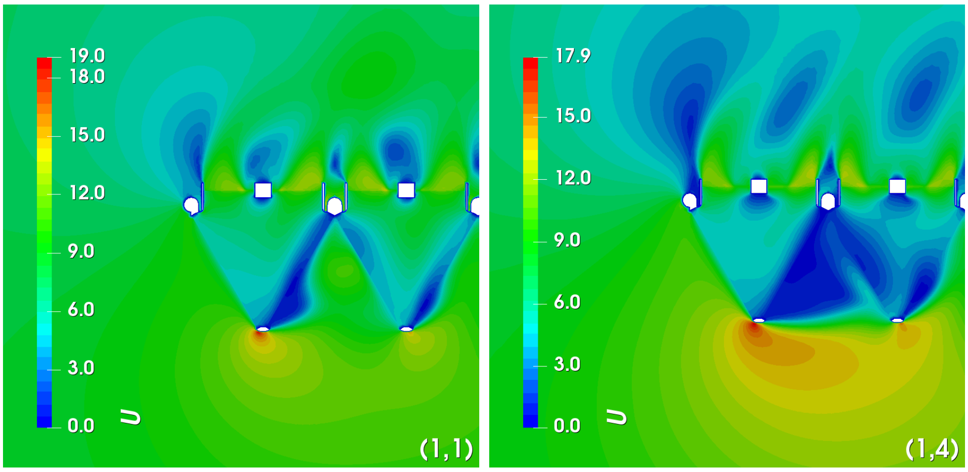

Figure 7.33: Induced Draft Flow Separation ($U_x = 9$ m/s)

At the greater crosswind velocity of 9 m/s the region behind the rear heat exchanger of the first V-frame for fan-unit $(1, 4)$ shows a large region of relatively low velocity magnitude. At crosswind velocities of 6 m/s this region is much smaller and at crosswind velocities of 3 m/s it is negligible.

Heat Exchanger Performance

The total heat transfer rate and mean heat exchanger inlet air temperature for the Induced Draft ACC under secondary crosswind conditions are shown in Figs. 7.34 to 7.36.

The mean heat transfer rate for the Induced Draft ACC under secondary conditions decreased from 19.3063 MW under normal operating conditions by 10.0% under a 3 m/s crosswind, by 22.5% under a 6 m/s crosswind and

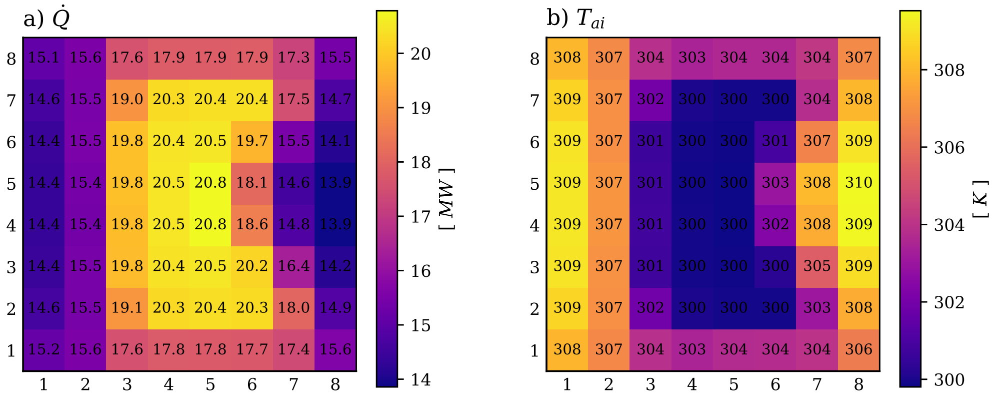

Figure 7.34: Induced Draft Heat Exchanger Performance ($U_x = 3$ m/s)

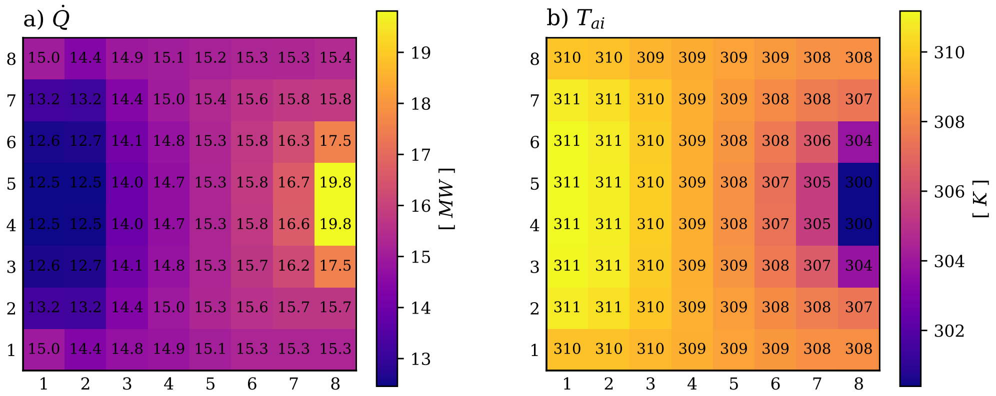

Figure 7.35: Induced Draft Heat Exchanger Performance ($U_x = 6$ m/s)

by 31.2% under under a 9 m/s crosswind. The mean heat exchanger inlet temperatures increased from 301.644 K under normal operating conditions increased to 304.3 K, 308.6 K and 311.7 K respectively.

At the leading edge of the ACC the mean heat transfer rate decreases from 18.4 MW under normal operating conditions by 21.1%, 30.5% and 39.1% under 3, 6 and 9 m/s crosswinds respectively. Immediately downwind of the leading edge fan-units the mean heat transfer rate decreases from 20.2 MW by 23.3%, 36.7% and 55.9% under the same crosswind velocities.

The mean inlet temperatures of the heat exchangers at leading edge fan-units increases from 303.4 K under normal operating conditions to 309.0, 311.0 and 313.0 K under 3, 6 and 9 m/s crosswinds respectively. Immediately downwind of the leading edge-fan-units the mean inlet temperature of the heat exchangers increases from 300.2 K to 307.0 K, 310.8 K and 314.1 K under the same crosswind velocities.

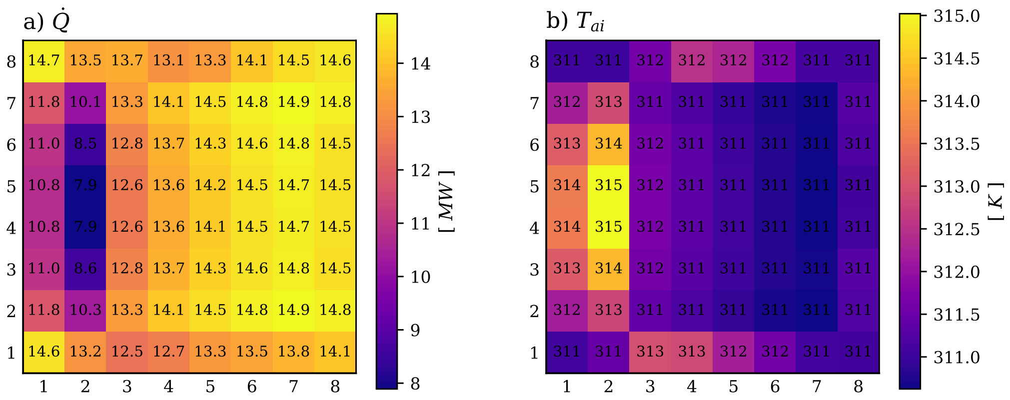

Figure 7.36: Induced Draft Heat Exchanger Performance ($U_x = 9$ m/s)

The decreases in the heat transfer rate is greater immediately downwind of the leading edge than at the leading edge itself, while the increase in inlet temperature is greater immediately downwind of the leading edge. The decrease in heat transfer rate, and similarly the decrease in heat transfer effectiveness, is attributed to the increase in inlet temperatures downwind of the leading edge. This correlates well with the flow separation phenomena seen in Fig. 7.33.

The heat transfer asymmetry seen in the heat transfer rate show that under crosswind velocities of 9 m/s the front ($j = 1$) side fan-units have a heat transfer rate that is 0.56 MW (3.16%) less than that of the back ($j = 8$) side fan-units. Interestingly the heat exchangers' inlet air temperatures do not show a significant asymmetry with a difference of only 0.3 K under the same crosswind velocity.

Hot Plume Recirculation

The flow field recirculation at the sides of the Induced Draft ACC is shown for the 9 m/s crosswind in the secondary direction. The recirculation is shown for both the front ($j = 1$) and back ($j = 8$) side fan-units as contour plots on the yz-plane through the centres of the fan-units located at $i \in 4, 6, 8$. The velocity field recirculation is shown in Figs. 7.37 and 7.38 and the temperature field recirculation is shown in Figs. 7.39 and 7.40.

The velocity contour plots show the vortex formation at the sides of the Induced Draft ACC under secondary crosswind conditions. The vortices are shown to grow larger as they move down the sides of the ACC. The recirculation is shown to be attached at the top of the sides of the ACC where they remain until they detach towards the end of the sides. The recirculation vortex is shown to be larger on the front side of the ACC than on the back side of the ACC.

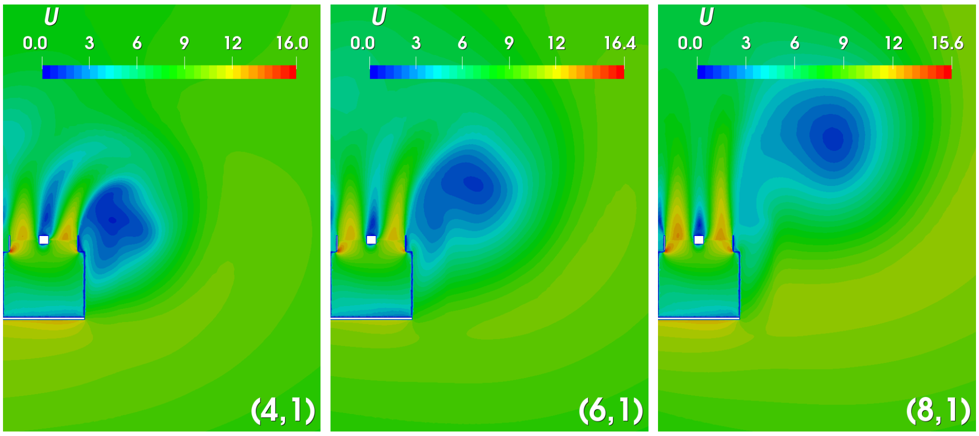

Figure 7.37: Induced Draft Velocity Recirculation ($U_x = 9$ m/s, Front Side)

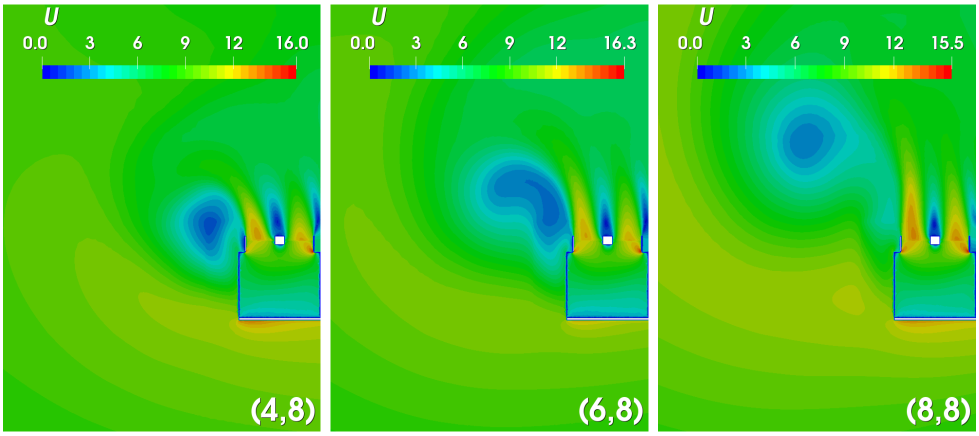

Figure 7.38: Induced Draft Velocity Recirculation ($U_x = 9$ m/s, Back Side)

The temperature contour plots show how the hot air ejected at the top of the fan-units become entrained in the vortices formed at the sides of the ACC. The heated air recirculated through the the fan-units at the sides of the ACC is responsible for the decreased heat transfer rates seen at the sides of the ACC.

The flow field streamlines for the 9 m/s crosswind in the secondary crosswind direction is shown in Fig. 7.41. Similar to what occurs under primary crosswind conditions, the streamlines show the formation of the vortex starting at the corner fan-unit of the leading edge. The vortex grows in sizes as it moves down the side of the ACC as seen in Figs. 7.37 to 7.40. The bottom of the vortex remains at a relatively even height up until just before the last fan-units down the side of the ACC, where-after the vortex starts to detach from the ACC as it moves up and away.

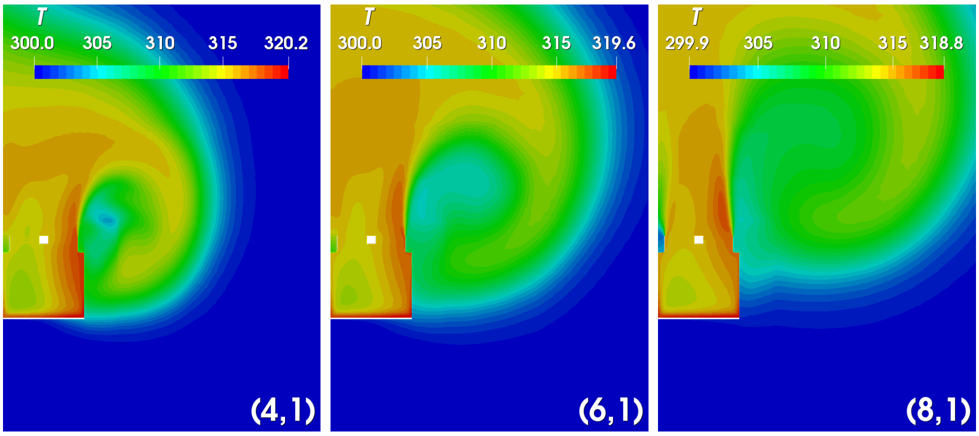

Figure 7.39: Induced Draft Temperature Recirculation ($U_x = 9$ m/s, Front Side)

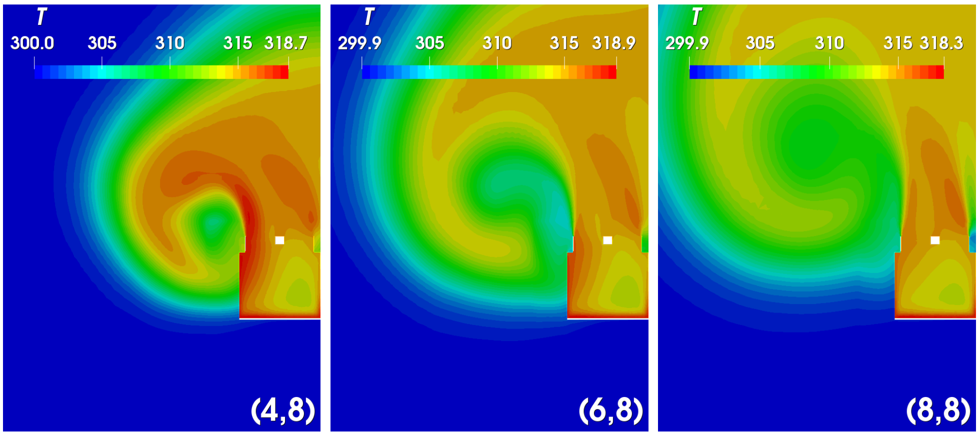

Figure 7.40: Induced Draft Temperature Recirculation ($U_x = 9$ m/s, Back Side)

7.2.4 Comparison of Primary & Secondary Crosswind

An analysis of the Induced Draft ACC results for crosswinds in both primary and secondary directions show how all three of the performance criteria, i.e. volumetric effectiveness, heat transfer effectiveness and heat-to-power ratios, decrease as the crosswind velocity increases. The greatest decreases are seen at the fan-units of leading edge of the ACC, with respect to the crosswind direction followed by decreases at the fan-units immediately downwind of the leading edge fan-units. Overall the performance of the ACC is shown to decrease less under primary crosswind conditions than under secondary crosswind conditions.

Comparisons of the mean volumetric effectiveness, the mean heat transfer effectiveness, the mean heat-to-power ratio and the mean heat exchanger inlet air temperatures for the Induced Draft ACC between primary and secondary crosswind conditions are shown in Figs. 7.42 to 7.45. The figures show com-

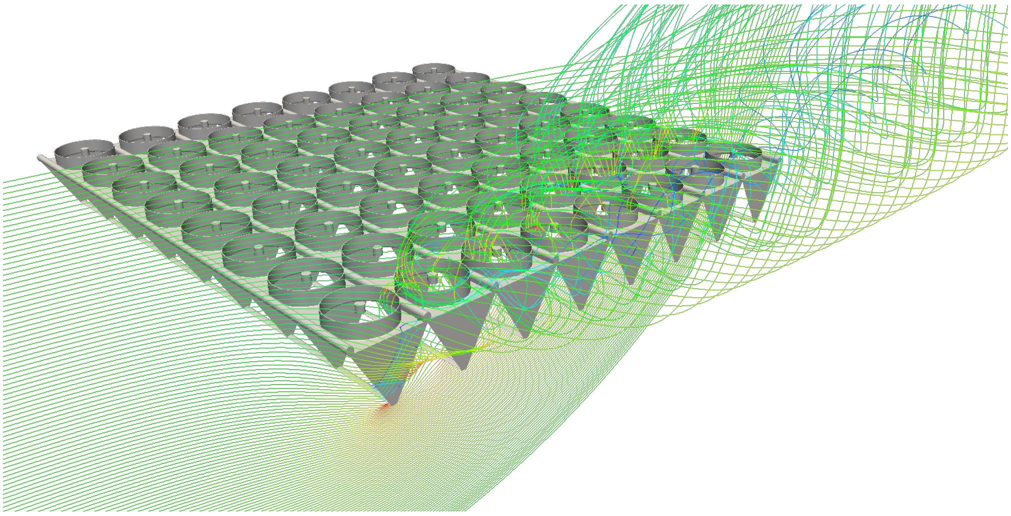

Figure 7.41: Induced Draft Streamlines ($U_y = 9$ m/s)

parisons between results for the entire ACC and for fan-units at the leading edge and immediately downwind of the leading edge.

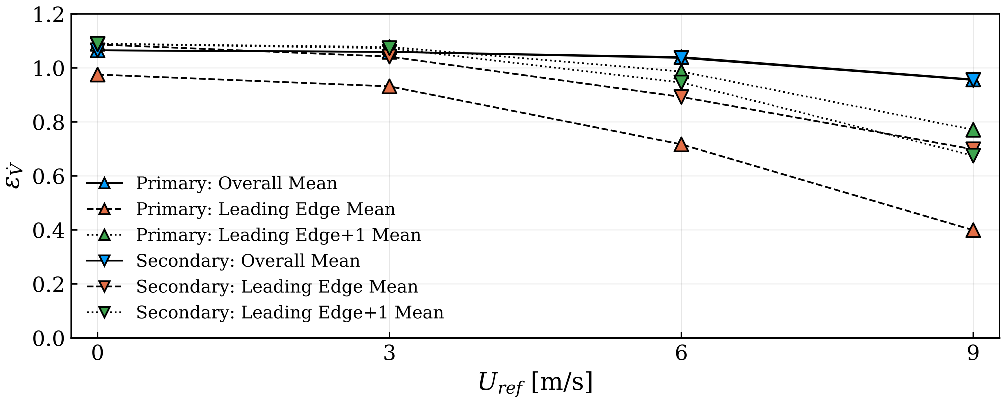

Figure 7.42: Induced Draft Volumetric Effectiveness Comparison

As seen in Fig. 7.42 the decreases in the overall mean volumetric effectiveness of the Induced Draft ACC under both primary and secondary crosswind conditions are almost exactly similar. At the leading edge fan-units of the ACC the mean volumetric effectiveness decreases more under primary crosswind conditions, while at the fan-units immediately downwind of the leading edge the decrease is greater under secondary crosswind conditions. This difference in attributed to the different nature of the flow separation between primary and secondary crosswinds, where under primary crosswinds the airflow is required to move vertically downwards and into the region between the V-frames fan-units in contrast to secondary crosswinds where the air can flow directly into and through the heat exchangers. Additionally the leading edge fan-units under primary crosswind conditions are configured with the L-fan which has higher pressure and power characteristic curves compared to the N-fan which probably allows the fan-units to mitigate the downwind volumetric effectiveness decreases better – albeit at the cost of their own performance.

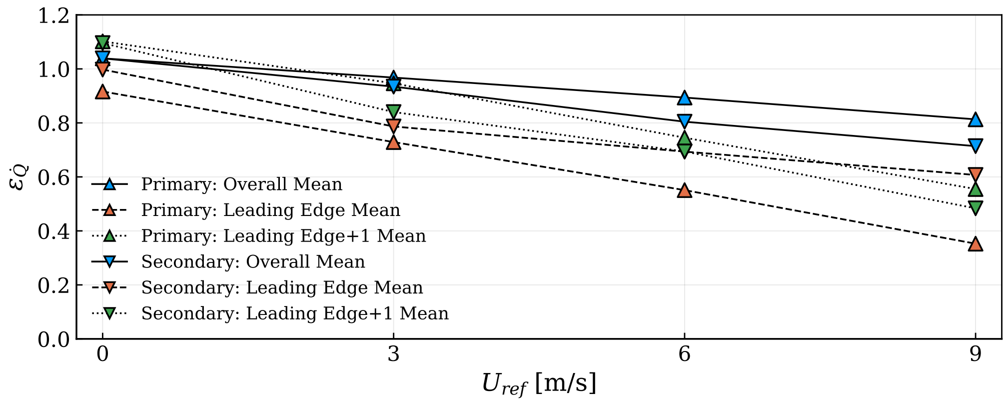

Figure 7.43: Induced Draft Heat Transfer Effectiveness Comparison

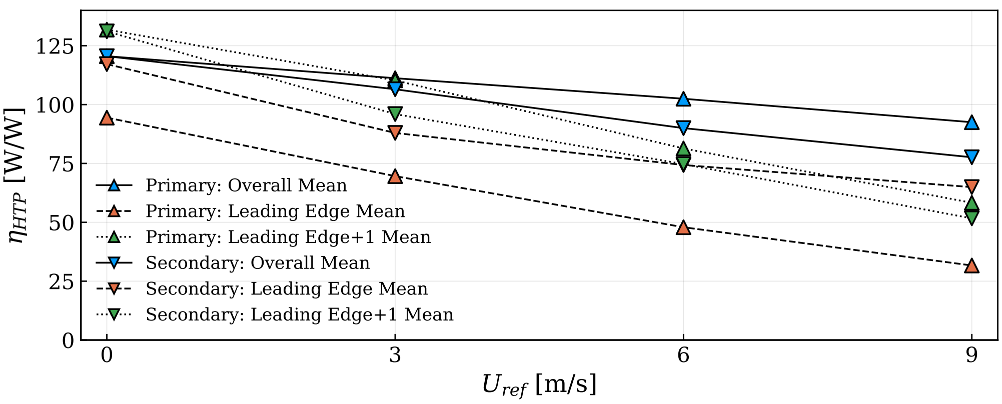

Figure 7.44: Induced Draft System Heat-to-Power Comparison

Comparing the heat transfer effectiveness in Fig. 7.43 and the system heat-to-power ratio in Fig. 7.44 shows very similar trends between the two performance criteria – indeed the correlation between the two sets of results is almost perfectly linear. The high correlation suggests that the changes seen in the heat-to-power ratio are primarily driven by changes in the heat transfer rate rather than changes in the fan power consumption. This is corroborated by the relatively small increases in fan power consumption as the crosswind velocities increase in both primary and secondary crosswind conditions.

The decrease in overall mean heat transfer effectiveness, and similarly the heat-to-power ratio, is greater under secondary crosswind conditions than the decreases under primary crosswind conditions. At the leading edge fan-units of the ACC the decrease is greater under primary crosswind conditions than it is under secondary crosswinds which correlates well with the decrease in volumetric effectiveness discussed earlier. However at the fan-units immediately downwind of the leading edge fan-units the decrease deviates from that seen for the volumetric flow rate as both the heat transfer effectiveness and heat-to-power ratio decrease more under secondary crosswind conditions. The change in the heat transfer is linked to significantly greater heat exchanger inlet air temperatures seen downwind of the leading edge under secondary crosswind conditions as shown in Fig. 7.45.

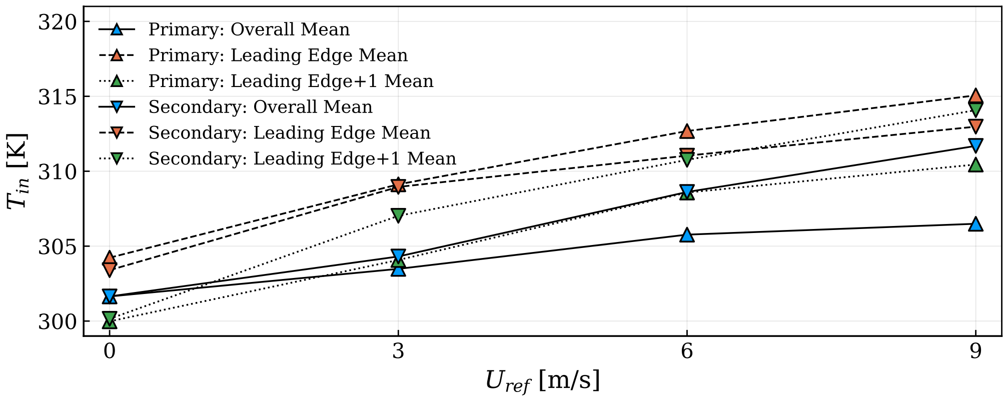

Figure 7.45: Induced Draft Inlet Air Temperatures Comparison

Chapter 8

Forced Draft vs Induced Draft Comparison

8.1 Single Fan Operating Point

The numerical operating points of the two Single Fan ACCs differ. The volumetric flow rates, the fan power consumptions and the heat transfer rates are listed in Tables 8.1 to 8.3. The comparisons are given for both axial flow fans at various fan blade angles, i.e. for the L-fan at 8°, 9° and 10° and for the N-fan at 10°, 11° and 12°.

Table 8.1: Single Fan ACC: Volumetric Flow Rate Comparison ($\dot{V}$)

L-Fan	8.0°	9.0°	10.0°	
Forced Draft	699.25	726.64	753.53	m^3/s
Induced Draft	838.73	884.01	928.79	m^3/s
N-Fan	10.0°	11.0°	12.0°	
Forced Draft	663.29	684.71	705.94	m^3/s
Induced Draft	886.19	924.16	961.74	m^3/s

Comparing the volumetric flow rates through the two Single Fan ACCs shows that the flow rates through the Induced Draft ACC are greater than those through the Forced Draft ACC by 157.4 m^3/s for the L-fan and 239.4 m^3/s for the N-fan. It is noted that due to the heat transfer that occurs the before the axial flow fan in the induced draft design the expected volumetric flow rate is higher due to the lower air density. The Induced Draft ACC's increases in volumetric flow rate per degree of increase in blade angle are also 65.9% greater for the L-fan and 77.1% greater for the N-fan than that seen for the Forced Draft ACC. Besides the difference in flow field density at the axial flow fan the differences in the volumetric flow rates can be attributed to the different geometries of the two ACC designs.

Table 8.2: Single Fan ACC: Fan Power Comparison ($\dot{W}$)

L-Fan	8.0°	9.0°	10.0°	
Forced Draft	159.55	174.97	191.63	kW
Induced Draft	180.15	195.77	212.81	kW

N-Fan	10.0°	11.0°	12.0°	
Forced Draft	139.60	152.29	165.57	kW
Induced Draft	168.12	182.40	197.73	kW

Comparing the fan power consumption of the two Single Fan ACCs shows similar results to that of the volumetric flow rates. The axial flow fans of the Induced Draft ACC are operating at a higher volumetric flow rate and consequently their power consumptions are increased. The Single Fan Induced Draft ACC's fan shaft power consumption is 20.9 kW greater for the L-fan and 30.26 kW greater for the N-fan than that seen in the Forced Draft ACC. The increase in the fans' shaft power consumption per degree of fan blade angle between the two ACCs is neglible for the L-fan with a less than 2% difference, while the increase in the N-fan's power consumption per degree of fan blade angle is greater for the Induced Draft ACC by approximately 14%.

Table 8.3: Single Fan ACC: Heat Transfer Rate Comparison ($\dot{Q}$)

L-Fan	8.0°	9.0°	10.0°	
Forced Draft	16.18	16.68	17.16	MW
Induced Draft	17.49	18.20	18.90	MW

N-Fan	10.0°	11.0°	12.0°	
Forced Draft	15.55	15.94	16.33	MW
Induced Draft	18.24	18.82	19.41	MW

Lastly, comparing the heat transfer rates of the two Single Fan ACCs shows results similar to that of the volumetric flow rates with the Induced Draft ACC outperforming the Forced Draft ACC. The Single Fan Induced Draft ACC achieved 1.5 MW more than the Forced Draft ACC when equipped with the L-fan, and 2.88 MW more when equipped with the N-fan. The increased heat transfer itself is attributed to the increased volumetric flow rates through the fan-units. Similar to the volumetric flow rates, the increase in fan power consumption per degree of increase in blade angle for the Induced Draft ACC is 43.9% and 50.0% greater than that of the Forced Draft ACC for the L-fan and N-fan respectively.

8.2 Axial Flow Fan Performance

A comparison of the overall mean volumetric effectiveness between the Forced Draft and Induced Draft ACCs is shown in Fig. 8.1.

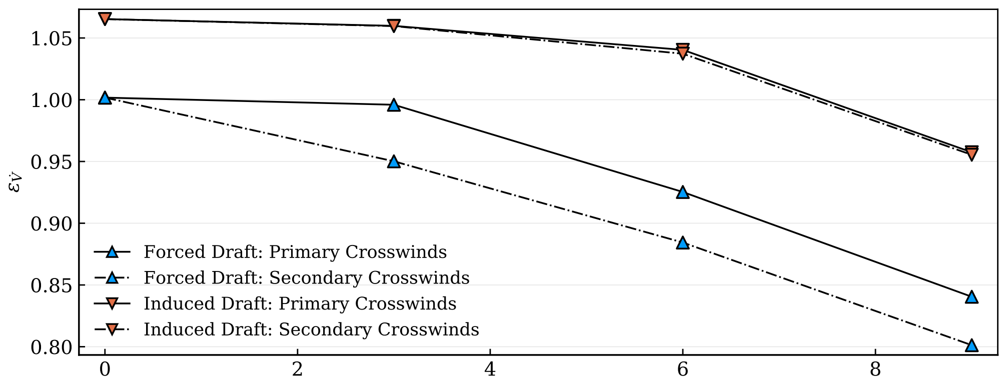

Figure 8.1: Volumetric Effectiveness Comparison: Forced vs Induced Draft

The overall mean volumetric effectiveness of the Induced Draft ACC is consistently higher than that of the Forced Draft ACC. The Induced Draft ACC's mean volumetric effectiveness is similar under both crosswind conditions, and the reduction over the range of crosswind conditions is less than that of the Forced Draft ACC. The Forced Draft ACC is shown to perform marginally better under primary crosswinds than under secondary crosswinds, however the decrease in the mean volumetric effectiveness is still larger than that seen for the Induced Draft.

A detailed comparison of the mean volumetric effectiveness of the Forced Draft and Induced Draft ACCs is shown in Fig. 8.2. The detailed comparison shows the mean volumetric effectiveness for each row under primary crosswinds and each street under secondary crosswinds, i.e. equivalent downwind fan-units perpendicular to the crosswind direction.

For both ACCs, and both crosswind directions, the effect of the crosswinds is concentrated at the leading edge fan-units, and the fan-units immediately downwind of the leading edge. From the 3$^{\text{rd}}$ row under primary crosswinds, and 3$^{\text{rd}}$ street under secondary crosswinds, and downwind thereof the mean volumetric performance of the two ACCs remains relatively consistent.

The Forced Draft ACC exihibited assymetry in the volumetric effectiveness of the fan-units located at the sides of the ACC parallel to the crosswind direction under both primary and secondary crosswind conditions. In contrast the Induced Draft ACC did not exhibit any real asymmetry in the volumetric effectiveness. The difference is attributed to the location of the fans in the

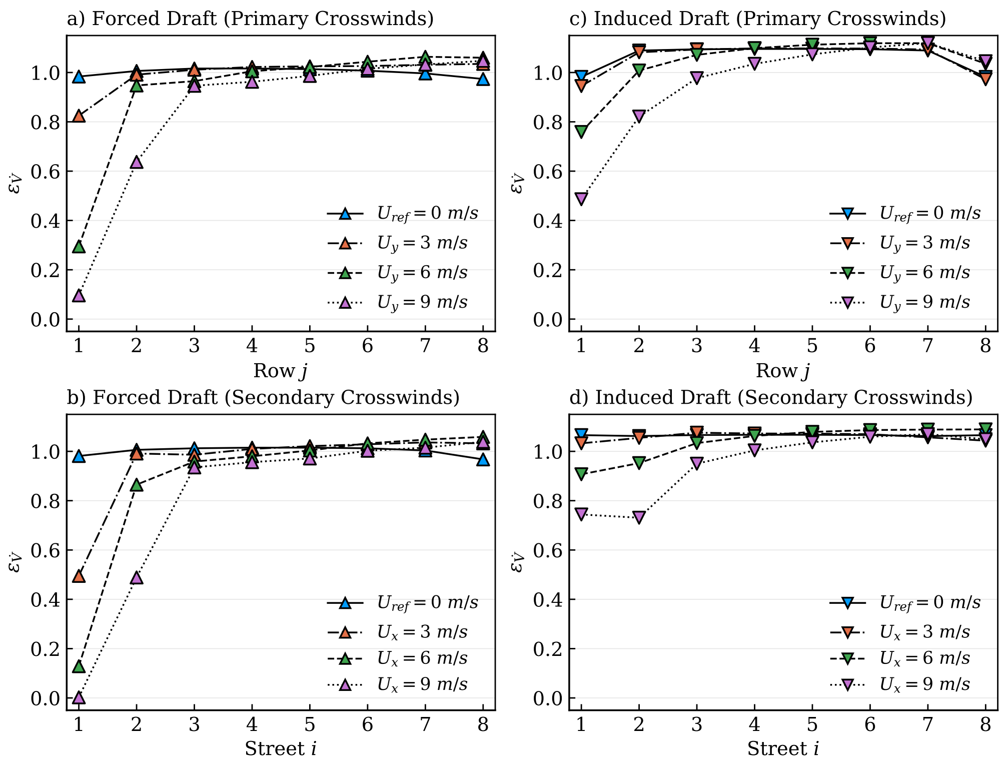

Figure 8.2: Volumetric Effectiveness Comparison: Forced vs Induced Draft

Induced Draft Design where their location downstream of the heat exchangers makes them less susceptible to crosswinds at their inlet, i.e. different relative velocities due to the fans rotation at the sides of the ACC affecting the fan performance.

Due to the different geometries of the Forced Draft and Induced Draft ACCs the nature of flow separation at the leading edges of the ACC differs. For the Forced Draft ACC which was equipped with windwalls the flow separation is relatively independent of the crosswind directions after accounting for the effects of the axial flow fan used to equip the leading edge fan-units. The flow separation here occurs as the high velocity flow moves past the bellmouth inlet of the Forced Draft ACC. In contrast the nature of the flow separation differs for the Induced Draft ACC which has no windwalls. Under primary crosswind conditions the flow separates as it is required to move down and inbetween the V-frames of the Induced Draft ACC, and while under secondary crosswinds the flow impinges directly on the leading edge's heat exchanger bundles and separates behind the nadir of the V-frame. The difference in fan-unit geometry is the primary cause of the Induced Draft ACC superior volumetric effectiveness at the leading edge as the flow separation does not directly affect the axial flow fan in the same manner as seen for the Forced Draft ACC.

8.3 Heat Exchanger Performance

A comparison of the overall mean heat transfer effectiveness between the Forced Draft and Induced Draft ACCs is shown in Fig. 8.3. The overall mean heat transfer effectiveness results shown are different to that of the overall mean volumetric effectiveness shown previously in Fig. 8.1

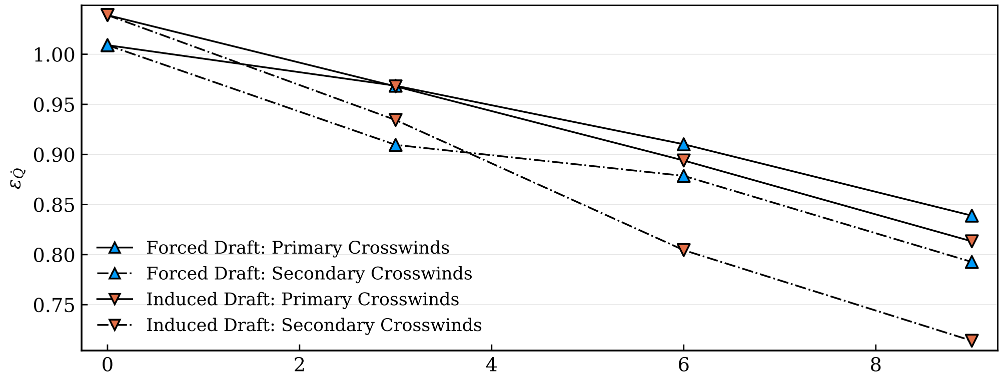

Figure 8.3: Heat Transfer Effectiveness Comparison: Forced vs Induced Draft

Under normal operating conditions and low crosswind velocities of 3 m/s the overall mean heat transfer effectiveness of the Induced Draft ACC is higher than, or at least comparible to, that of the Forced Draft ACC. At primary crosswinds of 6 and 9 m/s the overall mean heat transfer effectiveness of Forced Draft ACC is higher than that of the Induced Draft ACC, and similarly also under secondary crosswinds of 6 and 9 m/s. The overall mean heat transfer effectiveness of the Induced Draft ACC under primary crosswinds of 6 and 9 m/s is higher than that of the Forced Draft ACC under secondary crosswinds of similar magnitudes.

A detailed comparison of the mean heat transfer effectiveness of the Forced Draft and Induced Draft ACCs are shown in Fig. 8.4. Similar to volumetric effectiveness shown in Fig. 8.2 the mean heat transfer effectiveness results are shown for each row and street respectively for primary and secondary crosswinds.

For the Forced Draft ACC the decrease in heat transfer effectiveness correlates relatively well with that of the volumetric effectiveness. In contrast the decrease in heat transfer effectiveness seen in for the Induced Draft ACC start to deviate significantly from that of the volumetric effectiveness, with the deviation increasing as the crosswind velocity increases. This suggests that for the Forced Draft ACC the reduction in the axial flow fan's performance as measured by the volumetric effectiveness is the driving factor behind the reduced heat exchanger performance as measured by the volumetric effectiveness. The

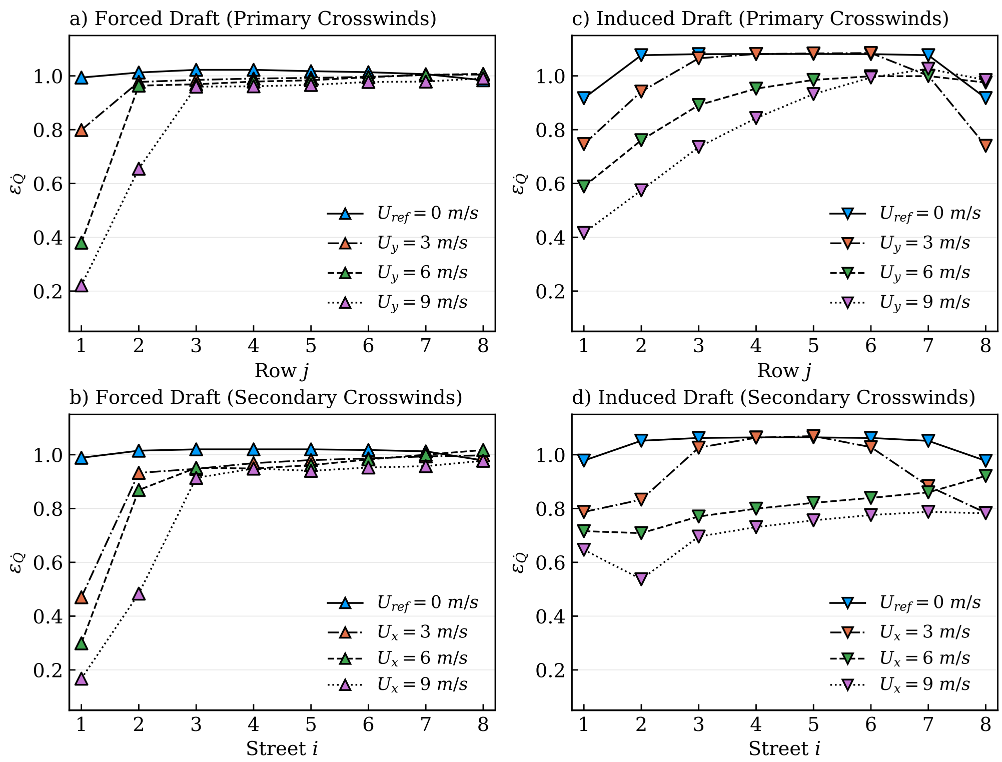

Figure 8.4: Heat Transfer Effectiveness Comparison: Forced vs Induced Draft

decrease in heat transfer effectiveness is shown to be much more significant under secondary crosswind conditions, and is much more prevalent for the Induced Draft ACC.

The differences in heat transfer effectiveness between the two ACCs is attributed to increased heat exchanger inlet air temperatures. A comparison of the overall mean heat exchanger inlet air temperatures between the two ACCs is shown in Fig. 8.5.

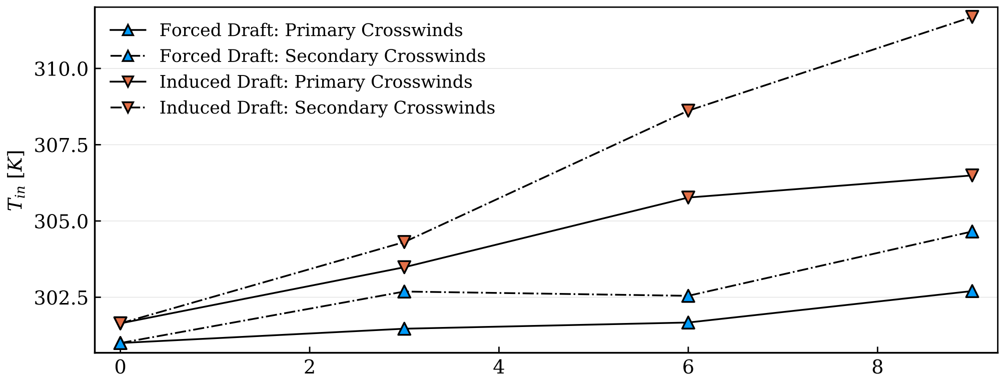

Figure 8.5: Inlet Air Temperatures Comparison: Forced vs Induced Draft

The increases in the overall mean heat exchanger inlet air temperatures are larger for the Induced Draft ACC than the increases are for the Forced Draft ACC. Additionally the difference between the increases in the mean heat exchanger inlet air temperatures between primary and secondary crosswind conditions is also larger for the Induced Draft ACC. Both Induced Draft and Forced Draft ACC show larger increases in mean heat exchanger inlet air temperature under secondary crosswind conditions.

A detailed comparison of the mean heat exchanger inlet air temperatures between the Forced Draft and Induced Draft ACCs are shown in Fig. 8.6. Similar to volumetric effectiveness and heat transfer effectiveness shown in Figs. 8.2 and 8.4 respectively, the mean heat exchanger inlet air temperatures are shown for each row and street respectively for primary and secondary crosswinds.

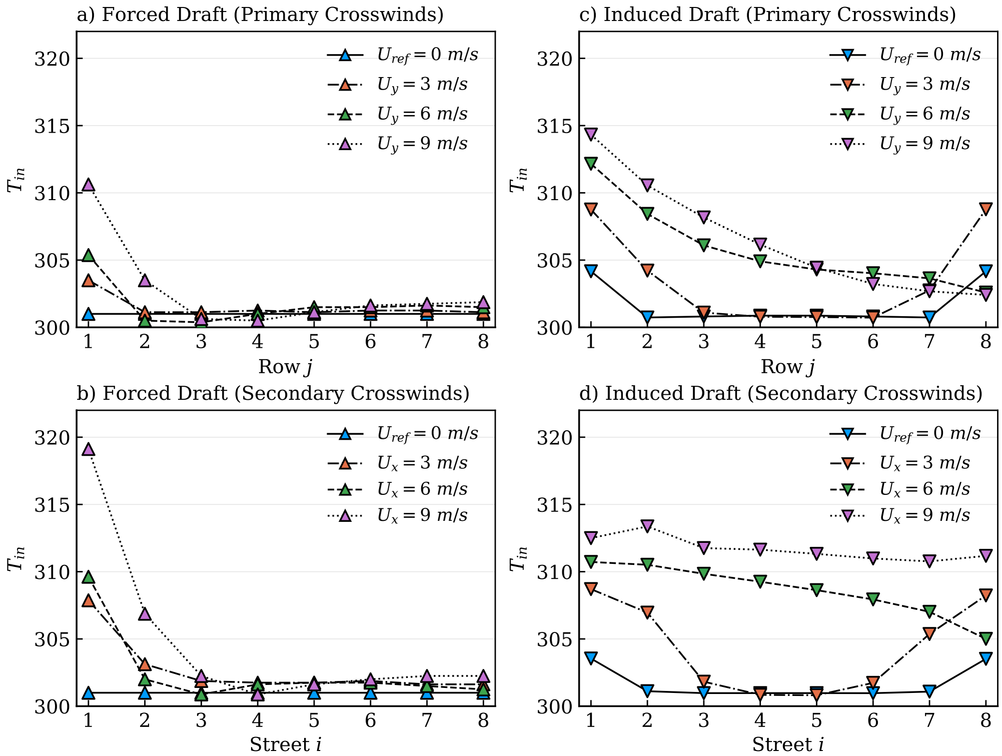

Figure 8.6: Inlet Air Temperatures Comparison: Forced vs Induced Draft

The increased heat exchanger inlet air temperatures is shown to be concentrated at the leading edges of the two ACC, regardless of crosswind direction For the Forced Draft ACC the mean inlet air temperatures are relatively unaffected from the 3rd fan-unit row/street downwind of the leading edge and on. In contrast under crosswinds velocities of 6 and 9 m/s all the fan-units of the Induced Draft ACC are shown to have increased mean heat exchanger inlet air temperatures. The increased mean heat exchanger inlet air temperatures of the Induced Draft ACC matches very well with the decreased heat transfer effectiveness shown previously in Fig. 8.4.

The effect of the two ACC's fan-unit geometry on flow separation directly affects the heat exchanger inlet air temperatures by transporting heated air from upwind fan-units towards the downwind heat exchangers. The Induced Draft ACC is also by design more susceptible to increased heat exchanger inlet air temperatures due to the axial flow fan being located behind the heat exchangers allowing any reverse flow through the heat exchangers to directly affect the downwind heat exchangers. Any reverse flow through the Forced Draft ACC is trapped within the plenum of the fan-unit, unless there is net negative flow through the fan-unit, and does not affect the downwind fan-unit's heat exchanger inlet air temperatures.

Similar to the volumetric effectiveness an asymmetry is seen in the heat transfer effectiveness and heat exchanger inlet air temperatures at the sides of the ACC. The heat transfer effectiveness of the fan-units at the sides of the ACC is shown to differ asymmetrically for both the Forced Draft and Induced Draft ACC, although difference in effectiveness of the Induced Draft ACC under secondary crosswind directions is relatively minimal. Regarding heat exchanger inlet air temperatures only the Induced Draft ACC exhibits an assymetry at the sides of the ACC and only under primary crosswind directions where the heat exchagners at the sides of the ACC are directly open to hot plume recirculation. The asymmetry in the results is attributed to the rotational flow field induced by the axial flow fans and their interaction with the air at the axial flow fan's inlet for the Forced Draft ACC and their interaction with the hot plume recirculation vortices for the Induced Draft ACC.

8.4 Heat-to-Power Ratio

A comparison of the overall mean heat-to-power ratios between the Forced Draft and Induced Draft ACCs is shown in Fig. 8.7.

The highest overall mean heat-to-power ratios are seen for the Induced Draft ACC under primary crosswind conditions. In contrast the overall mean heat-to-power ratios of Induced Draft ACC under secondary crosswinds of 6 and 9 m/s are smaller than those of the the Forced Draft ACC under both primary and secondary crosswind of similar magnitudes. The Forced Draft ACC's mean heat-to-power ratios are marginally higher under primary crosswind conditions than they are under secondary crosswind conditions. The decrease in heat-to-power ratios as the crosswind velocity increases is larger for the Induced Draft ACC than it is for the Forced Draft ACC, and the difference between the heat-to-power ratios under the two different crosswind directions is also larger.

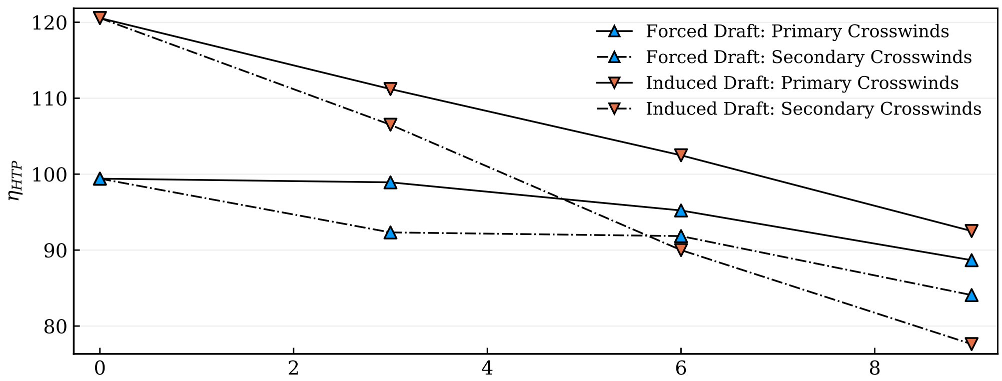

Figure 8.7: System Heat-to-Power Ratio Comparison: Forced vs Induced Draft

A detailed comparison of the fan-unit heat-to-power ratios of the two ACCs is shown in Fig. 8.8. The mean heat-to-power ratios are shown for the each row and street of the ACC under primary and secondary crosswinds respectively.

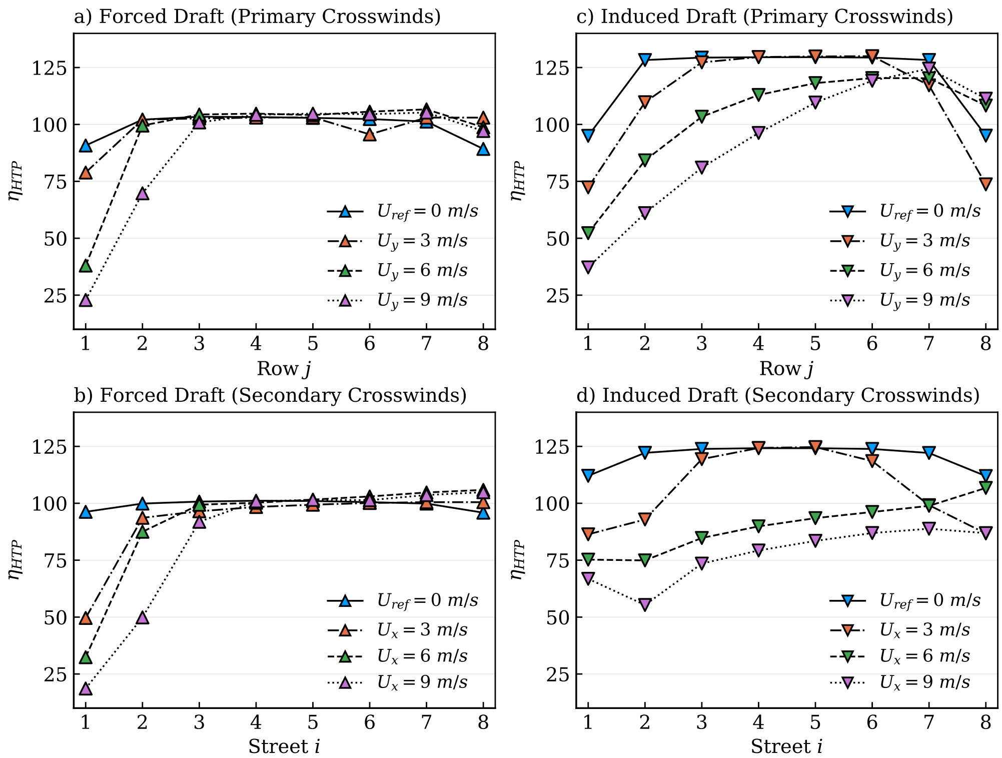

Figure 8.8: System Heat-to-Power Ratio Comparison: Forced vs Induced Draft

The decrease in mean heat-to-power ratios is concentrated at the leading edge of the ACC. The mean heat-to-power ratios of the Forced Draft ACC remain relatively constant from the 3rd row/street and on. In contrast the decreases in the mean heat-to-power ratios of the Induced Draft ACC are distributed over many more rows/streets of the ACC. The largest decreases in the Induced Draft ACC's mean heat-to-power ratios is shown at the leading edge under primary crosswind conditions with consecutively smaller decreases futher downwind of the leading edge. However, under secondary crosswinds of 6 and 9 m/s the decreases in the Induced Draft mean heat-to-power ratios are more uniformly distributed over the entire ACC with even the fan-units far from the leading edge showing relatively low heat-to-power ratios.

Chapter 9

Conclusions

9.1 Numerical Modeling Strategy

The two ACC models developed in this study each consisted of multiple separate numerical models each of which were required to accurately represent the specific components they modeled. To this end the axial flow fan model, the heat exchanger model and a single fan-unit ACC model were validated against experimental and analytical results.

9.1.1 Axial Flow Fan Modeling Strategy

Two actuator disk models were developed for use in this study, namely an incompressible flow implementation for use in the Forced Draft ACC model and a compressible flow implementation for use in the Induced Draft ACC model. The incompressible flow implentation was sufficient for the Forced Draft ACC while the compressible flow implentation was required for the Induced Draft ACC due to its heat exchangers being located before the axial flow fan. For both ACC models, the ADM was used to model two different axial flow fans, the L-fan and the N-fan, which were used to configure the ACCs.

Both implementations of the actuator disk model were validated successfully against experimental fan performance characteristics of the two fans in a BS 848 Type A Facility. Both implementations were able to accurately model the pressure characteristics of the two axial flow fans at their respective operating points. At low volumetric flow rates, i.e. well below the operating point, the ADM under-predicted the fans' static pressure rises, which is a known shortcoming of the ADM.

The actuator disk model, unlike other simplified fan models, can directly determine the shaft power of the fan it is modeling. Both ADM implementations accurately modeled the fan power characteristic of both fans used in this study.

The numerical results correlated very well with the experimental data near the operating points of the two fans. The ADM's numerical power characteristics do not suffer the same deviation from experimental results as seen for the pressure characteristics.

Fan efficiency is a function of the fan's volumetric flow rate, static pressure rise and power. Therefore the fan efficiency as determined using the ADM shows its dependence on the above-mentioned pressure and power characteristics. At the volumetric flow rate near the operating point, the ADM was able to determine the fan efficiency accurately for both fans. At low volumetric flow rates, the fan efficiencies were under-predicted due to the fans under-predicted pressure characteristic.

No significant differences were noticed between the compressible flow and incompressible flow actuator disk model implementations. However it can be noted that the incompressible flow implementation requires greater care to be taken regarding the boundary conditions setup in the numerical model due to the increased complexity of incompressible flow simulations.

9.1.2 Heat Exchanger Modeling Strategy

Two separate models were used to represent the the two ACCs' heat exchangers modeled in this study. The two models were respectively responsible for modeling the pressure drop over the heat exchanger and for modeling the heat transfer rate to the air flowing through the heat exchangers. Each model was validated against experimental results previously obtained in a experimental tunnel.

The Darcy-Forchheimer porosity model was used to model the pressure drop over the heat exchanger. The porosity model was able to very accurately model the pressure drop characteristic of the heat exchanger at all volumetric flow rates tested. The porosity model was additionally capable of correctly modeling the flow turning at the inlet of the heat exchangers. The Darcy-Forchheimer porosity model correlated slightly better when used in the incompressible flow simulations, due to the model's coefficients being defined using a constant reference density.

The Effectiveness Number of Transfer Units (ε-NTU) method was used to determine heat transfer rate. The ε-NTU method was implemented for both incompressible flow and compressible flow as respectively required for the Forced Draft and Induced Draft ACC models. Both ε-NTU method implementations' numerical heat transfer correlated well with that of the experimental results of the heat exchangers. The incompressible flow implementation correlated slightly better overall, only under-predicting slightly at very low volumetric flow rates and over-predicting at higher flow rates. The compressible flow implementation correlated even better at low volumetric flow rates, however at higher volumetric flow rates the model over-predicted the heat transfer much more than the incompressible flow modle did. It is noted that both implementations are sufficiently close to the experimental resutls at the lower volumetric flow rates near the expected operating point of the heat exchanges when they are installed in their respective ACC.

9.2 Forced Draft vs Induced Draft ACC Performance

The performance of the 64-fan Forced Draft ACC and the 64-fan Induced Draft ACC were investigated under various crosswind conditions. Two major phenomena were found te be responsible for decreases in the ACCs' overall performance as under crosswind conditions; namely reduced axial flow fan performance, and increased heat exchanger inlet air temperatures. For the Forced Draft ACC the primary cause of the ACC's decreased performance was identified as reduced axial flow fan performance, while increased heat exchanger inlet air temperatures were identified as a secondary cause. In contrast for the Induced Draft ACC the relation is reversed with increased heat exchanger inlet air temperatures identified as the primary cause of the ACC's reduced performance, with the reduced axial flow fan performance identified as a secondary cause.

For both the Forced Draft and Induced Draft ACC designs the volumetric effectiveness correlates with the heat transfer effectiveness. In the case of the Forced Draft ACC the correlation is very high with a near direct mapping from the volumetric effectiveness to the heat tranfer effectiveness. In contrast for the Induced Draft design the volumetric and heat transfer effectiveness start to diverge as crosswind velocity increases. This correlation suggests that for the Forced Draft ACC design the axial flow fan performance is the primary factor governing the overall ACC performance. For the Induced Draft design, while the axial flow fan performance remains important, the deviation between the two effectivenesses suggests that other flow field phenomena have become more influential, i.e. heat exchanger inlet air temperatures. A direct comparison of the results shows that the axial flow fans of the Forced Draft ACC design are much more susceptible to crosswinds than those of an Induced Draft ACC design.

One of the major differences between the two ACCs is that Forced Draft ACC investigated was equipped with windwalls while the Induced Draft ACC was not. One of the effects that the windwalls have on the Forced Draft ACC is that the ACC is relatively agnostic to which direction the crosswind is coming from due to the similar cross-sectional profiles, and thus the effect of the leading edge fan configuration is emphasized. The Induced Draft ACC in contrast has exposed heat exchangers on one side, and also different cross-sectional profiles, which makes the system inherently more sensitive to crosswind direction, and thus the effect of the leading edge fan configuration is de-emphasized.

The fan performance of the leading edge fan-units of both the Forced Draft and Induced Draft designs was found to decrease significantly as the crosswind velocity increased. For the Forced Draft design the increased crosswind velocity results in flow separation at the bellmouth inlets of the leading edge fan-unit which restricts the flow through the fan-unit. For the Induced Draft design the flow separation occurs differently – under primary crosswind conditions the flow separation occurs as the air is required to flow downwards past the V-frame side walls into the channels between the fan-units, while under secondary crosswind conditions the flow separation is found behind the V-frame's nadir. The flow separation creates a low pressure region that increase the pressure rise that the axial flow fan must overcome, thereby decreasing the volumetric flow rate through the fan-unit. Additionally for the Forced Draft ACC the flow separation results in oblique inflow angles that further reduce the axial flow fans' performance, while for Induced Draft systems the oblique inflow angles creates turning losses where the flow enters the heat exchangers. The flow separation was found to have a greater effect on the axial flow fans of the Forced Draft ACC than those of the Induced Draft ACC.

The volumetric effectiveness results for the Forced Draft ACCs fan configuration shows how the fan configuration affects the ACC's performance when subjected to crosswinds. The L-fan with its steeper pressure characteristic curve was found to mitigate the effect of flow separation at the leading edge better than the N-fan. Consequently the heat transfer effectiveness of the leading edge fan-units was also found to decrease less as crosswinds increased when the L-fan was used. The leading edge fan-unit of the Induced Draft ACC performed worse under primary crosswind conditions when the L-fan was located at the leading edge. However, the performance of the fan-units immediately downwind of the leading edge was better under primary crosswind conditions which suggests that the leading edge fan configuration was able to mitigate the adverse affects that flow separation has on fan-units downwind of the leading edge.

The increase in heat exchanger inlet air temperatures at the leading edge fan-units, and downwind thereof, is seen to increase under crosswinds for both the Forced Draft and Induced Draft ACC. The increase is greater for the Induced Draft ACC than it is for the Forced Draft ACC with the difference attributed to the designs of the two ACCs. The nature of the flow separtion for the Forced Draft ACC affects the axial flow fans directly, and thus only the heat exchangers indirectly. In contrast the flow separation seen for the Induced Draft ACC directly affects the heat exchangers, and due to the lack of windwalls, affects them differently depending on the crosswind direction. The Induced Draft ACC is also more susceptible to increased heat exchanger inlet air temperatures further downwind of the leading edge than the Forced Draft ACC.

Hot plume recirculation was identified for both ACCs, however the effect on the heat exchanger inlet temperatures is less than the more direct effects of flow separation and reverse flow at the leading edge fan-units. Due to the lack of windwalls the Induced Draft ACC showed the greatest susceptibility to hot plume recirculation, especially under secondary crosswind when the heat exchangers were directly open to the recirculation vortices. In contrast the hot plume reciruclation seen for the Forced Draft ACC was relatively agnostic to the crosswind direction.

The heat-to-power ratios of the Induced Draft ACC under normal operating conditions was significantly higher than those of the Forced Draft ACC. The Induced Draft ACC's heat to-power ratios decreased the more than those of the Forced Draft ACC as the crosswind velocity increased, and the divergence between the heat-to-power ratios under primary and secondary crosswinds was also larger than that of the Forced Draft ACC. At higher crosswind velocities in the primary crosswind direction the Induced Draft ACC's heat-to-power ratios were higher than those of the Forced Draft ACC under both primary and secondary crosswinds. However, the Induced Draft ACC's heat to-power ratios under high crosswind velocities in the secondary direction were lower than those of the Forced Draft ACC under both the primary and secondary crosswinds.

The overall performance of the Induced Draft ACC was better under normal operating conditions and low velocity crosswinds, while at higher crosswind velocities the comparison is dependent on the specific performance criteria and the crosswind direction. The Forced Draft ACC's leading edge fan-unit axial flow fan and heat exchagner performance was consistently worse than that of the Induced Draft ACC. The Induced Draft ACC's overall axial flow fan performance was consitently and significantly better than that of the Forced Draft ACC, but its overall heat exchanger performance was affected more directly by crosswinds than the Forced Draft ACC's heat exchanger were. The Induced Draft ACC was shown to be fundamentally more susceptible to the crosswind direction than the Forced Draft ACC.

9.3 Future Work

Direct Correlations between Fan Characteristics and Reduced Fan Performance.

This study, and previous studies before it, have focused primarily on comparing results between different fans. Finding a direct correlation between fan characteristic and the reduced fan performance observed under crosswind conditions should be attempted. The reduction in fan performance is dependent on the fan's location in the ACC, and therefore modeling an ACC of sufficient size is necessary to capture the various operating conditions that the fan will operate at. The numerical model used in this study can be used to simulate such an ACC and investigate much more direct correlations between fan characteristics and reduced performance.

Quantification of Hot Plume Recirculation

The effect of hot plume recirculation has not yet been sufficiently investigated and quantified. Any attempt to do such a flow analysis would need to isolate the effects of flow-separation that occurs at the sides of the ACC with the effects of hot plume recirculation. The size of the hot plume recirculation would need te be determined in a useful manner, and the effect of the recirculation on the ACC's overall performance quantified. Identifying where and how the hot plume forms could help with the design of mitigation methods should the effect of the recirculation be sufficiently large.

Extend Draft Equation to Multiple Fan ACCs

The current formulation of the draft equation is limited to a single fan-unit ACC. The draft equation needs to include the flow field phenomena that are present in a multiple fan-unit ACC if it is to be used in the analysis of such an ACC. The numerical model used in this study can be used to quantify the above-mentioned phenomena.

Investigation and Development of a Fan Control System

Currently the axial flow fans installed in ACC systems are configured with a fixed blade angle, and run at a fixed speed. Mitigation of adverse crosswinds has been attempted by configuring the ACC's periphery fan-units with high volumetric flow rate, high power axial flow fans. This strategy unfortunately increases the ACC's fan power consumption during normal operating conditions when no crosswinds are present due to the higher power requirement of the periphery fan-units. Due to the ability of the ADM to effectively calculate the fan's performance under crosswind accurately as well as the fan's shaft power consumption, enough information should be available to investigate and develop a control system that would control the fan blade angle and/or the fan's rotational speed to optimise the fan-unit performance both when the system is under normal operating conditions and when subject to adverse crosswind.

Investigation of Crosswind Mitigation Systems for Induced Draft ACCs

The Induced Draft ACC suffered from radically decreased performance under certain crosswind direction due to the nature of its V-frame design. Windwalls, and other potential crosswind mitigation systems, could be used to improve the performance of V-frame Induced Draft ACC. The nature of the V-frame Induced Draft design would require a different approach to the design of such systems than those taken for A-frame Forced Draft designs, i.e. windwalls for Forced Draft ACCs specifically prevent air from impeding on the outlet of the heat exchangers, but would not do so for Induced Draft ACC.

Appendices

Appendix A

System Specifications

A.1 Fan Specification

Two commercial fans are used in this study, which are labeled as the L-fan and N-fan. The specifications of the fans are given below in Table A.1.

Table A.1: Fan Specifications

Dimension	Symbol	L-fan	N-fan	
Number of Blades	n_f	8	9	#
Diameter	D_f	10.370	10.370	m
Blade Chord Length	c_f	1.254	0.728	m
Hub-to-tip Ratio	D_f/D_h	0.135	0.135	m/m
Tip Clearance		0.025	0.025	m

The airfoil profiles of the N-fan and L-fan are not freely available. Augustyn (2013) determined the geometry of these fans using a combination of non-contact and contact 3D scanning. The only available 3D representations of the fan geometries were contained inside the meshes of `ANSYS Fluent`® case files from Augustyn's study, from which the coordinate points on the blade surfaces were extracted. The extracted fan airfoil profiles at various radii are shown in Figs. 4.1 and 4.2 in § 4.1.1.

A.2 Heat Exchanger Specification

The heat exchanger modelled in this study is based upon a heat-exchanger tested by Zietsman and Kröger (2010, Unpublished). The heat exchanger is shown in Fig. A.1, and the dimensions of the heat exchanger are given in Table A.2.

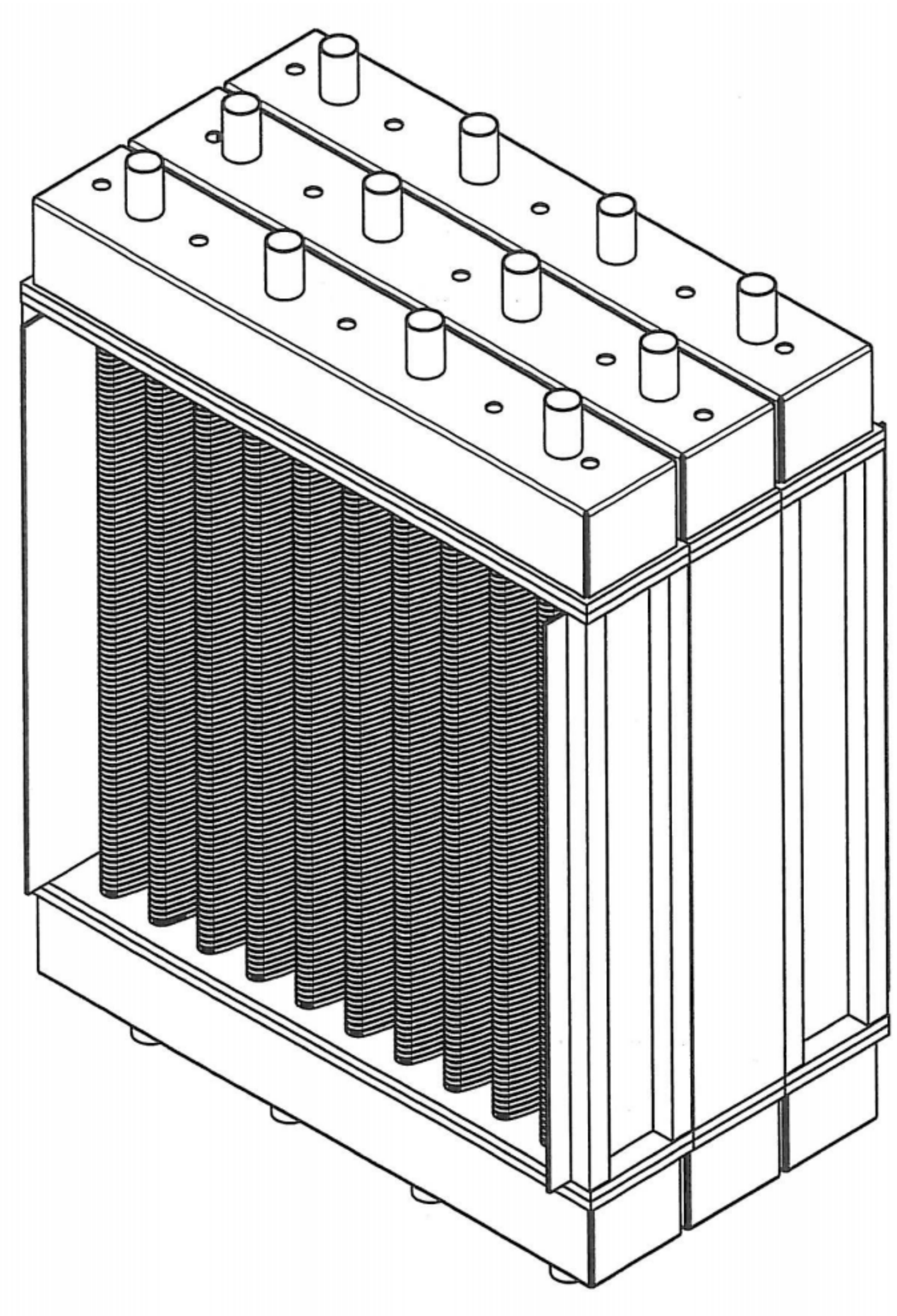

Figure A.1: Heat-Exchanger

The heat transfer correlation for the heat-exchanger modelled is given in Eqn. (A.1).

$$Ny = a \times Ry^b \tag{A.1}$$

The pressure drop correlations across the heat-exchanger, both non-isothermal

Table A.2: Heat Exchanger Specifications

Dimension	**Symbol**	**Value**	
Width	W_b	0.470	m
Height	H_b	0.470	m
Thickness	t_b	0.270	m
Frontal Area	A_{fr}	0.2209	m^2
Rows	n_r	3	#
Tubes per Row	n_{tpr}	10	#
Tube Cross-Section Area	A_{tc}		m^2
Fin Thickness	t_f		m
Fin Pitch (row 1)	P_{f1}		m
Fin Pitch (row 2)	P_{f2}		m
Fin Pitch (row 3)	P_{f3}		m
Tube Inner Area per Unit Length	A_{ti}		m^2/m
Tube Length	L_t	0.47	m
Hydraulic Diameter	d_e	0.023477	m

and isothermal, are given in Equations (A.2) and (A.3).

$$K_{he-nonisothermal} = c_1 \times Ry^{d_1} \tag{A.2}$$

$$K_{he-isothermal} = c_2 \times Ry^{d_2} \tag{A.3}$$

Certain values withheld for confidentiallity reasons.

A.3 Forced Draft Fan-Unit Specifications

The Forced Draft ACC's A-frame fan-unit schematic is shown in Fig. A.2, and its dimensions are listed in Table A.3.

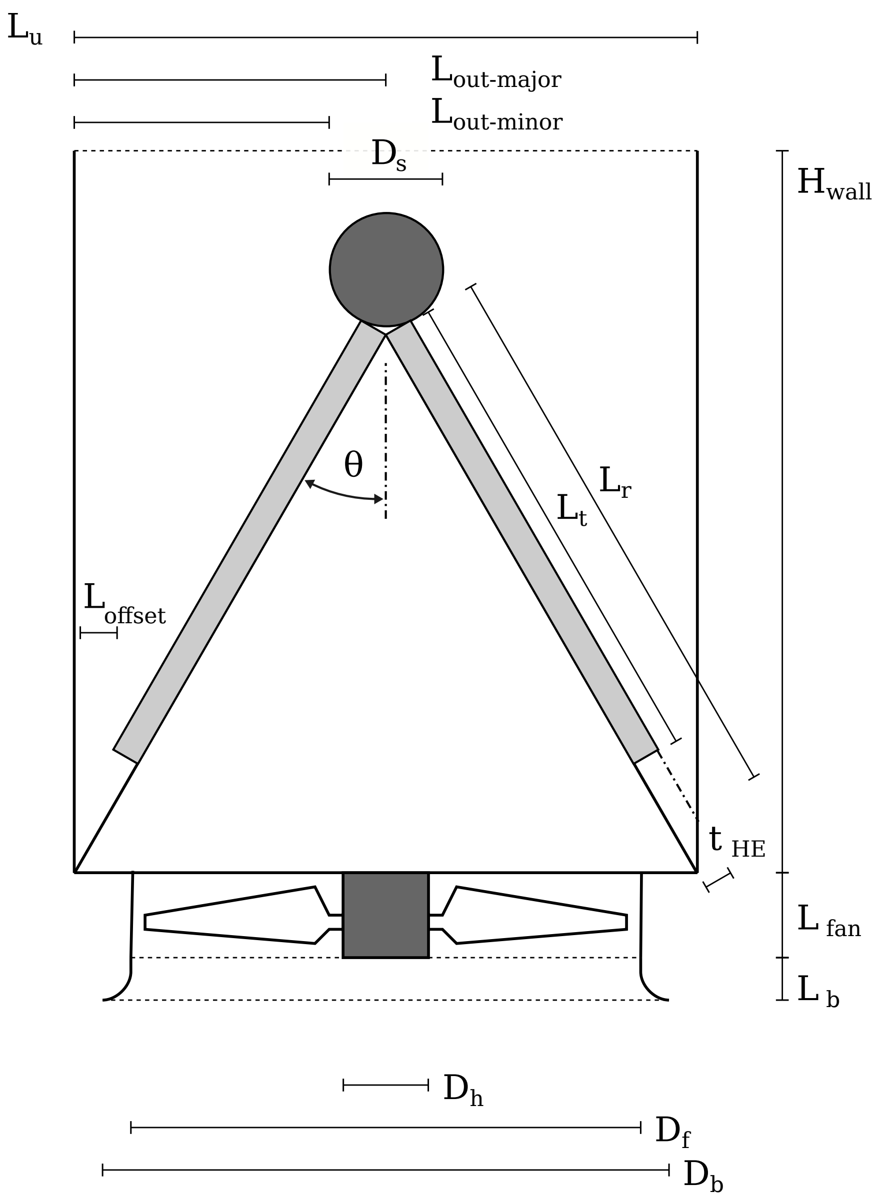

Figure A.2: Forced Draft ACC A-Frame Fan-Unit Schematic

Table A.3: Forced Draft ACC Unit Dimensions

Dimension	**Symbol**	**Value**	
Half Apex Angle	θ	30	°
Fan-Unit Length/Width	L_u	12.5	m
Fan Diameter	D_f	10.420	m
Fan Height	L_f	1.500	m
Hub Diameter	D_h	1.407	m
Bellmouth Diameter	D_b	10.800	m
Bellmouth Height	L_b	0.300	m
HE Tube Length	L_{he}		m
HE Tube Length Ext.	L_{he-ext}		m
HE Thickness	t_{he}		m
HE Horisontal Offset	L_{off}		m
HE Outlet incl. Duct	$L_{out-minor}$		m
HE Outlet excl. Duct	$L_{out-major}$		m
Steam Duct Diameter	D_s	2.400	m
Windwall Height	L_{wall}	14.5	m

Certain values withheld for confidentiallity reasons.

A.4 Induced Draft Fan-Unit Specifications

The Induced Draft ACC's V-frame fan-unit schematic is shown in Fig. A.3, and its dimensions are listed in Table A.4.

Table A.4: Induced Draft ACC Unit Dimensions

Dimension	**Symbol**	**Value**	
Fan Unit Length/Width	L_u	12.5	m
Fan Diameter	D_f	10.420	m
Fan Height	L_f	1.500	m
Hub Diameter	D_h	1.407	m
Bellmouth Radius	R_b	0.200	m
HE Tube Length	L_{he}		m
HE Thickness	t_{he}		m
HE Horisontal Offset	L_w		m
Steam Duct Diameter	D_d		m

Certain values withheld for confidentiallity reasons.

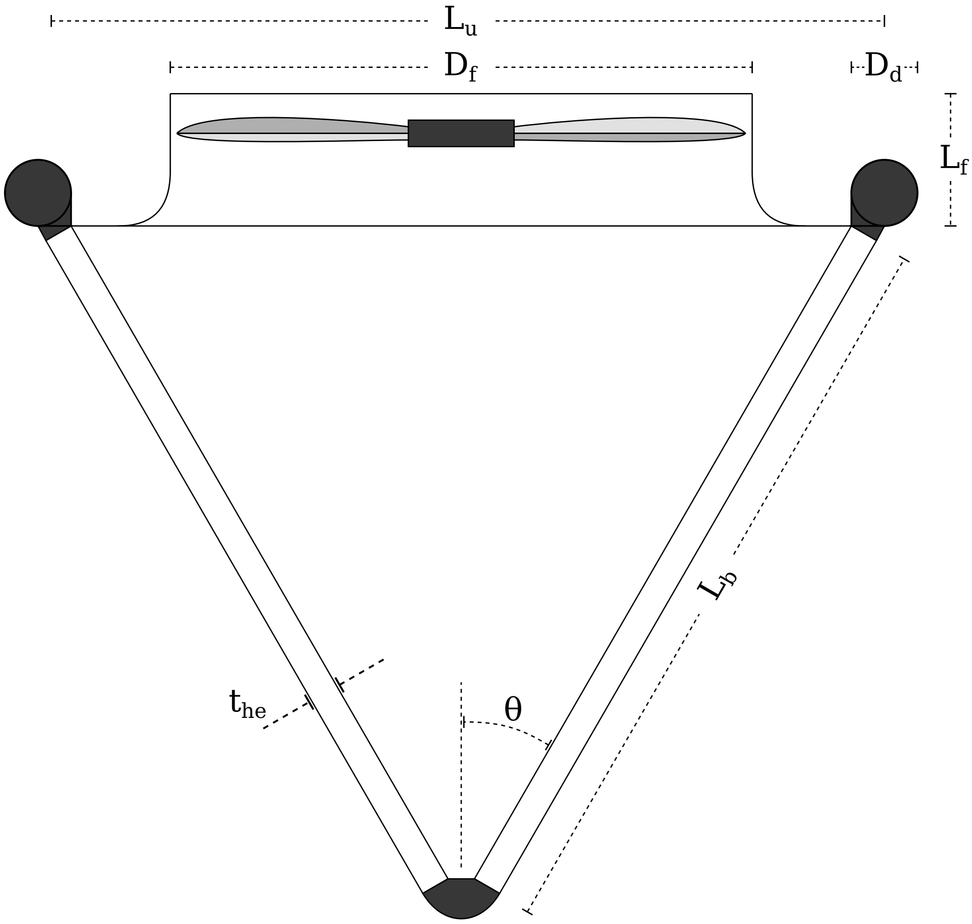

Figure A.3: Induced Draft V-Frame Fan-Unit Schematic

Appendix B

Draft Equations

Draft equations as defined by Kröger (1998) are used to provide one-dimensional models for the preliminary analysis of the fan-units for both the Forced Draft and Induced Draft ACCs.

The draft equation sets the total pressure change over the system equal to the sum of the losses throughout the system, the pressure rise over the fan and the pressure change with height.

$$\Delta p_{total} = \sum_{i}^{n} K_i \frac{(\dot{m}_{ai}/A_i)^2}{2\rho_{ai}} - \Delta p_{fan} + \Delta p_{height} \tag{B.1}$$

B.1 Draft Equation Fan Model

The fan static pressure rise is modelled as a polynomial function dependent on the volumetric flow rate through the fan.

$$\Delta p_{FS}(\dot{V}) = \sum_{i}^{n} a_i \dot{V}^i \tag{B.2}$$

For the purpose of solving the draft equation the experimental data collected by Augustyn (2013) is fit to a polynomial function, with the fan characteristic curves scaled up to full scale from the experimental scale using the fan affinity laws:

$$\left(\frac{\dot{V}_1}{\dot{V}_2}\right) = \left(\frac{\omega_1}{\omega_2}\right)^1 \times \left(\frac{D_1}{D_2}\right)^3 \tag{B.3}$$

$$\left(\frac{p_1}{p_2}\right) = \left(\frac{\omega_1}{\omega_2}\right)^2 \times \left(\frac{D_1}{D_2}\right)^2 \times \left(\frac{\rho_1}{\rho_2}\right) \tag{B.4}$$

$$\left(\frac{\dot{W}_1}{\dot{W}_2}\right) = \left(\frac{\omega_1}{\omega_2}\right)^3 \times \left(\frac{D_1}{D_2}\right)^5 \times \left(\frac{\rho_1}{\rho_2}\right) \tag{B.5}$$

The pressure change due to the change in height is calculated using the dry adiabatic lapse rate.

$$\Delta p_{height} = p_0 \left(1 + \frac{dT}{dz} \times \frac{z}{T_0}\right) \tag{B.6}$$

$$\frac{dT}{dz} = -0.00975 \text{ °C/m} \tag{B.7}$$

B.2 Draft Equation Losses

The system losses accounted for in the draft equation are the jetting losses, K_{dj}, the outlet losses, K_o, the heat-exchanger losses, K_{he}, the contraction losses at the heat-exchanger, K_{ci} and finally the losses attributed to flow obstructions before the fan, K_{screen} and after the fan, K_{fan}.

The heat exchanger entrance contraction loss coefficient, K_{ci}, incurred by the flow entering the fan-unit's heat-exchanger and is defined for normal flow conditions by:

$$K_{ci} = \frac{1}{\sigma_{21}^2} \times \left(1 - \frac{1}{\sigma_c}\right)^2$$

where:

$$\sigma_{21} = \frac{P_{f1}}{t_f + P_{f1}}$$

$$\sigma_c = 0.6144517 + 0.04566493\ \sigma_{21} - 0.336651\ \sigma_{21}^2 + 0.4082734\ \sigma_{21}^3 + 2.672041\ \sigma_{21}^4 \tag{B.8}$$

For the Forced Draft ACC the jetting and outlet losses, respectively K_{dj} and K_o, account for the losses incurred by the flow exiting the A-frame fan-unit's heat-exchangers at an angle and being forced upwards (by the windwalls and/or flow exiting from other heat-exchangers) is defined as:

$$\begin{aligned} K_{dj} = \Bigg[& \left(-2.89188 \left(\frac{L_{offset}}{L_{he}}\right) + 2.93291 \left(\frac{L_{offset}}{L_{he}}\right)^2 \right) \left(\frac{L_{he} L_{out-minor}}{L_{out-major}^2}\right) \left(\frac{28}{\theta}\right)^{0.4} \\ & + \left(\exp\left(2.36987 + 5.8601 \times 10^{-2}\theta - 3.3797 \times 10^{-3}\theta^2\right) \left(\frac{L_{out-minor}}{L_{out-major}}\right)\right)^{0.5} \left(\frac{L_{he}}{L_{he-ext}}\right) \Bigg]^2 \end{aligned} \tag{B.9}$$

$$\begin{aligned} K_o = \Bigg[& \left(-2.89188 \left(\frac{L_{offset}}{L_{he}}\right) + 2.93291 \left(\frac{L_{offset}}{L_{he}}\right)^2 \right) \left(\frac{L_{out-minor}}{L_{out-major}}\right)^3 \\ & + 1.9874 - 3.02783 \left(\frac{D_s}{2L_{out-major}}\right) + 2.0187 \left(\frac{D_s}{2L_{out-major}}\right)^2 \Bigg] \left(\frac{L_{he}}{L_{out-minor}}\right)^2 \end{aligned} \tag{B.10}$$

where the half apex angle θ is in degrees and the remaining length, L, and diameter, D, dimensions are defined in Table A.3.

For the Forced Draft ACC the jetting, outlet, heat-exchanger and contraction losses are combined to form a combined loss coefficient $K_{\theta t}$:

$$\begin{aligned}K_{\theta t} &= K_{he} + \frac{2}{\sigma_{min}^2}\left(\frac{\rho_{ai}-\rho_{ao}}{\rho_{ai}+\rho_{ao}}\right) \\ &+ \frac{2\rho_{ao}}{\rho_{ai}+\rho_{ao}}\left(\frac{1}{\theta_m}-1\right)\left(\left(\frac{1}{\sin\theta_m}-1\right)+2K_{ci}^{0.5}\right) \\ &+ (K_{dj}+K_o)\left(\frac{2\rho_{ai}}{\rho_{ai}+\rho_{ao}}\right)\end{aligned}$$

where:

$$\theta_m = -3.1558 + 0.9133\theta + 0.0019\ \theta^2$$

$$\sigma_{min} = \text{ratio of minimum to free stream flow area through heat-exchanger bundle} \tag{B.11}$$

For the Induced Draft ACC the following downstream loss coefficient, K_d, is used for the flow exiting an inclined heat exchangers:

$$K_d = \exp(+5.488405 - 0.21312209\theta + 3.533265\times10^{-3}\theta^2 - 0.2901016\times10^{-4}\theta^3) \tag{B.12}$$

where θ is in degrees.

For the Induced Draft ACC the heat exchanger inlet contraction losses is adjusted for off-axis inflow givening an adjusted loss coefficient $K_{i\theta}$:

$$K_{i\theta} = \left(K_{ci}^0.5 + \frac{1}{sin(\theta)} - 1\right)^2 \tag{B.13}$$

B.3 Forced Draft ACC Curves

The fan and system resistance curves obtained by solving the analytical draft equations for both the L-fan and N-fan configured Forced Draft ACCs are shown in Figs. B.1 and B.2.

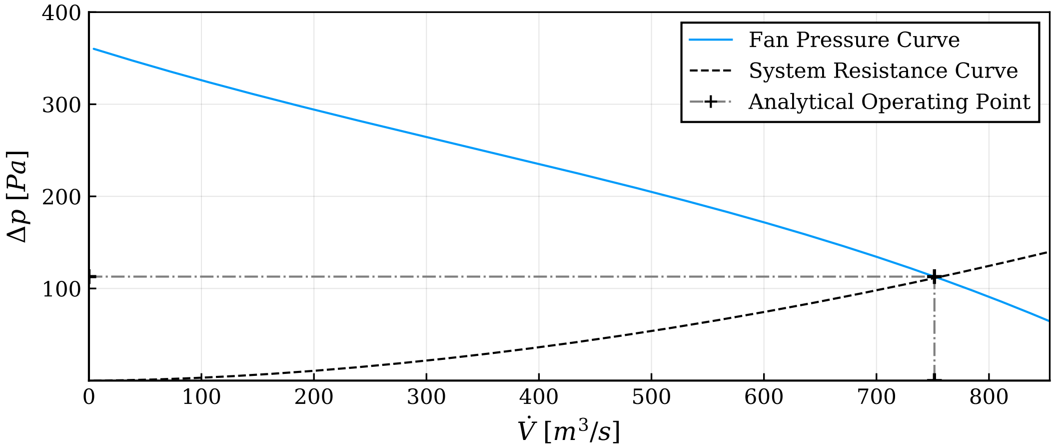

Figure B.1: Forced Draft L-Fan System Resistances ($\gamma_{tip} = 9°$)

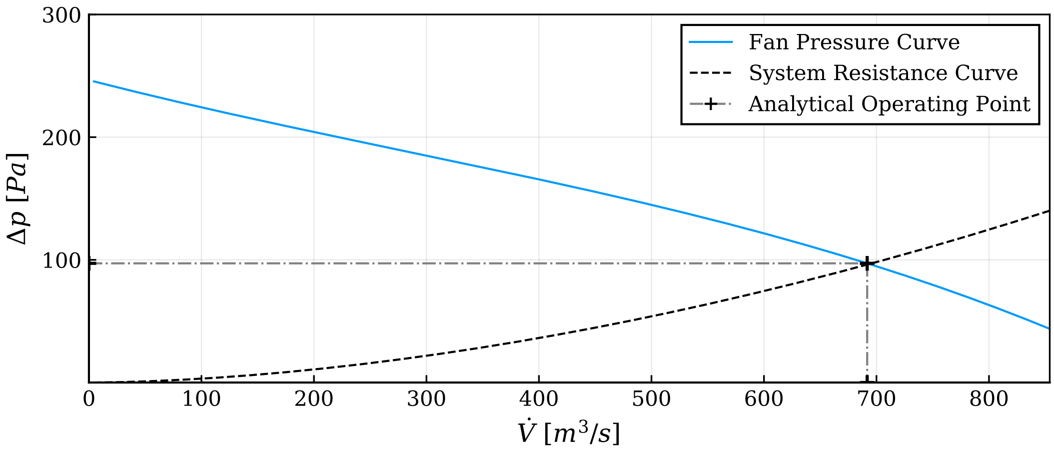

Figure B.2: Forced Draft N-Fan System Resistances ($\gamma_{tip} = 10°$)

B.4 Induced Draft ACC Curves

The fan and system resistance curves obtained by solving the analytical draft equations for both the L-fan and the N-fan configured Induced Draft ACCs are shown in Figs. B.3 and B.4.

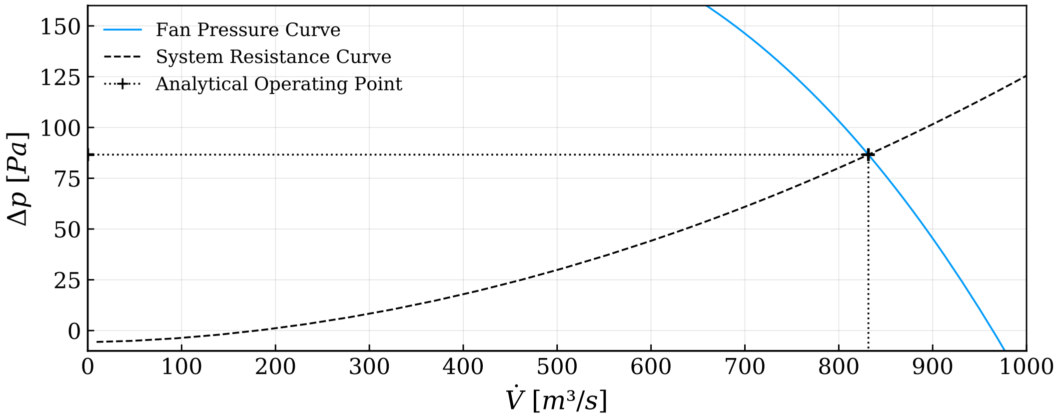

Figure B.3: Induced Draft L-Fan System Resistances ($\gamma_{tip} = 9.3°$)

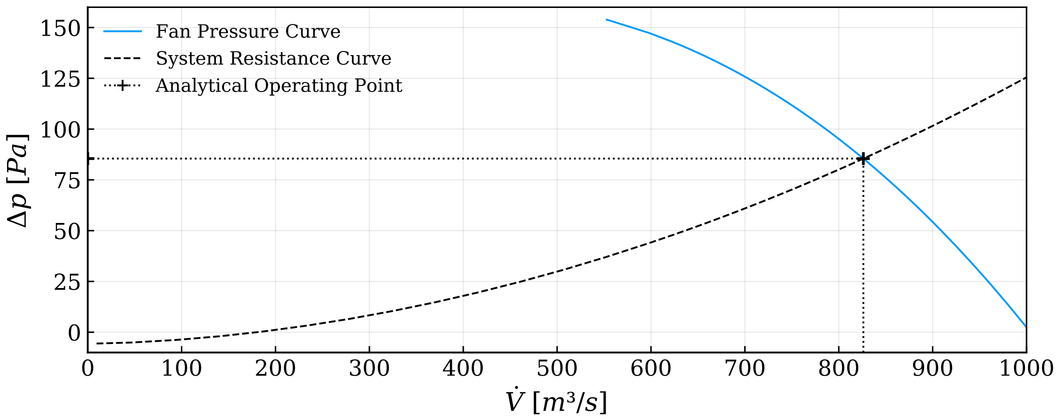

Figure B.4: Induced Draft N-Fan System Resistances ($\gamma_{tip} = 11.6°$)

List of References

Augustyn, O.P. (2013 Dec). *Experimental and Numerical Analysis of Axial Flow Fans*. Master's thesis, University of Stellenbosch.

Bredell, J.R. (2005 Dec). *Numerical Investigation of Fan Performance in a Forced Draft Air-Cooled Steam Condenser*. Master's thesis, University of Stellenbosch.

Bruneau, P. (1994). *The Design of a Single Rotor Axial Flow Fan for a Cooling Tower Application*. Master's thesis, University of Stellenbosch.

Chen, L., Yang, L., Du, X. and Yang, Y. (2018). Novel air-cooled condenser with v-frame cells and induced axial flow fans. *International Journal of Heat and Mass Transfer*, vol. 177, pp. 167–182.

Drela, M. (1989). Xfoil: An analysis and design system for low reynolds number airfoils. *Low Reynolds Number Aerodynamics*.

du Toit, C. and Kröger, D.G. (1993). Modelling of the recirculation in mechanical-draught heat exchangers. *R & D Journal*, vol. 9, no. 1, pp. 2–8.

Duvenage, K., Vermeulen, A., Meyer, C.J. and Kröger, D.G. (1996). Flow distortions at the fan inlet of forced draught air-cooled heat exchangers. *Applied Thermal Engineering*, vol. 16, no. 8/9, pp. 741–752.

Engelbrecht, R.A. (2018 Mar). *Numerical Investigation of Fan Performance in a Forced Draft Air-Cooled Condensor*. Ph.D. thesis, University of Stellenbosch.

Goldschagg, H.B. (1993 Mar). Lessons learnt from the worlds largest forced draft direct air cooled condenser. In: *Proc. EPRI Int. Symp. On Improved Technology for Fossil Power Plants*. Washington.

Hargreaves, D.M. and Wright, N.G. (2007). On the use of the k-epsilon model in commercial cfd software to model the neutral atmospheric boundary layer. *Journal of Wind Engineering and Industrial Aerodynamics*, vol. 95, pp. 355–369.

Hoerner, S.F. (1965). *Fluid-Dynamic Drag*. Self-published.

Huang, X., Chen, L., Xiaoze, D. and Yongping, Y. (2019). Cooling performance enhancement of air-cooled condendsers by guiding air flow.

Joubert, R. (2010 Mar). *Influence of geometric and environmental parameters on air-cooled steam condensor performance.* Master's thesis, University of Stellenbosch.

Kröger, D.G. (1998). *Air-cooled Heat Exchangers and Cooling Towers.* Departement of Mechanical Engineering University Stellenbosch, Stellenbosch, South Africa.

Launder, B.E. and Spalding, D.B. (1974). The numerical computation of turbulent flows. *Computer Methods in Applied Mechanics and Engineering.*

Louw, F.G. (2011 Mar). *Performance Trends of a Large Air-Cooled Steam Condensor during Windy Conditions.* Master's thesis, University of Stellenbosch.

Louw, F.G. (2015 Dec). *Investigation of the flow field in the vicinity of an axial flow fan during low flow rates.* Ph.D. thesis, University of Stellenbosch.

Monroe, R.C. (1979). Improving cooling tower fan system efficiencies. *Combustion*, vol. 50, no. 11, pp. 20–21.

Owen, M.T.F. (2010 Mar). *A numerical investigaation of air-cooled steam condenser performance under windy conditions.* Master's thesis, University of Stellenbosch.

Salta, C.A. and Kröger, D.G. (1995). Effect of inlet flow distrotion on fan performance in forced draught air-cooled heat exchangers. *Applied Thermal Engineering*, vol. 15, no. 6, pp. 551–561.

Schobeiri, M.T. (2010). *Fluid Mechanics for Engineers.* Springer, Berlin, Heidelberg.

Thiart, G.D. and von Backström, T.W. (1993). Numerical simulation of the flow field near an axial flow fan operating under distorted inlet conditions. *Journal of Wind Engineering and Industrial Aerodynamics*, vol. 45, no. 2, pp. 189–214.

van der Spuy, S.J. (2011 Dec). *Perimeter Fan Performance in Forced Draught Air-cooled Condensers.* Ph.D. thesis, University of Stellenbosch.

van der Spuy, S.J., von Backström, T.W. and Kröger, D.G. (2009). An evaluation of simplified methods to model the performance of axial flow fan arrays. *R & D Journal of the South African Institute of Mechanical Engineers*, vol. 26, pp. 12–20. Revised 2010 copy of the article.

van Rooyen, J. (2007 Mar). *Performance Trends of an Air-Cooled Steam Condenser Under Windy Conditions.* Master's thesis, University of Stellenbosch.

Versteeg, H.K. and Malalasekera, W. (2015). *Introduction to Computational Fluid Dynamics: The Finite Volume Method.* 5th edn. McGraw-Hill Education, New York, NY.

Wallis, R.A. (1983). *Axial flow fans and ducts.* John Wiley.

Wilkinson, M.B. (2017). *The Design of an Axial Flow Fan for Air-Cooled Heat Exchanger Applications.* Master's thesis, University of Stellenbosch.

Yang, L., Yang, Y. and Du, X. (2011 July). Performance assessment of air-cooled steam condenser with guide vane cascade. *Chinese Science Bulletin*, vol. 56, no. 21, pp. 2272–2280.

Zietsman, C. and Kröger, D.G. (2010). Performance characteristics of – thermal finned tubes. Unpublished.

Çengel, Y.A. and Boles, M.A. (2008). *Thermodynamics: An Engineering Approach*. 7th edn. McGraw-Hill, New York, NY.